

# Charge transport and interface phenomena in semiconducting polymers

**Citation for published version (APA):**

Gommans, H. H. P. (2005). *Charge transport and interface phenomena in semiconducting polymers*. [Phd Thesis 1 (Research TU/e / Graduation TU/e), Applied Physics and Science Education]. Technische Universiteit Eindhoven. <https://doi.org/10.6100/IR595007>

**DOI:**

[10.6100/IR595007](https://doi.org/10.6100/IR595007)

**Document status and date:**

Published: 01/01/2005

**Document Version:**

Publisher's PDF, also known as Version of Record (includes final page, issue and volume numbers)

**Please check the document version of this publication:**

- A submitted manuscript is the version of the article upon submission and before peer-review. There can be important differences between the submitted version and the official published version of record. People interested in the research are advised to contact the author for the final version of the publication, or visit the DOI to the publisher's website.
- The final author version and the galley proof are versions of the publication after peer review.
- The final published version features the final layout of the paper including the volume, issue and page numbers.

[Link to publication](#)

**General rights**

Copyright and moral rights for the publications made accessible in the public portal are retained by the authors and/or other copyright owners and it is a condition of accessing publications that users recognise and abide by the legal requirements associated with these rights.

- Users may download and print one copy of any publication from the public portal for the purpose of private study or research.
- You may not further distribute the material or use it for any profit-making activity or commercial gain
- You may freely distribute the URL identifying the publication in the public portal.

If the publication is distributed under the terms of Article 25fa of the Dutch Copyright Act, indicated by the "Taverne" license above, please follow below link for the End User Agreement:

[www.tue.nl/taverne](http://www.tue.nl/taverne)

**Take down policy**

If you believe that this document breaches copyright please contact us at:

[openaccess@tue.nl](mailto:openaccess@tue.nl)

providing details and we will investigate your claim.

# **Charge Transport and Interface Phenomena in Semiconducting Polymers**

PROEFSCHRIFT

ter verkrijging van de graad van doctor aan de Technische  
Universiteit Eindhoven, op gezag van de Rector Magnificus,  
prof.dr.ir. C.J. van Duijn, voor een commissie aangewezen door  
het College voor Promoties in het openbaar te verdedigen op  
woensdag 21 september 2005 om 16.00 uur

door

Hendrikus Hubertus Petrus Gommans

geboren te Eindhoven

Dit proefschrift is goedgekeurd door de promotoren:

prof.dr.ir. R.A.J. Janssen

en

prof.dr. H.H. Brongersma

Copromotor:

dr.ir. M. Kemerink

This research has been financially supported by Stichting voor Fundamenteel Onderzoek der Materie (FOM) (program E-11).

Omslag: Paul Verspaget

Printed at the Universiteitsdrukkerij, Eindhoven University of Technology

CIP-DATA LIBRARY TECHNISCHE UNIVERSITEIT EINDHOVEN

Gommans, Hendrikus Hubertus Petrus

Charge Transport and Interface Phenomena in Semiconducting Polymers / door Hendrikus Hubertus Petrus Gommans. – Eindhoven : Technische Universiteit Eindhoven, 2005.

Proefschrift.

ISBN 90-386-2271-6

NUR 926

Trefwoorden: licht emitterende diodes / fotovoltaïsche cellen / geleidende polymeren / grensvlakken / ionen bundel technieken / elektrische geleiding

Subject headings: light emitting diodes / photovoltaic cells / conducting polymers / interface formation / ion beam analysis / electrical conductivity / Boltzmann-equation

*“If you are not criticized, you may not be doing much.”*

Donald H. Rumsfeld



# Contents

<b>1 Introduction</b>	<b>1</b>
1.1 General	2
1.2 Charge transport in organic materials	2
1.3 Applications	4
1.3.1 Polymer light-emitting diode (pLED)	4
1.3.2 Solar cell	5
1.4 Charge transport: electrical characterization	6
1.4.1 Experimental	6
1.4.2 Modeling	8
1.5 Elemental composition: ion beam analysis	9
1.6 Scope of this thesis	10
1.7 References and notes	12
<b>2 Interface formation in K doped MDMO-PPV LEDs</b>	<b>15</b>
2.1 Introduction	16
2.2 Experimental	17
2.2.1 Sample preparation and electroluminescence	17
2.2.1. Ion scattering spectrometry	17
2.3 Results	18
2.3.1 Electroluminescence	18
2.3.2 Ion scattering spectrometry	19
2.4 Discussion	21
2.4.1 Diffusion profile	21
2.4.2 Electroluminescence	22
2.5 Conclusion	23
2.6 Reference and notes	25
<b>3 Interface formation in Cs doped MDMO-PPV LEDs</b>	<b>29</b>
3.1 Introduction	30
3.2 Experimental	30
3.3 Results	31
3.3.1 Al / MDMO-PPV / ITO	31
3.3.2 Al/ Cs/ MDMO-PPV/ ITO	36
3.4 Discussion	39
3.5 Conclusion	41
3.6 References and notes	42

<b>4 Field and temperature dependence of the photocurrent in polymer:fullerene bulk heterojunction solar cells</b>	<b>45</b>
4.1 Introduction	46
4.2 Results and discussion	46
4.3 Conclusions	50
4.3 References and notes	51
<b>5 Negative capacitances in low-mobility solids</b>	<b>53</b>
5.1 Introduction	54
5.2 Theory	55
5.3 Experimental	58
5.4 Summary	60
5.5 References and notes	61
<b>6 Universality of ac conduction for generalized space charge limited transport in ordered solids</b>	<b>63</b>
6.1 Introduction	64
6.2 Drift-diffusion	64
6.3 Results and discussion	66
6.3.1 Approximate power law behavior	66
6.3.2 Taylor Isard scaling and the BNN relation	69
6.4 Conclusion	71
6.5 References and notes	72
<b>Summary</b>	<b>75</b>
<b>Samenvatting</b>	<b>77</b>
<b>Dankwoord</b>	<b>79</b>
<b>List of publications</b>	<b>80</b>
<b>Curriculum Vitae</b>	<b>81</b>

## Introduction

### Abstract

*This chapter introduces the basic concepts of conjugated polymers and their application in light-emitting diodes and solar cells. The polymer-electrode interfaces in these devices form the main subject of this thesis. To investigate these interfaces and understand their role on device performance, ion-beam analysis, I-V characterization and admittance spectroscopy are used in combination with model calculations that numerically solve the drift-diffusion equations for charge transport. The background of these experimental and computational techniques is briefly explained. The final section provides an overview of the contents of the thesis.*



## 1.1 General

With the discovery of conducting polymers<sup>1</sup> a new class of materials has emerged that attracts worldwide attention in academia and industry. The unique combination of solubility with semiconducting or metallic electronic structure has demonstrated to be advantageous for a number of technological applications such as light-emitting diodes (LED) and photovoltaic cells. All these molecular devices have to be wired and the actual choice of electrode material is recognized to be of crucial importance for the device performance. In general, such electrode-polymer interfaces are depicted as abrupt junctions and charge transport barriers are estimated by the bulk properties of the separate materials. However, interfaces generally differ from this oversimplified picture due to modifications in e.g. composition and electronic structure. In this thesis the exotic structure of these interfaces is demonstrated by combining experimental results and model calculations for device structures typically applied in LEDs and solar cells.

Contacts on conducting polymers are typically manufactured in two different manners: [1] a contact is created by spin-coating a solution onto a metal(lic) (conductor) or [2] a metal is brought onto the polymer layer by vapor deposition. Even when the same element from the periodic system is chosen as electrode these methods generally lead to different contacts.

During deposition, metal atoms condense onto the polymer layer out of the gas phase. Depending on the surface and the interface energy, two materials either tend to phase separate/cluster or mix, disregarding the option of the formation of a compound material for the moment. Together with the deposition rate, this property determines the extent of diffusion. The composition of these diffusion profiles may be studied by ion beam techniques and given the depth and resolution requirements one may choose from a broad spectrum (LEIS, SIMS, NICISS-TOF, RBS, ERDA).<sup>2</sup>

In case a diffusive interface layer is formed, gap states may be created up to considerable depths due to chemical interaction (bond breaking/formation, charge transfer). Depending on the concentration, these gap states (either donor or acceptor states) result in band bending, as Fermi levels tend to align. Considering the dimensions of polymer layers in photonic applications ( $\sim 10^{-5}$  cm) the importance of such effects is not necessarily restricted to charge injection solely. In order to study these phenomena, steady state as well as frequency resolved electrical characterization is performed in a temperature range of 80-300 K. The results are interpreted by numerical modeling in the drift-diffusion approximation and allow for the identification of the carrier mobilities, the recombination mechanism and the field distribution in the polymer layer. Although in LED structures the diffusion current may be neglected, in a solar cell structure diffusion is indispensable in order to come to grips with its performance.

## 1.2 Charge transport in organic materials

Starting with the ground state of a C atom we have  $1s^2 2s^2 2p^2$ , which gives us four electrons in the outer electronic orbitals. In the presence of other atoms (C, H, O, etc.) these levels may hybridize either into  $sp$ ,  $sp^2$  or  $sp^3$  orbitals, each possessing their unique spatial character. All these orbitals are strongly localized, however in case of  $sp^2$  we are left with one unhybridized  $p_z$  orbital. This  $p_z$  orbital is oriented perpendicular to the three  $sp^2$  orbitals, that are coplanar with angles of  $120^\circ$  between each other (figure 1). In case of an identically hybridized neighbor C atom with similar orientation, these  $p_z$  orbitals will overlap and form a molecular  $\pi$  bond. Together with the  $\sigma$  bond between the two C atoms (created by two hybridized  $sp^2$  orbitals) this results in a double bond. Given a row of neighboring  $sp^2$  hybridized C atoms, all with their  $p_z$  orbitals parallel, this then results in an alternating single bond, double bond structure (figure 2). Maintaining this alternating sequence (conjugation structure), these bonds are located arbitrarily, i.e. the positions of

the double and single bonds may be exchanged with small or no energy difference. The  $\pi$ -electrons in a conjugated structure are thus delocalized over the entire molecule. A simple example is the benzene molecule with two delocalized electron clouds on both sides of the carbon ring structure. Another example is polyacetylene as shown in figure 2.

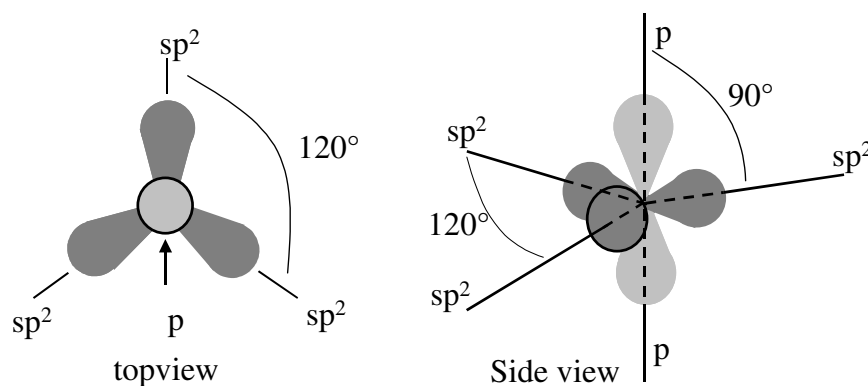


**Figure 1:** Spatial representation of the  $sp^2$  hybridized carbon atom from top and side view; note that the  $p$  orbital has two elongated tails.

The dominance of the  $\pi$ -electrons in the transport properties originates from the fact that they form the highest occupied molecular orbital (HOMO) and lowest unoccupied molecular orbital (LUMO), which are the electronic levels that determine the semiconducting properties of these materials in optical excitations and charge transport.

In order to obtain charge transport on macroscopic length scales there are two alternative routes one can pursue: growing a lattice of (smaller) molecules or casting films of molecules with high-molecular-weight from solution. Regardless ones choice, charge transport is strongly determined by the interaction *between* molecules. The first method offers an opportunity to study these interactions due to the high level of *symmetry* in location and orientation of the molecules. In the latter technique the transport is dictated by a variety of phenomena that is generally accounted for in the *disorder*. This term includes the dispersion in molecular structure, conjugation length, defects, impurities, morphology etc. Consequently, on a microscopic level each film is different. However, by variation of synthesis route, molecular structure, solvent and spin casting conditions a handle is given in controlling this disorder and consequently, the *macroscopic* transport properties in these films. Driven by a technological interest attention has been focused on the option of casting out of solution.

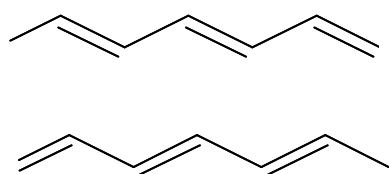


**Figure 2:** The chemical structures of polyacetylene in the twofold degenerate ground state.

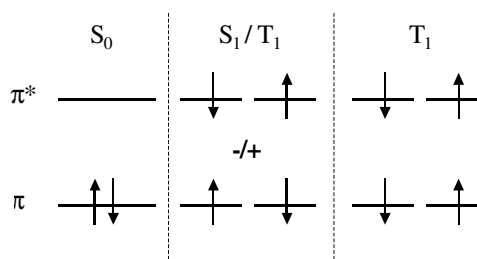


**Figure 3:** Possible spin orientations in the ground state ( $S_0$ ) and first excited state ( $S_1$  or  $T_1$ ).

The electronic properties of the conjugated material thus depend on microscopic variables that may also be expressed in energy parameters: electron-lattice interaction, electron-electron (electron-hole) interaction, bandwidth and the random disorder potential. The relative strength of

the electron-hole interaction (exciton binding energy) in fact determines whether to view this material as a molecular solid or as a one-dimensional semiconductor. After 25 years there still is a fierce debate on this parameter [see refs 3-5]. The random disorder potential leads to (un)correlated hopping transport (as opposed to band transport) and gives rise to a field dependent mobility, the so-called Poole-Frenkel behavior.<sup>6,7</sup> There is discussion about its energetic<sup>6,7</sup> or structural origin<sup>8</sup>. Recently however, this field dependence has been recognized as a charge density dependence.<sup>9,10</sup>

The interest in conducting polymers has been boosted after demonstrating electroluminescence in the visible spectrum for poly(phenylene vinylene).<sup>11</sup> Luminescence is related to the radiative decay of excited electronic states. The lowest excited state consists of a relaxed electron and hole in the LUMO and HOMO, respectively. Depending on spin orientation of these charges the optical transition is either allowed (spin orientation = anti parallel, singlet state,  $S_1$ ) or forbidden (spin orientation = parallel, triplet state,  $T_1$ ) and the luminescence is termed fluorescence or phosphorescence, respectively (figure 3). The exchange energy in conjugated polymers can be as large as 0.5-1.0 eV and places the  $T_1$  state at considerably lower energy than the  $S_1$  state. In principle, the energy corresponding to the  $\pi$ - $\pi^*$  transition can be chosen to match any color, as it is primarily determined by the molecular structure. However, matrix effects in the film may alter these.

In order to obtain conductivity in this class of materials, charges actually need to be inserted. Several means are available: chemical doping (charge transfer, electrochemical, acid-base), photodoping or charge injection at a metal-semiconductor interface.<sup>12</sup> The first method is extremely efficient as the highest degree of doping may even result in altering the electronic structure into that of a metal. Photo excitation creates excitons (= bound electron-hole pair) in the singlet state that may result in the formation of free electrons and holes in the LUMO and HOMO, respectively. The break up of the exciton into free charges, however, has a low probability in general, as it competes with (non)radiative decay processes that are generally dominant. Injection through a metal-semiconducting interface does not rely on the presence of counter charges. As a consequence, in case of efficient charge injection (ohmic contact), space charge will be created, which severely limits the maximum number of charge carriers in these films. Realizing this limiting condition, however, allows us to determine the mobility for a single charge carrier without significantly altering the film properties. In diode geometry nullifying this limit by bipolar injection remains unattainable, as generally the mobilities for charge carriers with opposite sign differ and the recombination probability is larger than zero. While this limit is thus restrictive for a diode, it can be overcome in a field-effect transistor.

## 1.3 Applications

### 1.3.1 Polymer light-emitting diode (pLED)

The pLED consists of a photoactive layer (here, poly[2-methoxy-5-(3',7'-dimethyloctyloxy)-1,4-phenylene vinylene] (MDMO-PPV)) sandwiched between two electrodes. The operation mechanism is schematically depicted in figure 4 and relies on the injection, transport and recombination of electrons and holes to form an exciton that relaxes by the emission of a photon. The electrode materials are chosen as to minimize the barrier for charge *injection*. As exciton formation requires both charge carriers, this generally results in two different electrodes, one suitable for the injection of holes and the other for electrons. It is nearly impossible to quantitatively predict the barrier for charge injection for an arbitrary combination of electrode material and conjugated polymer. As a rule of thumb, one is of course allowed to compare the energy levels of the electrode and conjugated material separately, however, photoemission spectroscopy has demonstrated that vacuum level alignment is not generally valid. Given this

barrier, advanced injection models have been developed to predict its field and temperature dependence.<sup>13, 14</sup>

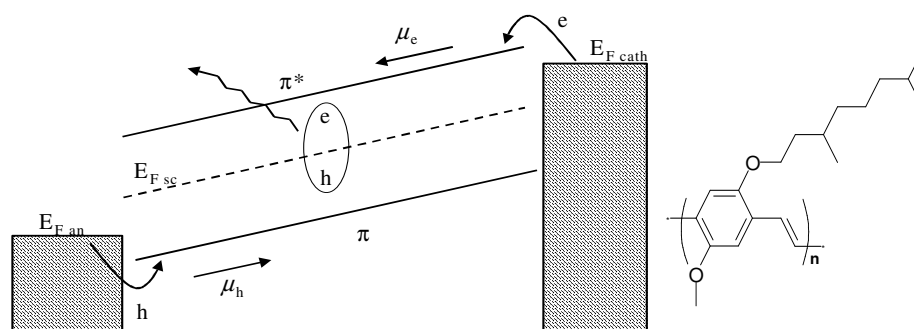


**Figure 4:** Left: Schematic representation of the transport phenomena in a pLED: injection - transport - recombination; the significance of the energy levels as drawn here is limited. Right: Chemical structure of MDMO-PPV.

For an optimal device performance injection barriers have to be minimized and the current density becomes bulk limited (as opposed to injection limited). With a few assumptions concerning (semi-)classical parameters: the injection barriers, the built-in potential (= potential difference between the two contacts in open circuit) and the intrinsic charge depletion, one can determine the *mobility* in so-called space charge configuration. The typical mobilities for electron and hole transport in MDMO-PPV has been determined to be:  $3 \times 10^{-9}$  and  $3 \times 10^{-7}$   $\text{cm}^2/\text{Vs}$  at zero electric field and room temperature<sup>15</sup>. As explained in the previous section charge transport in a film is governed by disorder. Consequently, the term *the* mobility on a polymer film should be used with some reserves as it is strongly affected by preparation conditions. Moreover, the mobility is a macroscopic parameter that by definition is not allowed to depend on sample dimensions. Decreasing film thicknesses below  $10^{-5}$  cm may thus lead to difficulties in its persistent use, considering the minimum size at which the transport properties are defined by the extent of disorder (at least  $10^{-6}$  cm in MDMO-PPV).<sup>8</sup>

The last issue in the LED operation is the *formation of (singlet) excitons* and their subsequent *radiative recombination*. The first process is related to the charge capture cross-section and spin statistics. The second process has to compete with the non-radiative decay as well as intersystem crossing (a spin flip changing the singlet into the triplet state). Other reported exciton quenching mechanisms result from the presence of defects, trap states, single charges, (second) excitons and electrodes.<sup>16</sup>

### 1.3.2 Solar cell

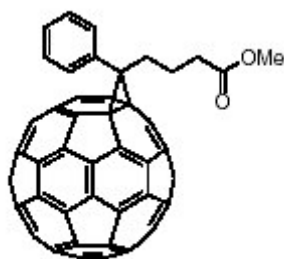


**Figure 5:** Chemical structure of PCBM.

The operation mechanism is schematically depicted in figure 6 and the overall efficiency depends on a variety of parameters that will be briefly explained.

The solar cell in principle consists of a photoactive layer sandwiched between two electrodes. The bandgap of the photoactive layer should be chosen to *match the solar irradiance spectrum*. In order to create charge carriers rather than excitons that are formed in a pure material, polymer solar cells commonly use a combination of two semiconductors with complementary electronic levels. The initial step after photoexcitation is the dissociation of an exciton via charge

transfer at the interface of these two materials. In the devices discussed in this thesis MDMO-PPV is used as an electron donor and 1-(3-methoxycarbonyl)propyl-1-phenyl-[6,6]-methanofullerene (PCBM) (figure 5) is used as an electron acceptor<sup>17-19</sup>. In this combination of materials photon absorption is predominantly by MDMO-PPV because of its much higher absorption coefficient in the visible region. The optimum in donor-acceptor ratio for this charge transfer process is given by the phase separation of the materials as well as the exciton size and diffusion length on a MDMO-PPV unit. Such a cell consisting of a blend of two materials is named bulk heterojunction solar cell.

After the charge transfer the electrons and holes have to escape their Coulomb potential and *migrate* towards either electrode due to the internal field. This migration leads to an electric field opposing the 'original' field that will be reduced up to a certain distance from the electrodes. As both charge carriers will *recombine* at the opposing electrodes a continuous current flow is created. The resulting electric field in the polymer layer depends thus on the free electron and hole concentration, their drift and diffusion mobility, the generation rate, and the recombination rate in the bulk and at the electrodes.

Considering the two phases in this bulk heterojunction solar cell, the mixing ratio, miscibility and morphology determine the formation of percolative paths for efficient charge transport (at present, it is assumed that electrons are transported by the PCBM material, and holes by the MDMO-PPV). It should be clear that the importance of the mixing ratio on the collection efficiency could hardly be overestimated as it determines the photo-absorption, charge transfer and electron and hole transport in these cells simultaneously. A similar argument holds for the layer thickness due to its influence of on the photo-absorption and charge transport.

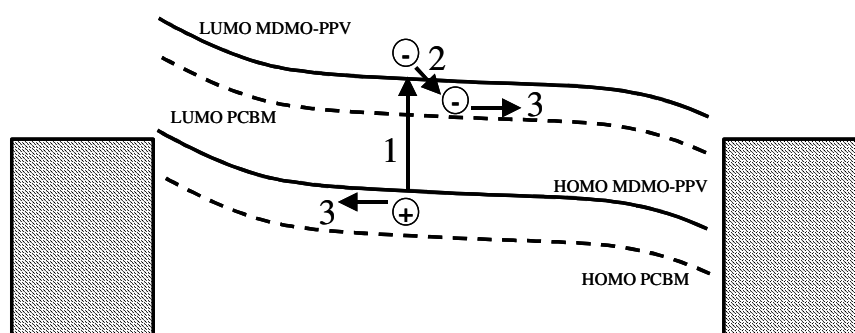


**Figure 6:** Schematic representation of the transport phenomena in a solar cell: 1 absorption; 2 charge transfer; 3 coulomb escape and transport.

## 1.4 Charge transport: electrical characterization

### 1.4.1 Experimental

In order to study the physical processes that underlie the charge transport in polymer opto-electronic devices, steady state and frequency resolved electrical characterization is conducted and its results are explained by the numerical solutions of the drift-diffusion equations.

Steady state *I-V* characterization will in general be applied to determine either the injection barrier at an interface or the mobility in a polymer layer for a single charge carrier and this can be easily done as a function of temperature. The electric field is not necessarily restricted to either the interface or the semi-conducting layer and it is in principle possible to characterize the injection barrier and mobility simultaneously. However, in that case no analytical expression can be easily derived and the uniqueness of a set of parameters that allow for a numerical model description is difficult to demonstrate. In opto-electronic devices we deal with both charge carriers simultaneously

and the current will thus be governed by the drift-diffusion equations in case we ignore thermal aspects in the transport.<sup>20</sup> The drift-diffusion model is referred to as semi-classical as two types of particles are involved as opposed to the classical one particle case. Moreover, the transport is quantum mechanical in nature. The full quantum mechanical treatment, however, leads to another form of the transport equation.<sup>21</sup>

As we apply this model to describe the electrical characterization on opto-electronic devices it is obvious that many assumptions have to be made concerning the field, temperature and concentration dependence of the electron and hole injection and mobility and recombination / generation in the polymer layer. Note that the disorder aspect in transport may be taken into account via the mobility through functionalized dependences on field and concentration. Moreover, as screening in conjugated materials is very poor, the presence of charges in the conducting layer will result in severe band bending. In fact, determining the single carrier mobility in space charge configuration is based on this principle. In order to learn about this band bending the *position* of *all* charges, regardless the reason of their presence has to be known. This is a major disadvantage in electrical characterization as there is no spatial resolution by definition.\*

The experimental challenge is thus to reduce these numerous assumptions by for instance manufacturing (poorly operating!) devices that only allow for single carrier transport with known injection barriers. One has to bear in mind that the manufacturing process itself, however, is very likely to affect the charge transport and care should be taken in extrapolating the obtained information to real device configurations.

Frequency resolved electrical characterization (admittance spectroscopy) gives an amplitude for the response signal as well as a phase difference relative to the stimulus. When expressed in complex vector notation this provides a real and imaginary part of the response as a function of frequency, named the conductance,  $G(\omega)$ , and susceptance,  $B(\omega)$ , respectively:

$$Y(\omega) \equiv \frac{i_{ac}}{v_{ac}} \equiv G(\omega) + iB(\omega) \equiv G(\omega) + i\omega C(\omega).$$

It is common practice to discuss the imaginary part in terms of the capacitance,  $C(\omega)$ , in stead of  $B(\omega)$ . Note that all functions are real valued except for the admittance,  $Y(\omega)$ , itself. Provided the causality requirement is satisfied and the frequency is real valued, the Kramers-Kronig relation holds, which establishes the relation between the real and imaginary part of the response function. Depending on the field of research the measured response signal is termed differently: complex susceptibility,  $\chi(\omega)$ , complex permittivity,  $\epsilon(\omega)$ , or complex conductivity,  $\sigma(\omega)$ . The last one in fact equals  $Y(\omega)$  times a spatial dimension of the sample. These response functions are now related to each other in the following manner:

$$\epsilon(\omega) = \epsilon_0 [1 + \chi(\omega)]; \sigma(\omega) = i\omega\epsilon_0\chi(\omega); \sigma(\omega) = i\omega\epsilon_0 \left[ \frac{\epsilon(\omega)}{\epsilon_0} - 1 \right],$$

where  $\epsilon_0$  is the permittivity in vacuum. This variety in response functions led to some difficulties in interpretation in the past, as identical responses were attributed to completely different physical phenomena.

The surplus of this technique is manifold:

1: In case there is no transport through the polymer layer the imaginary part can be used to determine the *permittivity* of the medium via the charging of the capacitor plates. In principle, this can be done at a single frequency, which is not true for the following cases.

2: The *trapping-detrapping* rates from states in the bandgap can be studied<sup>22</sup>. In the frequency domain one can then identify three regimes in which all, some and no trapping sites are

---

\* In this thesis, the electrical characterization and the diffusion profiles of charged species will be combined in a description of the transport in LED devices.

able to release charges. Often this characterization is performed at a broad temperature range in order to control the population of the gap states. Here, again the spatial position of the trapping sites should be known for a correct interpretation of the spectra. See chapter 3.

3: The *disorder* can be expressed as a superposition of states that vary in energy (energetic disorder) and/or position (structural disorder). Although it is clear that variations in disorder(!) will lead to differences in admittance spectra, it is far from straightforward to present a quantitative interpretation in terms of energy and position when both are not known. In the theoretical literature, there exists a fierce discussion about the universal character of ac transport in disordered media that appears to be found experimentally.<sup>23</sup>

4: The *transit time effect* in single carrier space charge limited diodes can be observed. This effect is shown as a transition in the frequency domain the moment the charge carrier is not able to cover the distance between the two electrodes in one modulation period. The mobility of the charge carrier can then be derived from this transition (see chapter 6). The major advantage over *I-V* characterization is that the requirement of no trap states has become redundant.

5: The minority carrier contribution can be frequency resolved in the capacitance (see chapter 5) that allows for identification of the minority carrier mobility or the recombination rate in case assumptions are made about their functional dependence on field, temperature etc. In *I-V* characterization this contribution is clearly overshadowed by the majority carriers.

In this study, admittance measurements in the range of 5 Hz - 13 MHz are performed using a HP 4192A impedance analyzer. The analyzer can superimpose a bias voltage -35V to 35 V on top of the ac voltage.

The temperature was varied between 82-300 K in an optistat CF-V continuous flow cryostat that was purchased at Oxford Instruments together with the ITC601 temperature controller.

The *I-V* characterization was performed with either a home built setup (Chapter 3 and 4) or by a Keithley 2410 source meter (Chapter 4 and 5).

### 1.4.2 Modeling

A major contribution in the description of charge transport in this thesis comes from numerical simulations of the drift-diffusion equations that allow for a thorough interpretation of the experimental results. These equations are in fact based on the classical Boltzmann transport equation. Solutions to this equation can be provided by the method of moments that by choosing the number of moments allows one to decide on the complexity of the model. For the drift-diffusion equations the zeroth and first order moment have to be related.

The drift-diffusion equations are widely used to describe semiconductor devices. The set of coupled partial differential equations is given by the Poisson equation, continuity equations and transport equations:

$$\begin{aligned}\bar{\nabla} \cdot (\epsilon \bar{\nabla} \phi) &= q(n - p - C) \\ \bar{\nabla} \cdot \bar{J}_n &= q(\partial_t n + R) \\ \bar{\nabla} \cdot \bar{J}_p &= q(-\partial_t p - R) \\ \bar{J}_n &= q(D_n \bar{\nabla} n - \mu_n n \bar{\nabla} \phi) \\ \bar{J}_p &= q(-D_p \bar{\nabla} p - \mu_p p \bar{\nabla} \phi)\end{aligned}$$

where  $\phi$  denotes the electric potential,  $n$  and  $p$  are the free carrier concentrations of electrons and holes, and  $J_n$  and  $J_p$  are the electron and hole current density, respectively.  $D_n$ ,  $D_p$ ,  $\mu_n$  and  $\mu_p$  are the diffusion coefficients and the mobilities of electrons and holes, respectively.  $C$  is the net doping concentration,  $R$  the generation/recombination rate,  $\epsilon = \epsilon_r \epsilon_0$  with  $\epsilon_0$  the permittivity of vacuum and  $\epsilon_r$  the relative permittivity that is assumed constant. Often, the Einstein relation for diffusion,  $D_{n/p} =$

$k_B T/q \mu_{n/p}$ , is assumed to hold, where  $k_B$  is the Boltzmann constant,  $T$  the temperature and  $q$  the elementary charge. The bars depicted above the variables express their vector character.

The numerical solution of the drift-diffusion equations is far from trivial. In the 1980's, many conferences (NASECODE and SISDEP/SISPAD series) were held on the topic. The system of equations is singularly perturbed<sup>23</sup> and highly nonlinear. Dedicated numerical methods have been developed to solve the system, and they turn out to be essential for a robust and efficient solution. The Scharfetter-Gummel discretization scheme must be used to discretize the current densities, whereas damped Newton methods<sup>24</sup> or nonlinear variable transformations<sup>25</sup> are essential for the solution of the extremely nonlinear systems of discretized equations. A thorough description of all numerical methods used for semiconductor device simulation is given in ref. 20. The simulations described have been performed using the software package CURRY, developed within the Philips electronics company.

## 1.5 Elemental composition: ion beam analysis

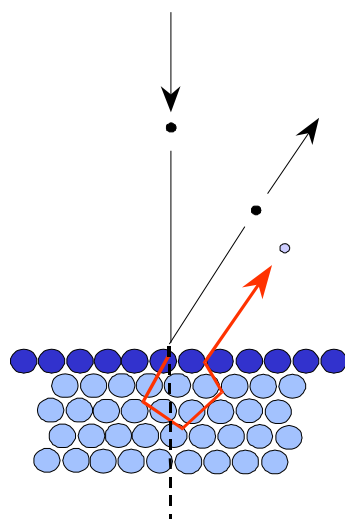


**Figure 7:** a schematic representation of low energy ion scattering

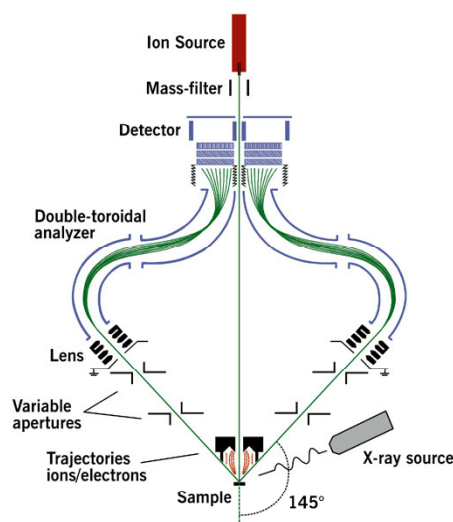


**Figure 8:** The design of the Eindhoven LEIS set-up.

In order to study the diffusion profiles of alkali metals into MDMO-PPV two different ion scattering techniques have been employed, viz. low energy ion scattering (LEIS) and neutral impact collision ion scattering spectroscopy (NICISS). Here, their operation principle and experimental setups are elucidated.

In LEIS, the elemental composition at the outermost surface is probed by analysis of the kinetic energy of noble gas ions that are elastically backscattered from the surface (figure 7).<sup>26</sup> For  $\text{He}^+$  the survival probability for maintaining its charged character during the scattering process amounts to  $10^{-4}$ - $10^{-2}$  for the outermost surface layer but decreases when the ions penetrate this layer ensuring surface sensitivity. However, the neutralized noble gas atoms that were scattered at deeper layers may reionize at the surface and contribute to the spectrum at lower energy. Due to the complexity of neutralization mechanisms an *ab-initio* quantification of LEIS spectra is practically undoable and hence calibration is required. In order to maximize the mass resolution of the target atoms, the mass, energy and scattering angle of the incoming ions may be varied. In the set-up, a mono energetic 3 keV  $^3\text{He}^+$  ion beam is employed and the applied ion dose is typically between  $10^{13}$  -  $10^{14}$  atoms/cm<sup>2</sup>. The kinetic energy of ions scattered by 145° is analyzed and detected by a



double toroidal analyzer (figure 8) and position sensitive detector<sup>27</sup> and allowed for a detection limit of 100 ppm in the outermost atomic layer in case of alkali atoms deposited on hydrocarbons.

By measuring the time-of-flight (TOF) of both the charged and neutralized noble gas ions, the composition in deeper layers can be studied with NICISS.<sup>28, 29</sup> Passage through the material induces inelastic losses due to small-angle scattering and electronic excitation (nuclear and electronic stopping power). In order to obtain absolute concentration-depth profiles, the stopping power in hydrocarbons<sup>30</sup>, the detector sensitivity and differential cross-sections must be determined.<sup>29</sup> In the NICISS measurements a mono energetic 4.5 keV  $^4\text{He}^+$  ion beam is employed with a maximum dose of  $5 \times 10^{13}$  atoms/cm<sup>2</sup>. In the set-up, the scattering angle is fixed at  $168^\circ$  with the analyzer detector orientation along the surface normal. The depth resolution is best near the surface and decreases slowly with depth ( $\leq 10 \text{ \AA}$  at 100  $\text{\AA}$  depth).<sup>29</sup> By integration of NICISS spectra we obtain the total amount of deposited alkali atoms up to a depth of 200  $\text{\AA}$ . In principle, these diffusion spectra can also be obtained by conducting LEIS experiments and using the energy resolved signal.

Ion scattering methods generally induce modifications in the chemical structure of polymer surfaces.<sup>31</sup> Hence in order to probe the intrinsic surface composition, a dose of  $\sim 10^{13}$  ions/cm<sup>2</sup> is permitted which allows for “static” conditions.<sup>32</sup> Although such a dose already damages the polymer, the spectra do not show any significant composition modification during the measurement. Surface charging appeared to be negligible for the applied film thickness due to the (semi-) conducting nature of MDMO-PPV.

## 1.6 Scope of this thesis

The emphasis of this thesis has focused on the understanding of interface phenomena (read diffusion) and their effect on charge transport in polymer opto-electronic devices. Semi-classical transport has been considered by matching solutions of the drift-diffusion equations with the experimental results of (time-dependent) electrical characterization. Interface effects were taken into account by incorporating diffusion profiles into the transport description. This then generally resulted in modifications of boundary conditions in terms of the charge and field distribution in the polymer structure.

In chapter two and three the LED performance of a polymer layer (MDMO-PPV) is investigated as a function of alkali metal concentration at the cathode. Here, Time-of-Flight (TOF) experiments were conducted and a trapping mechanism for the alkali cations is proposed that can account for the observed diffusion profiles. Electrical characterization has been modeled by incorporating these diffusion profiles as dopant layers. Moreover, a novel interpretation is presented for the admittance spectra typically observed for these polymer LED structures.

In chapter four the bulk-heterojunction solar cell is electrically characterized as a function of bias and temperature by photocurrent experiments. The field dependence of the photocurrent is used to determine the recombination mechanism. The temperature dependence allows for the characterization of the activated behavior of the electron and hole mobilities.

In chapter five the negative capacitance in admittance spectroscopy as often observed in semiconducting devices is explained within the drift-diffusion approximation. From these calculations scaling laws relating the frequency for which the capacitance has a transition from positive to negative values, with the electron and hole mobilities are presented in the limit of strong and zero recombination. Subsequently the minority carrier mobility and recombination rate constants are determined by admittance spectroscopy in both the polymer LED and bulk heterojunction solar cell.

In chapter six calculations based on the drift-diffusion equations are presented that can account for the behavior of the experimentally observed universal ac conductance in admittance spectroscopy as reported in literature. The explanation we present considers the space charge

distribution in the dielectric layer with one ohmic contact. Our description deviates from conventional models as it is shown that disorder is not a prerequisite for this ac behaviour.

The chapters of this thesis have been published as independent articles, or are prepared for individual publication in refereed journals. Therefore each of the following chapters can be read independently. Accordingly overlap between the chapters is unavoidable.

## 1.7 References and notes

- [1] C.K. Chiang, C.R. Fincher, Y.W. Park, A.J. Heeger, H Shirakawa, E.J. Louis, S.C. Gau, A.G. MacDiarmid, *Phys. Rev. Lett.* **39**, 1089 (1977).
- [2] J. Wayne Rabalais, *Principles and Applications of Ion Scattering Spectrometry: Surface Chemical and Structural Analysis*, (John Wiley & Sons, Inc., Hoboken, New Jersey, 2003)
- [3] J.-L. Brédas, J. Cornil, A.J. Heeger, *Adv. Mat.* **8**, 447 (1996).
- [4] N.S. Sariciftci (Ed.), *Primary Photoexcitations in Conjugated Polymers*, World Scientific, Singapore, 1997.
- [5] Jan-Willem van der Horst, *Ph.D thesis*, Technische Universiteit Eindhoven (2001).
- [6] H. Bässler, *Phys. Stat. Sol. B* **175**, 15 (1993).
- [7] S.V. Novikov, D.H. Dunlap, V.M. Krenke, P.E. Paris, A.V. Vannikov, *Phys. Rev. Lett.* **81**, 4472 (1998).
- [8] P.W.M. Blom, M.C.J.M. Vissenberg, *Phys. Rev. Lett.* **80**, 3819 (1998).
- [9] C. Tanase, E.J. Meijer, P.W.M. Blom, D.M. de Leeuw, *Phys. Rev. Lett* **91**, 216601 (2003).
- [10] Frank Pasveer, *Ph.D thesis*, Eindhoven University of Technology (2004).
- [11] J.H. Burroughes, D.D.C. Bradley, A.R. Brown, R.N. Marks, K. Mackay, R.H. Friend, P.L. Burn, A.B. Holmes, *Nature* **347**, 539 (1990).
- [12] A.J. Heeger, *Rev. Mod. Phys.* **73**, 681 (2000).
- [13] U. Wolf, V.I. Arkhipov, H. Bassler, *Phys. Rev. B.* **59**, 7507 (1999).
- [14] V.I. Arkhipov, U. Wolf, H. Bassler, *Phys. Rev. B.* **59**, 7514 (1999).
- [15] Hubert Martens, *Ph.D thesis*, University of Leiden (2000).
- [16] M. Pope and C.E. Swenberg, *Electronic Processes in Organic Crystals and Polymers*, 2<sup>nd</sup> ed. (Oxford University Press, Oxford, 1999).
- [17] C.J. Brabec, G. Zerza, G. Cerullo, S. De Silverstri, S. Luzzati, J.C. Hummelen, N.S. Sariciftci, *Chem. Phys. Lett.* **340**, 232 (2001).
- [18] T. Offermans, S.C.J. Meskers, R.A.J. Janssen, *J. Chem. Phys.* **119**, 10467 (2003).
- [19] I. Montanari, A.F. Nogueira, J. Nelson, J.R. Durrant, C. Winder, M.A. Loi, N.S. Sariciftci, C.J. Brabec, *Appl. Phys. Lett.* **81**, 3001 (2002).

- 
- [20] W.H.A. Schilders, *Numerical Methods for Semiconductor Device Simulation*, volumes I and II, Springer, Vienna (to appear)
- [21] P.A. Markowich, C.A. Ringhofer, and C. Schmeiser, *Semiconductor Equations*, Springer-Verlag, Vienna (1990)
- [22] P. Blood and J.W. Orton, *The Electrical Characterization of Semiconductors: Majority Carriers and Electron States*, (Academic Press, San Diego, 1992).
- [23] J.C. Dyre, and T.B. Schrøder, *Mod. Rev. Phys.* **72**, 873 (2000) and references therein
- [24] P.A. Markowich, *SIAM J. Appl. Math.* **5**, pp. 896-928 (1984).
- [25] R.E. Bank and D.J. Rose, *Numer. Math.* **37**, pp. 279-295 (1981).
- [26] S.J. Polak, C. den Heijer, W.H.A. Schilders, and P.A. Markowich, *Int. J. Numer. Methods Eng.*, **24**, pp. 763-838 (1987).
- [27] H.H. Brongersma, H.J. van Daal, *Analysis of Microelectronic Materials and Devices*, ch. 2.8, Ed. M. Grasserbauer and H.W. Werner, John Wiley and Sons (1991)
- [28] G.J.A. Hellings, H. Ottevanger, S.W. Boelens, C.L.C.M. Knibbeler, H.H. Brongersma, *Surf. Sci.* **162**, 913 (1985).
- [29] H. Niehus, G. Comsa, *Nucl. Instr. Meth.* **B15**, 122 (1986).
- [30] G. Andersson, H. Morgner, *Surf. Sci.* **405**, 138 (1998).
- [31] G. Andersson, H. Morgner, *Nucl. Instr. Meth.* **B155**, 357 (1999).
- [32] G. Marletta, *Nucl Instr. and Meth.* **B46**, 295 (1990).
- [33] P. Bertrand, Y. De Puydt, *Nucl. Instr. Meth.* **B78**, 181 (1993).



### Interface formation in K doped MDMO-PPV LEDs

#### Abstract

*Manufacturing of Al / K / MDMO-PPV / ITO LED structures by physical vapor deposition of K onto the emissive polymer layer has been characterized by electroluminescence and ion scattering spectrometry. Varying the deposited K areal density from  $3.9 \times 10^{12}$  to  $1.2 \times 10^{14}$  atoms/cm<sup>2</sup> the external efficiency rises from 0.01 to 1.2 cd/A. Spectra obtained by ion scattering analysis demonstrate the overall absence of K at the polymer outermost surface layer, and diffusion up to a depth of 200 Å. Depth profiles have been derived, and were modeled using an irreversible first order “trapping” reaction. Trapping may stem from confinement of the electron at a conjugated segment, that was donated through charge transfer typical for alkali /  $\pi$ -conjugated systems. This study demonstrates that evaporation of low work function metals onto organic systems does not result in simple stacked structures. The enhanced electroluminescence with submonolayer K deposition is attributed to the shift of the recombination zone away from the Al cathode, which is demonstrated to prevail over the known exciton quenching mechanism due to the formation of gap-states.*

## 2.1 Introduction

Conjugated organic materials have drawn much attention for their novel properties and technological potential in electronic devices. Since the discovery of electroluminescence (EL) in poly(p-phenylene vinylene) (PPV)<sup>1</sup>, many investigations have focused on the development of efficient polymer LEDs. An important aspect in this is the analysis of metal/organic interfaces, which play a major role in the conduction, efficiency and stability of the device. Contributions in this field arose among others from ultraviolet photoelectron spectroscopy (UPS), which demonstrated the formation of gap-states, (bi)polarons<sup>2-5</sup>, the failing of vacuum level alignment<sup>6, 7</sup> and energy level bending<sup>8</sup>. By photoluminescence (PL) experiments it was also shown that metal deposition resulted in exciton quenching by either directly introducing gap-states<sup>9</sup> or opening a non-radiative decay channel through energy transfer to a metal mirror<sup>10, 11</sup>. Recently, it was shown that the amount of Ca diffusing into the polymer during cathode deposition influences the electroluminescence<sup>12</sup>.

In order to estimate interface effects on the device performance, an important issue is the interface width. In typical modeling studies the extend of interfaces is often neglected and abrupt junctions are assumed<sup>13, 14</sup>. However, for metal atoms evaporated onto soft condensed layers thermodynamics indicates that this location is unstable and will diffuse to extensive depths, depending primarily on chemical reactivity and kinetics<sup>15</sup>. Experimental investigations are lacking, despite that one of the major improvements in performance has been achieved by the introduction of interfacial layers between the cathode and the conjugated polymers. Here distinction can be made between dopant layers<sup>16, 17</sup> and insulating layers<sup>18-21</sup>, where in the latter case still controversy exists about its operating mechanism.

Doping by physical vapor deposition of alkali metals has been established by UPS<sup>2-5</sup>. The alkali metal acts as a strong reducing agent that donates its electrons to the conjugated  $\pi$ -system, which in turn leads to the generation of the earlier mentioned (bi)polarons. These states in the previously forbidden electronic bandgap may effectively reduce the barrier height for electron injection. Taking into consideration that the efficiency in PPVs is restricted by an unbalanced charge transport as a result of the lower electron mobility compared to the hole mobility, alkalis are expected to enhance the device performance significantly. In addition Cao *et al.*<sup>16</sup> demonstrated an enhanced device stability with increasing alkali cation size and suggested an increased diffusion barrier underlying this observation. Diffusion of K in both PPV and poly (2-methoxy-5-(2'-ethyl-hexyloxy)-1,4-phenylene vinylene) (MEH-PPV) has in fact been identified by angle-resolved X-ray photoelectron spectroscopy (XPS)<sup>22</sup>. However the XPS probe depth is confined to a range of 5-20 atomic layers with a maximum sensitivity of 1 at%. Thus, qualitative information is difficult to extract and quantitative diffusion profiles were not determined.

Although this brief overview points to a correlation between metal diffusion and conductivity and radiative recombination in PPVs, no direct evidence has been established. Also literature on alkali metals employed as electron injection electrode in LEDs<sup>16, 23</sup> is rather limited. Here, we will focus on K deposited onto poly(dialkoxy-p-phenylene vinylene) MDMO-PPV<sup>24</sup> by physical vapor deposition. The interface formation is studied by inspection of the K distribution in MDMO-PPV using ion scattering analysis techniques and diffusion profiles are extracted. The results are correlated to the LED performance derived from EL measurements.

## 2.2 Experimental

### 2.2.1 Sample preparation and electroluminescence

ITO-coated glass substrates were cleaned in ultrasonic baths of acetone and propanol for 30 min each. Subsequently they were introduced into the UV-ozone cleaning chamber, which is directly attached to a glovebox ( $[O_2] < 1$  ppm and  $[H_2O] < 1$  ppm)<sup>25</sup>. After 30 minutes of UV-ozone treatment, hydrocarbons were effectively removed from the substrates, the chamber was evacuated, refilled with nitrogen and the substrates were transferred into the glovebox setup. An MDMO-PPV 0.7 wt % toluene solution was heated at 50° C for 1 h and cast at a spin rate of 3100 rpm. Typical film thicknesses were determined to be  $120 \pm 10$  nm by an alpha-stepper (Alpha-step 200 Tencor Instruments). By means of a load lock these samples were introduced into an UHV vapor deposition chamber (base pressure  $10^{-9}$  mbar) without being exposed to air. The cathodes were deposited through a shadow mask that defined six diodes per substrate with an active area of  $24 \text{ mm}^2$ . K was deposited from an alkali metal dispenser purchased from Saesgetters ( $\sim 800^\circ \text{ C}$ ;  $2 \times 10^{-9}$  mbar) at room temperature. For the LED's an Al capping layer ( $\sim 80$  nm) was deposited by evaporation ( $\sim 1 \text{ \AA/s}$ ) at about  $40^\circ \text{ C}$  while the thickness was monitored using a quartz crystal ( $1250^\circ \text{ C}$ ;  $10^{-7}$  mbar). Directly after lowering the temperature of the Al effusion cell to  $600^\circ \text{ C}$ , EL measurements were conducted in an *in-situ* setup in the evaporation chamber at a temperature of  $36^\circ \text{ C}$ . Several runs were repeatedly made with increasing evaporation time for K. In case of the ion scattering analysis the Al capping layer was omitted and samples were transported in an airtight suitcase to the ion scattering setups. In the case of the NICISS measurements the samples had to be brought into contact with air for several minutes.

#### 2.2.1. Ion scattering spectrometry

In order to study K diffusion into MDMO-PPV, two different ion scattering techniques have been employed, viz. low energy ion scattering (LEIS) and neutral impact collision ion scattering spectroscopy (NICISS).

LEIS probes the elemental composition of the topmost atomic layer: the mass of the surface atoms is determined from analysis of the kinetic energy of elastically backscattered noble gas ions, while efficient neutralization of the ions ensures the surface sensitivity<sup>26</sup>. LEIS measurements were performed in a UHV system with a base pressure of  $2 \times 10^{-10}$  mbar. A mono energetic 3 keV  $^3\text{He}^+$  ion beam was employed and the applied ion dose was typically between  $10^{13}$  -  $10^{14}$  atoms/cm<sup>2</sup>. In the set-up, the kinetic energy of ions scattered by  $145^\circ$  was analyzed and detected by a double toroidal analyzer and position sensitive detector<sup>27</sup> and allowed for a detection limit of 100 ppm in the case of K.

By measuring the time of flight (TOF) of the charged plus neutralized noble gas ions, the composition in deeper layers can be studied with NICISS<sup>28,29</sup>. Passage through the material induces additional inelastic losses due to small-angle scattering and electronic excitation (nuclear and electronic stopping power). In order to obtain absolute concentration-depth profiles, the stopping power in hydrocarbons<sup>30</sup>, the detector sensitivity and differential cross-sections must be taken into account<sup>29</sup>. NICISS measurements were conducted in a high vacuum system with a base pressure of  $\sim 4 \times 10^{-6}$  mbar. A mono energetic 4.5 keV  $^4\text{He}^+$  ion beam was employed with a maximum dose of  $5 \times 10^{13}$  atoms/cm<sup>2</sup>. In this set-up, the scattering angle is fixed to  $168^\circ$  with the analyzer detector orientation along the surface normal. The concentration sensitivity is also close to 100 ppm for K. The depth resolution is best near the surface and decreases slowly with depth ( $\leq 10 \text{ \AA}$  at  $100 \text{ \AA}$  depth)<sup>29</sup>. By integration of a NICISS spectrum we obtain the total amount of deposited K up to a depth of  $200 \text{ \AA}$ .



Ion scattering methods generally induce modifications in the chemical structure of polymer surfaces<sup>31</sup>. Hence in order to probe the intrinsic surface composition, a maximum dose of  $\sim 10^{13}$  ions/cm<sup>2</sup> is permitted which allows for “static” conditions<sup>32</sup>. Although such a dose already does some damage to the polymer, the spectra do not show any significant composition modification during the measurement. Surface charging appeared to be negligible for the applied film thickness due to the conducting property of MDMO-PPV.

## 2.3 Results

### 2.3.1 Electroluminescence

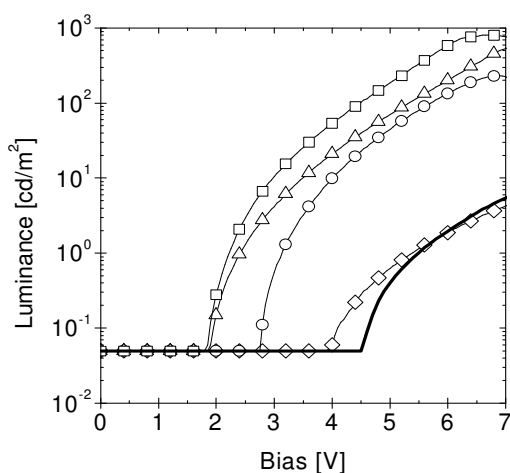


**Figure 1:** Electroluminescence (EL) versus bias on Al / K / MDMO-PPV / ITO stacked structures with varying deposition coverage:  $3.9 \times 10^{12}$  (diamonds),  $2.0 \times 10^{13}$  (circles),  $3.4 \times 10^{13}$  (triangles) and  $1.0 \times 10^{14}$  K (squares) atoms/cm<sup>2</sup> and without K (thick solid curve).

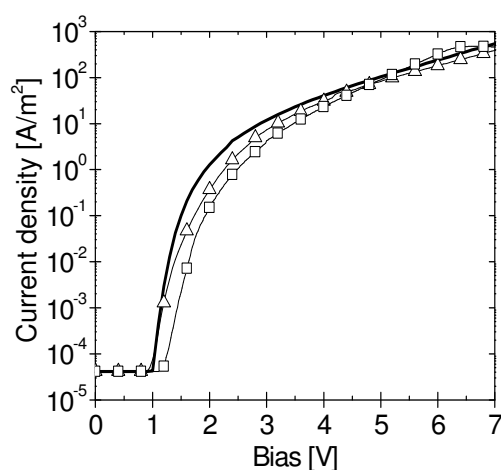


**Figure 2:** Current voltage characteristics on Al / K / MDMO-PPV / ITO LED structures with varying deposition coverage:  $3.9 \times 10^{12}$  (triangles) and  $1.2 \times 10^{14}$  (squares) atoms/cm<sup>2</sup> and without K (thick solid curve). At a coverage of  $3.4 \times 10^{13}$  atoms/cm<sup>2</sup> or more the current onset remains at 1.45 V.

The luminance and current versus bias are shown in figures 1 and 2 for different amounts of deposited K. A dramatic increase of more than two orders of magnitude in light output with increasing K deposition is observed. The light onset shifts from 4.50 V down to 1.85 V, the latter corresponding to the lowest conceivable onset potential for radiative emission of the polymer layer ( $\lambda_{\text{max}} = 630$  nm, see fig 3). Already at a deposition of  $2.0 \times 10^{13}$  atoms/cm<sup>2</sup> the current onset has shifted from  $1.00 \pm 0.05$  to  $1.25 \pm 0.05$  V, resulting in a reduced current at low bias, which converges to its original value with increasing bias. This effect will be explained by an increase in built-in potential in the subsequent discussion. The maximum efficiency increases from 0.01 to 1.2 cd/A and saturates at higher amounts of deposition (figure 4). Moreover the bias at which this maximum is obtained decreases with K coverage to almost 2.0 V, which is close to the light onset. Obviously, the amount of K deposition dictates the device performance and hence, this regime is relevant in order to study the associated depth profiles.

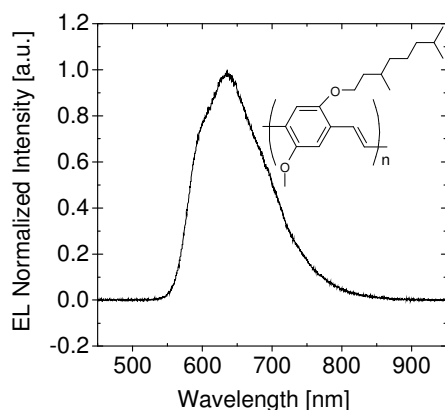


**Figure 3:** EL spectrum normalized to its peak height for  $1.0 \times 10^{14}$  K atoms/cm<sup>2</sup>. Inset gives the chemical structure of MDMO-PPV.

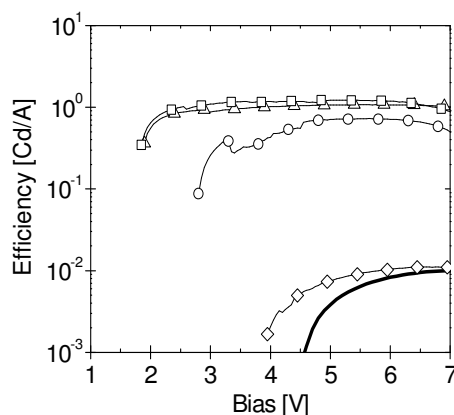


**Figure 4:** Efficiency of Al / K / MDMO-PPV / ITO LED structures with varying deposition coverage:  $3.9 \times 10^{12}$  (diamonds),  $2.0 \times 10^{13}$  (circles),  $3.4 \times 10^{13}$  (triangles) and  $1.0 \times 10^{14}$  K (squares) atoms/cm<sup>2</sup> and without K (thick solid curve).

### 2.3.2 Ion scattering spectrometry

Figure 5 shows two LEIS spectra of MDMO-PPV / ITO substrates with different amounts of K deposition. The C and O surface peaks are the main features in the spectrum. The absence of a peak at 2265 eV, indicated by the arrow in the figure, shows that K completely diffuses into the polymer. We observe a continuous background starting at 2265 eV due to reionisation of the neutral atoms, which were scattered in deeper layers. The extent of this signal indicates K diffusion up to at least 100 Å, but possibly much deeper. The increasing background at ion energies below 1000 eV originates from detection of ionized hydrogen recoils. In order to compare the C and O signals for different K coverages a LEIS spectrum with pristine MDMO-PPV is shown in the inset. After a correction for the increased background due to the diffusion of K, both surface peaks remain similar, confirming the absence of K at the outermost surface layer.

Figure 6 shows two NICISS spectra: one for the pristine MDMO-PPV substrate and one for the K / MDMO-PPV system. In these spectra each compositional element is identified as a step in the TOF signal and can be traced until the next element (with lower mass number) appears. The step due to the presence of K is clearly visible in the uppermost spectrum. The photon peak shown in the spectrum is produced by inelastic processes that involve outer shell electrons from incident and target particles<sup>33</sup> and is employed for time calibration  $t = 0$ <sup>29</sup>. The NICISS signal starting at 3 μs increases as a result of hydrogen recoils that contribute to the

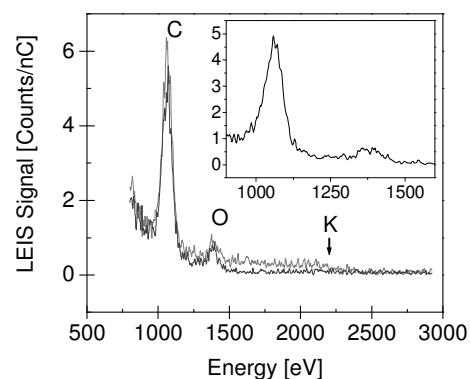


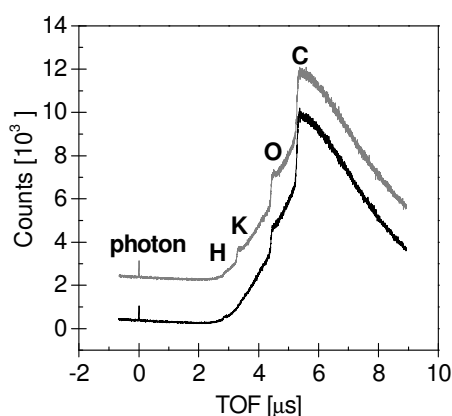
**Figure 5:** Low energy ion scattering (LEIS) spectra obtained from K / MDMO-PPV / ITO stacking structures. Two spectra are shown with different quantities of deposited K atoms/cm<sup>2</sup> (black:  $0.71 \times 10^{14}$  at/cm<sup>2</sup>; grey:  $1.2 \times 10^{14}$  at/cm<sup>2</sup>) and one with pristine MDMO-PPV (inset).

spectrum in both ionized and neutral form. Their presence in the spectrum remains over the complete time scale<sup>29</sup>.

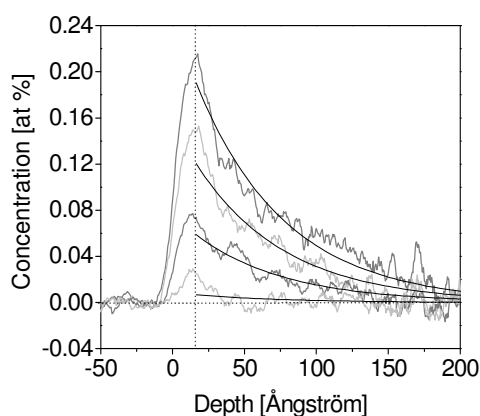
In order to obtain the depth profiles for K, the NICISS signal of pristine MDMO-PPV is subtracted from the reference MDMO-PPV / K spectrum. The depth scale for K is derived from the time of flight scale taking into account the stopping power of the projectiles in the hydrocarbons<sup>30</sup>. The inelastic loss of energy during back scattering off K was assumed to be 10 eV. Since it was not measured during the experiments the leading mark of the depth scale can be determined only with an accuracy of  $\pm 2$  Å. The K concentration is determined by relating the count rate to the C signal including corrections for the C atomic fraction ( $\Phi_C = 39\%$ ) and the differential cross sections.

Figure 7 shows the concentration-depth profiles for K / MDMO-PPV structures with increasing amounts of K deposition. The profiles show that the K concentration increases from negligible at the surface to a maximum at a depth of 16 Å. For depths larger than 16 Å the K concentration decreases. The profiles are not significantly influenced by the depth resolution: deconvoluted depth profiles as calculated using an algorithmic deconvolution procedure for a Gaussian distribution function with FWHM of 9.3 Å for K, are nearly identical to the measured data. Comparing the concentration profiles together with the time difference between manufacturing and analyzing the substrates (see caption figure 7) it is evident that the diffusion profiles are irrespective of time. Thus at the moment we conduct the ion scattering investigations the K concentrations are metastable and diffusion has stopped. Therefore, we must include a trapping mechanism in order to describe the diffusion.

The diffusion process was thus modeled by assuming Fickian diffusion in a semi-infinite plane from an instantaneous source with an irreversible first order “trapping” reaction<sup>34</sup>:



**Figure 6:** Neutral impact collision ion scattering spectroscopy (NICISS) on an MDMO-PPV / ITO stacking structure with K deposition (upper) and without (lower). For clarity the upper spectrum is raised by 2000 counts.



**Figure 7:** K diffusion profiles determined by NICISS (smoothed over 10 data points). The total deposition is calculated by integration of the spectra and amounts (from top to bottom) to  $1.2 \times 10^{14}$ ,  $7.1 \times 10^{13}$ ,  $3.5 \times 10^{13}$  and  $3.9 \times 10^{12}$  atoms/cm<sup>2</sup>. The time between manufacturing and conducting the ion scattering measurements is 2, 18, 18 and 6 days respectively. The solid curves through the spectra are fits to an exponential decay function with a characteristic decay length of 62 Å.

$$\partial C/\partial t = D \partial^2 C / \partial x^2 - k C, \quad (1)$$

which equals zero in case we consider the steady state situation. We assume this diffusion to begin at the observed maximum (16 Å below the surface). Here  $k$  and  $D$  are the trapping and chemical diffusion constant respectively and  $C(x)$  the K concentration as a function of depth  $x$ . The solution to this differential equation is

$$C(x) = M q \exp(-q x) \text{ for } (x > 0), \quad (2)$$

where  $M$  is the total amount of diffusing substance and  $q = (k/D)^{1/2}$ . From the resulting fits shown in figure 7 the characteristic decay length,  $1/q$ , is determined to be independent of K concentration and amounts to 62 Å.

In short, we note that in K / MDMO-PPV systems both in- and bulk diffusion are substantial. Moreover, in comparison with the emissive layer of 1000 Å, the 200 Å at which K is detected is significant. The depth profile is approximated by an exponential decaying concentration with its maximum below the polymer surface at ~ 16 Å. The depth at which this maximum occurs is likely related to the length of the aliphatic side groups as explained in the next section.

## 2.4 Discussion

### 2.4.1 Diffusion profile

In the following section we differentiate between two diffusion processes, which we refer to as in-diffusion and bulk diffusion. In order to minimize the free energy the main contribution stems from the surface energy: the component with highest surface energy will diffuse into the other component until it is completely screened from the vacuum and the surface energy is minimized: we will refer to this as in-diffusion. A minor contribution to the free energy originates from the increase in entropy by lowering the concentration gradient in the system, which results in bulk diffusion. In addition, the free energy is also lowered by the decrease in chemical potential through charge transfer between the components.

The driving force for in-diffusion is the difference in surface energy between the metal particles,  $\gamma_M$ , on one side and the polymer surface energy,  $\gamma_P$ , and the interfacial energy,  $\gamma_{MP}$ , on the other. In-diffusion occurs in case the inequality  $\gamma_M > \gamma_P + \gamma_{MP}$  holds. In general the surface energy for polymers is much lower than that for metals (for PPV  $\gamma_P \approx 30 - 40 \text{ mJ/m}^2$  and for K  $\gamma_M \approx 150 \text{ mJ/m}^2$ ). An estimate for the interfacial energy for a range of polymer/inorganic material combinations is given for instance by Fowkes<sup>35</sup> and the inequality holds for most systems. In general, kinetics, determined by substrate temperature and deposition rate, may prevent diffusion in the polymer leading to aggregation<sup>36</sup>.

The K depth profiles shown in fig. 7 clearly indicate that the subsurface concentration is higher than the surface concentration. The LEIS spectrum even demonstrates the complete absence of K at the outermost surface layer within the detection limit of 100 ppm and therefore in-diffusion has been established. Whether the atoms at the surface diffuse by available vacancies within the polymer matrix or whether they are immediately covered by aliphatic groups in order to lower the surface energy cannot be deduced from these experiments. It should be noted that the maximum K concentration does not occur just below the surface, but somewhat deeper (16 Å). As soon as the K is situated more than roughly 4 Å below the surface, the surface free energy has already been significantly reduced. The observation that the maximum K concentration occurs deeper than this, indicates that the position of this maximum must result from the details of diffusion and trapping mechanisms. A likely explanation is that the aliphatic groups are oriented at a small angle with the

surface normal and as a result the conjugated segments, that act as trapping sites, are located deeper in the bulk.

Bulk diffusion of K extends over a range of 200 Å and detection beyond this depth is limited by our experimental method. As the diffusion profiles do not seem to be affected by time (days), we assume a stationary K distribution, from which the importance of trapping then immediately can be concluded. In absence of trapping the depth profiles should have converged to a spatially homogenous distribution over time, which we do not observe.

UPS measurements have clearly shown that charge transfer occurs between the K and the conjugated backbone of the polymer, resulting in doping induced gap states<sup>4</sup>. The maximum doping level occurred at one K atom per monomer repeating unit, which assures that complete charge transfer occurs in the samples studied here. This charge transfer will also have an immediate effect on diffusion: since cations repel each other their diffusion is not impeded by the formation of immobile clusters and in addition, as bulk diffusion is generally considered to proceed through the mechanism of vacancy hopping, the smaller ion size compared to their neutral form promotes diffusion as well<sup>15</sup>.

The repulsive Coulomb interaction between cations does not significantly affect the observed depth profiles, as electrons donated to the  $\pi$ -conjugated system will attempt to screen these positive sites and freely rotating dipoles are formed. The average potential energy decays as  $1/r^6$  and compared to the kinetic energy term of  $3/2 kT$ , becomes negligible at length scales in the order of Angströms. Here  $r$  is the distance between two dipoles,  $k$  is the Boltzmann constant and  $T$  the temperature ( $= 293$  K). An explanation for trapping may be found in the density of defects, which limits the conjugation length. The electrons will be localized to typically 6-10 monomer units and due to electrostatic forces the ion diffusion is restricted. The length of such a conjugated segment (estimated at 50 Å using the length of 6.3 Å for one monomer unit) and their random orientation with respect to the surface is in reasonable agreement with the characteristic length of 62 Å for the decaying exponential we obtained for fitting. This of course only holds when charge transfer results on a time scale much smaller than diffusion.

#### 2.4.2 Electroluminescence

Here the effect of chemical (charge transfer) doping leading to the enhanced performance is discussed in terms of the electronic transport.

Generally, the built-in potential is approximated by the difference in work function of anode and cathode<sup>37</sup>, assuming vacuum level alignment at the metal – polymer interfaces<sup>6</sup>. However, the overall absence of K at the surface (fig 5) rules out the explanation of matching the LUMO of MDMO-PPV to the work function of a metallic K layer. This is confirmed by UPS studies<sup>2, 3</sup>: a decreasing work function due to alkali deposition is exclusively measured at alkali densities much higher than used here (10 at% and 40 at% for Rb<sup>3</sup> and Na<sup>2</sup> respectively). The formation of (bi)polaron states leads to a shift of the Fermi energy level to lower binding energy close to the polymer surface<sup>3</sup>. The Fermi level of Al will be able to align to this Fermi energy level and consequently we ascribe the increase in built-in potential of 250 mV to a transition from vacuum level to Fermi level alignment as has been observed before by Greczynski *et al*<sup>38</sup>.

The enhanced luminescence could partly be explained by the increased built-in potential, for the alignment of the Al work function to the increased polymer Fermi energy level will lower the barrier for electron injection. However, this cannot explain the concentration dependent luminescence upon further deposition, as the current onset remains unaffected.

It was experimentally determined that as a consequence of difference in carrier mobility in PPVs,  $I$ - $V$  characteristics for double injection structures are dominated by the hole current density<sup>14</sup>. Therefore, electron-hole recombination occurs close to the polymer/cathode interface as was shown by model calculations for a pLED with either ohmic or tunneling contacts<sup>39, 40</sup>. In addition non-

radiative energy transfer for emitting dipoles as a function of distance from a metallic mirror has been experimentally demonstrated and its impact on the radiative recombination efficiency for MEH-PPV ranged up to 60 nm from the Al cathode<sup>11</sup>. Accordingly we attribute our increase in EL (efficiency) with increasing K deposition to a *shift* of the recombination zone away from the cathode.

Chemical doping of the polymer surface layer by K deposition may lead to three physical mechanisms, each of which is able to account for this shift: 1) an enhanced electron injection; 2) an increase in electron mobility due to the newly formed electronic states close to the LUMO and 3) the presence of donor electrons that are available for recombination in the polymer layer through doping (through the formation of recombination centers).

The first two mechanisms can potentially be observed by electrical characterization. However, the analytical solution to the problem of double injection into an insulator in steady state<sup>41</sup> shows that the hole current prevalence over the total current remains even for an increase of electron current by two orders of magnitude.<sup>42</sup> Thus in order to demonstrate the validity of either of these two possibilities one should attempt to reduce the hole current by increasing its injection barrier or, better, by manufacturing an electron only device.

For the luminescence properties the exact concentration-depth profile will be important and should be taken into account in case the second and third mechanism apply: in general the bandwidth of the density of states introduced by doping is concentration dependent and should be reflected in the electron mobility. Also, the position of the donated electrons, where excitons may be formed, will closely correspond to that of the K cations in the interfacial region and hence may dictate the non-radiative energy transfer to the Al mirror. The data presented here do not allow for any discrimination between these mechanisms and further qualification of the electronic transport is thus omitted.

The above mentioned mechanisms responsible for the increase in EL are based on the occurrence of charge transfer and subsequently the formation of gap states. At first glance this is in contradiction with earlier reports where in fact these gap-states were assigned to quench the PL in PPV derivatives<sup>9</sup>. Moreover it was demonstrated that by removing these states by oxidation the PL<sup>9</sup> property could recover. However, since it is known that Al neither diffuses<sup>43</sup> nor introduces these gap-states<sup>4</sup> and merely opens a non-radiative decay channel<sup>11</sup>, we propose that for the EL a shift of the recombination zone away from the Al cathode is dominant over the exciton quenching mechanism by the formation of gap states at submonolayer deposition.

Cao *et al.*<sup>16</sup> discussed the relation between device performance and the extension of the alkali doping region: they speculated that the diffusion rate is a much more important factor than the alkali work function during degradation. Our results confirm this, since we observe that even sub-monolayers at room temperature result in a diffusion region of about 200 Å. Cao *et al.* did not observe such concentration dependent behavior as reported here, but demonstrated that due to alkali deposition beyond 100 Å the PL efficiency severely decreased, which they attributed to quenching. We did not observe a decrease in EL efficiency, however it should be pointed out that our K coverage was far below this 100 Å.

## 2.5 Conclusion

The introduction of K onto poly(dialkoxy-p-phenylene vinylene) (MDMO-PPV) by physical vapor deposition has been applied in polymer LEDs, using ITO and Al as the anode and cathode respectively. The stacking structures were characterized by LEIS, NISS and EL in order to study the interface of the alkali / PPV system in relation to its performance.

The complete absence of K at the polymer surface and bulk diffusion up to 200 Å at a K concentration of  $1.2 \times 10^{14}$  atoms/cm<sup>2</sup> was established by ion scattering analysis. Depth profiles have been extracted from the NISS spectra, and bulk diffusion was modeled by introducing a trapping

parameter. A characteristic decay length of 62 Å was determined, and it was speculated that the confined conjugation length is the source for trapping and determines the decay length.

EL measurements clearly demonstrate a concentration dependent behavior: with increasing deposition an enhancement in luminescence and efficiency was observed (more than two orders in magnitude). The observed increase in built-in potential can at most partially account for this effect. We propose that the deposition of K actually results in a shift of the recombination zone, which can be either due to an improved charge balance or the presence of recombination centers in the interfacial layer. This will be pursued in further investigations.

In contrast to the common assumption in modeling charge carrier dynamics in polymer LED's, this study clearly indicates that physical vapor deposition of alkali metals (similar to earth alkaline metals)<sup>44</sup> onto soft condensed systems cannot generally be depicted as simple layered stacking structures. Moreover, we demonstrate that the formation of gap-states in the polymer layer results in an increased EL for deposition coverage up to  $1.2 \times 10^{14}$  atoms/cm<sup>2</sup> and that the gap state induced quenching mechanism as was pointed out by Park *et al*<sup>9</sup>, is of secondary importance compared to the non-radiative decay by energy transfer to the Al mirror.

## 2.6 Reference and notes

- [1] J.H. Burroughes, D.D.C. Bradley, A.R. Brown, R.N. Marks, K. Mackay, R.H. Friend, P.L. Burn, A.B. Holmes, *Nature* **347**, 539 (1990).
- [2] M. Fahlman, D. Beljonne, M. Lögdlund, R.H. Friend, A.B. Holmes, J.L. Brédas, W.R. Salaneck, *Chem Phys. Lett.* **214**, 327 (1993).
- [3] G. Iucci, K. Xing, M. Lögdlund, M. Fahlman, W.R. Salaneck, *Chem. Phys. Lett.* **244**, 139 (1995).
- [4] J. Birgerson, M. Fahlman, P. Bröms, W.R. Salaneck, *Synth. Met.* **80**, 125 (1996).
- [5] G. Greczynski, M. Fahlman, W.R. Salaneck, *Appl. Surf. Sci.* **166**, 380 (2000).
- [6] H. Ishii, K. Sugiyama, E. Ito, K. Seki, *Adv. Mater.* **11**, 605 (1999).
- [7] I.G. Hill, A. Rajagopal, A. Kahn, Y. Hu, *Appl. Phys. Lett.* **73**, 662 (1998).
- [8] J. Yoon, J.J. Kim, T.W. Lee, O.O. Park, *Appl. Phys. Lett.* **76**, 2152 (2000).
- [9] Y. Park, V.-E. Choong, B.R. Hsieh, C.W. Tang, Y. Gao, *Phys. Rev. Lett.* **78**, 3955 (1997)
- [10] Y. Park, V. Choong, E. Ettetdgui, Y. Gao, B.R. Hsieh, T. Wehrmeister, K. Müllen, *Appl. Phys. Lett.* **69**, 1080 (1996).
- [11] H. Becker, S.E. Burns, R.H. Friend, *Phys. Rev. B* **56**, 1893 (1997).
- [12] G.G. Andersson, H.H.P. Gommans, A.W. Denier van der Gon, H.H. Brongersma, *J. Appl. Phys.* **93**, 3299 (2003).
- [13] P.S. Davids, I.H. Campbell, D.L. Smith, *J. Appl. Phys.* **82**, 6319 (1997).
- [14] P.W.M. Blom, M.J.M. de Jong, *IEEE J. of Sel. Top. In Quant. Elec.* **4**, 105 (1998).
- [15] F. Faupel, *Low-Dielectrics Constant Materials IV*, Symposium. Mater. Res. Soc. Warrendale, PA, USA, p.15-26, 1998.
- [16] Y. Cao, G. Yu, I.D. Parker, A.J. Heeger, *J. Appl. Phys.* **88**, 3618 (2000).
- [17] H.M. Lee, K.H. Choi, D.H. Hwang, L.M. Do, T. Zyung, J.W. Lee, J.K. Park, *Appl Phys. Lett* **72**, 2382 (1998).
- [18] Y.E. Kim, H. Park, J.J. Kim, *Appl. Phys. Lett.* **69**, 599 (1996).
- [19] J. Yoon, J.J. Kim, T.W. Lee, O.O. Park, *Appl. Phys. Lett.* **76**, 2152 (2000).
- [20] P. Piromreun, H.S. Oh, Y. Shen, G.G. Malliaras, J.C. Scott, P.J. Brock, *Appl. Phys. Lett.* **77**, 2403 (2000).



- [21] T. M. Brown, R.H. Friend, I.S. Millard, D.J. Lacey, J.H. Burroughes, F. Cacialli, *Appl. Phys. Lett.* **79**, 174 (2001).
- [22] S. Li, E.T. Kang, K.G. Neoh, Z.H. Ma, K.L. Tan, W. Huang, *Appl. Surf. Sci.* **181**, 201 (2001).
- [23] J. Birgerson, F. J. J. Janssen, A. W. Denier van der Gon, Y. Tsukahara, K. Kaeriyama, W. R. Salaneck, *Synth. Met.* **132**, 57 (2002)
- [24] D. Braun, E.G.J. Staring, R.C.J.E Demandt, G.L.J. Rikken, Y.A.R. Kessener, A.H.J. Venhuizen, *Synth. Met.* **66**, 75 (1994).
- [25] G.G. Andersson, M.P. de Jong, F.J.J. Jansen, J.M. Sturm, L.J. van IJzendoorn, A.W. Denier van der Gon, M.J.A. de Voigt, H.H. Brongersma, *J. Appl. Phys.* **90**, 1376 (2001).
- [26] H.H. Brongersma, P.M. Mul, *Chem. Phys. Lett.* **14**, 380 (1973).
- [27] G.J.A. Hellings, H. Ottevanger, S.W. Boelens, C.L.C.M. Knibbeler, H.H. Brongersma, *Surf. Sci.* **162**, 913 (1985).
- [28] H. Niehus, G. Comsa, *Nucl. Instr. Meth.* **B15**, 122 (1986).
- [29] G. Andersson, H. Morgner, *Surf. Sci.* **405**, 138 (1998).
- [30] G. Andersson, H. Morgner, *Nucl. Instr. Meth.* **B155**, 357 (1999).
- [31] G. Marletta, *Nucl Instr. and Meth.* **B46**, 295 (1990).
- [32] P. Bertrand, Y. De Puydt, *Nucl. Instr. Meth.* **B78**, 181 (1993).
- [33] N.H. Tolk, J.L. Tully, W. Heiland, C.W. White, *Inelastic Ion-Surface Collisions*, Academic Press, New York, p. 201, 1977.
- [34] J. Crank, *The Mathematics of Diffusion*, Oxford University Press, 2<sup>nd</sup> ed. Bristol, p. 329, 1975.
- [35] F.M. Fowkes, *Ind. Eng. Chem.* **56**, 40 (1964).
- [36] G.J. Kovacs, P.S. Vincett, *J. Coll. Int. Sci* **90**, 335 (1982).
- [37] G.G. Malliaras, J.R. Salem, P.J. Brock, J.C. Scott, *Phys. Rev. B* **58**, R13411 (1998).
- [38] G. Greczynski, Th. Kugler, W.R. Salaneck, *J. Appl. Phys.* **88**, 7187 (2000).
- [39] P.W.M. Blom, M.C.J.M. Vissenberg, J.N. Huiberts, H.C.F. Martens, H.F.M. Schoo, *Appl. Phys. Lett.* **77**, 2057 (2000).
- [40] G.G. Malliaras, J.C. Scott, *J. Appl. Phys.* **83**, 5399 (1998).
- [41] R.H. Parmenter, W. Ruppel, *J. Appl. Phys.* **30**, 1548 (1959).

[42] Applying the measured mobilities for both holes and electrons at MDMO-PPV as a function of bias from 13.

[43] M. Atreya, S. Li, E.T. Kang, K.G. Nech, Z.H. Ma, K.L. Tan, J. Vac. Sci. Technol. A **17**, 853 (1999).

[44] F.J.J. Janssen, A.W. Denier van der Gon, L.J. van IJendoorn, R. Thoelen, M.J.A. de Voigt, H.H. Brongersma, Appl. Surf. Sci. **241**, 335 (2005).



### Interface formation in Cs doped MDMO-PPV LEDs

#### Abstract

*Al / Cs / MDMO-PPV / ITO LED structures, made by physical vapor deposition of Cs on the emissive polymer layer, have been characterized by electroluminescence, current-voltage and admittance spectroscopy. Deposition of Cs is found to improve the balance between electron and hole currents, enhancing the external electroluminescence efficiency from 0.01 cd/A for the bare Al cathode to a maximum of 1.3 cd/A for a Cs coverage of only  $1.5 \times 10^{14}$  atoms/cm<sup>2</sup>. By combining I-V and admittance spectra with model calculations, in which Cs diffusion profiles are explicitly taken into account, this effect could be attributed to a potential drop at the cathode interface due to a Cs-induced electron donor level 0.61 eV below the LUMO. In addition, the admittance spectra in the hole dominated regime are shown to result from space charge limited conduction combined with charge relaxation in trap levels. This description allows the direct determination of the carrier mobility, even in the presence of traps. In contrast to recent literature, it is demonstrated that there is no need to include dispersive transport in the description of the carrier mobility to explain the excess capacitance that is typically observed in admittance spectra of  $\pi$ -conjugated materials.*

### 3.1 Introduction

Since the discovery of the luminescent properties of poly(p-phenylene vinylene) (PPV) there has been an increasing interest for its application in devices such as polymer light-emitting diodes (pLEDs) and solar cells<sup>1</sup>. In order to understand the charge transport properties of this type of  $\pi$ -conjugated material, many investigations have recently been conducted by time-of-flight (TOF), current-voltage characterization ( $I$ - $V$ ) or admittance spectroscopy<sup>2-6</sup>. These techniques introduce charge carriers either by photo absorption (photodoping) or injection from metallic contacts. Generally, the interpretation of these experiments suffers from simplifications concerning the metal-polymer interface: abrupt compositional junctions without chemical interaction and alignment of the vacuum energy level are normally assumed.

The electron injecting contact of the pLED is typically manufactured by vapor deposition of a low work function metal onto the polymer layer. By photoelectron spectroscopy chemical (charge transfer) doping and the subsequent formation of (bi)polaron states<sup>7-11</sup> have been identified upon deposition of alkali(ne) (earth) metals onto  $\pi$ -conjugated systems. Recently, we have demonstrated diffusion up to 200 Å for *sub-monolayer* deposition of K by ion scattering spectroscopy<sup>12</sup>. Simultaneously, the electroluminescence and efficiency increased by two orders of magnitude.

In order to understand how chemical doping and diffusion at the electron injecting contact affect the charge transport and device performance we will study the Cs / MDMO-PPV interface in LED structures by combination of electrical characterization (electroluminescence,  $I$ - $V$  and admittance spectroscopy) with analytical and numerical models and ion scattering spectrometry.

### 3.2 Experimental

In a glovebox filled with a nitrogen atmosphere poly[2-methoxy-5-(3',7'-dimethyloctyloxy)-1,4-phenylene vinylene] (MDMO-PPV) films<sup>14</sup> were prepared by spin coating a 0.7 wt% toluene solution onto an indium tin oxide (ITO) coated glass substrate as described in ref 12. The film thickness is typically 170 nm as measured by an alpha stepper. By means of a transfer chamber samples were transported to a UHV chamber for Cs and Al deposition without being exposed to air. Cs was deposited by evaporation from an alkali metal dispenser purchased from Saesgetters at about 750 °C. The LED structures (6 in each run) were completed by vapor deposition of an 80 nm Al capping layer. The active area for each LED structure amounts 24 mm<sup>2</sup>.  $I$ - $V$  characterization, electroluminescence (EL) and admittance spectroscopy were all conducted in situ in the glovebox at a temperature of 20 °C. Admittance spectroscopy in the range of 5 Hz – 1 MHz was performed with a Hewlett Packard 4192A impedance analyzer. A small alternating signal,  $v_{ac}$ , of 50 mV was superimposed onto a dc bias,  $v_{dc}$ , up to 10 Volt. Measurements at different modulation levels, ( $v_{ac} = 10 - 250$  mV) showed identical results. The results were obtained in five runs at different Cs coverage, which were all repeated once. The, yet extensive, discussion in this paper is restricted to two deposition coverages. The results of the other coverages are entirely consistent with the ones discussed here.

### 3.3 Results

#### 3.3.1 Al / MDMO-PPV / ITO

In an admittance experiment the charge relaxation driven by a small harmonic voltage modulation  $v_{ac}$  is probed. Both amplitude and phase difference of the ac current  $i_{ac}$  are monitored as a function of frequency,  $f$ , to obtain the complex admittance  $Y$ :

$$Y(\omega) = i_{ac} / v_{ac} = G(\omega) + i \omega C(\omega) \quad [1]$$

with  $G$  conductance,  $C$  capacitance,  $i = \sqrt{-1}$ , and  $\omega = 2 \pi f$  the angular frequency.

Figure 1 gives the capacitance and conductance as a function of frequency at room temperature measured on an Al / MDMO-PPV / ITO structure at different forward bias. At  $v_{dc} = 0$  V the response to the alternating field is shown in both the conductance and capacitance spectra and is modeled by a contact resistance that we attribute to the ITO (fig 2).

At  $v_{dc} = 2$  V, the built-in potential is exceeded and hole transport into the polymer film occurs. As the intrinsic charge carrier density in the film is negligible compared to the injected charge, the field is entirely determined by the positive space charge density that has accumulated inside the device. Current limitation by non-ohmic behavior of the ITO / MDMO-PPV hole contact may be disregarded in this bias domain, as was demonstrated by Blom *et al*<sup>15</sup>. Modeling of  $I$ - $V$  curves and impedance spectra of numerous devices confirmed this notion, see also below. Note, however, that the electron contact still is non-ohmic. In order to understand the admittance spectra one can imagine that the superposition of the harmonically alternating field now results in space charge waves that redistribute to compensate for these oscillations. When the oscillation period is much longer than the carrier transit time,  $\tau_{tr}$ , i.e. the time the carrier needs to travel from one electrode to the other, the capacitance experiences a negative (or inductive) contribution as a result of this charge relaxation, resulting in a low frequency capacitance that is 3/4 of its geometrical value (fig 3a). At periods much shorter than  $\tau_{tr}$  the negative contribution disappears and the original dielectric response is recovered. The same applies for the conductance: as the charges cannot keep up with the alternating field  $\omega > 1/\tau_{tr}$  the conductance decreases (fig 3b) and the dielectric response takes over. This crossover in admittance spectroscopy is called the transit time effect and is described by small signal theory for space charge limited (SCL) diodes<sup>16</sup>:

$$Y(\omega) = \frac{\varepsilon A}{2L} \frac{\vartheta^3}{\tau_{tr}} \left[ \frac{\vartheta - \sin \vartheta}{(\vartheta - \sin \vartheta)^2 + (1 - \cos \vartheta - \vartheta^2 / 2)^2} - i \frac{1 - \cos \vartheta - \vartheta^2 / 2}{(\vartheta - \sin \vartheta)^2 + (1 - \cos \vartheta - \vartheta^2 / 2)^2} \right] \quad [2]$$

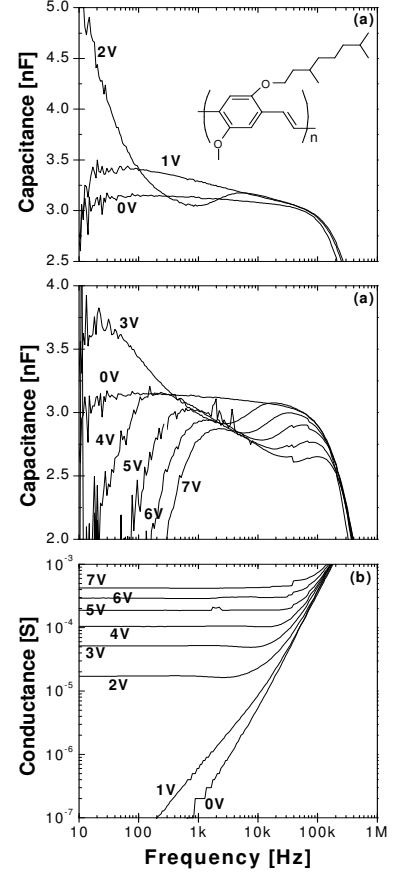


**Figure 1:** (a) Capacitance and (b) conductance versus frequency measured at an Al / MDMO-PPV / ITO structure for different forward bias,  $v_{dc}$ , which are indicated in the figure. Inset gives the chemical structure of MDMO-PPV.

$A$ ,  $L$  and  $\tau_{tr}$  are the film surface area, thickness and hole transit time, respectively. Here  $\vartheta$  is the charge carrier transit angle and equals  $\omega \tau_{tr}$ . This classical description is derived from Poisson's law and the continuity equation assuming an Ohmic injecting contact and a field independent mobility. The transit time effect is clearly observed in the conductance and capacitance spectra in fig 3 and can be used to determine the hole mobility as a function of bias:<sup>16</sup>

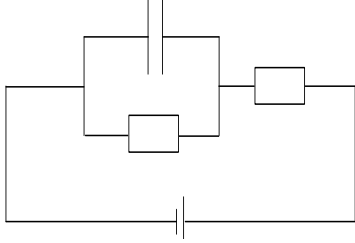


**Figure 2:** Schematic representation of a contact resistance in series with a capacitance with small leakage current.

$$\tau_{tr} = \frac{4}{3} \frac{L^2}{(V - V_{bi})\mu_h} \quad [3]$$

The oscillations for  $\omega \tau_{tr} \geq 10$  predicted by eq. 2 are not observed due to the non-negligible dielectric response at these frequencies that results in a divergence of space charge<sup>17</sup>. At frequencies lower than the reciprocal transit time the observed capacitance significantly deviates from its calculated behavior. This extra contribution to the capacitance has recently been ascribed to dispersive transport due to hopping in a disordered molecular solid<sup>4,13</sup>. Martens *et al*<sup>4</sup> argued that these hopping events result in both a distribution of transit times as well as a frequency

dependent mobility. However, as the mobility is directly linked to the transit time via eq. 3, it seems meaningless to apply separate distribution functions. Moreover, the frequency dependence of the mobility,  $\mu(\vartheta) = 1 + M(i\vartheta)^{1-\alpha}$ , with  $0 < \alpha < 1$  and  $M$  a constant applies only for frequencies higher than the reciprocal transit time, according to ref 18. When characterizing Schottky contacts by admittance spectroscopy, excess capacitances, which exhibit similar frequency behavior as observed in our experiments, are usually interpreted in terms of charge relaxation in trap levels<sup>19</sup>. The excess capacitance is thus explained by traps that become charged. When approaching the trap emission rate by increasing  $f$ , charge transfer from the trap starts to lag behind the driving voltage and the out-of-phase component (the excess capacitance) decays, while simultaneously the in-phase component,  $G(\omega)$ , increases<sup>19</sup>. The theory describing the trapping process in space charge limited diodes by a single trapping level was derived by Dascalu<sup>20</sup> and later by Kassing<sup>21</sup>. The equation describing the capture and emission of the charge carrier by a single trap can be linearized and results in both a steady state and a frequency dependent trapping parameter  $\theta$  and  $\alpha(\omega)$ , respectively, which are given by

$$\begin{aligned} n_{dc} + n_{dc,T} &= \theta^{-1} n_{dc} \\ n_{ac} + n_{ac,T} &= \alpha(\omega) n_{ac} \\ \alpha(\omega) &= 1 + \frac{\omega_v}{i\omega + \omega_e} \end{aligned} \quad [4]$$

Here, the subscripts dc, ac and T refer to the steady state, time dependent and trapped values for the charge density.  $\omega_v$  is the reciprocal of the charge lifetime  $\tau_v$  in the transport (= valence) band and  $\omega_e$  the reciprocal lifetime in the trap level  $\tau_e$ . The expression for the admittance expressed in these parameters becomes<sup>21</sup>

$$Y(\omega) = \frac{\varepsilon A}{2L} \frac{1}{\alpha \tau_{tr}} \left\{ \sum_{k=0}^{\infty} \frac{\Gamma(\theta\alpha + 1)}{\Gamma(\theta\alpha + k + 2)} \frac{(-i\omega\tau_{tr})^k}{(k+3)} \right\}^{-1} \quad [5]$$

$\Gamma$  is the Euler-Gamma function and the frequency dependence of  $\alpha$  according to eq. 4 is implied. It is easy to show that this expression converges to the original equation for the admittance in the limit ( $\theta \rightarrow 1$ ,  $\alpha \rightarrow 1$ ). The gradient in *both* conductance and capacitance can now be fitted with reasonable values for  $\tau_e = 5.0 \times 10^{-3}$  s and  $\tau_v = 1.7 \times 10^{-1}$  s and agrees qualitatively with the data, see fig. 3. Note that  $1/\tau_e > 1/\tau_v$ , which is a characteristic of shallow traps. The measured excess capacitance (on top of the geometrical capacitance) in fig 3 manifests itself in the whole frequency range up to  $1/\tau_{tr}$ . This leads to the conclusion that more than one trapping level is present. The description of the capacitance can be made to match the data exactly by inclusion of more than one trapping level. However, the conductance is already accurately modeled by only one trap for which  $\tau_e \ll \tau_v$ . Note that in the interpretation of Martens *et al.*,<sup>4</sup> this low frequency gradient in the conductance was not included.

The agreement with the data is hardly dependent on the exact value of  $\theta$ . A variation of  $\theta$  from 1 to  $10^{-5}$  can be compensated by a change in transit time of only a factor  $\sim 2$ , which is within the experimental error. The admittance spectra of Al / MDMO-PPV / ITO structures thus allow us to simultaneously determine the hole transit time and the trap relaxation as both phenomena are well separated in the frequency domain.

At  $v_{dc} = 4$  V a negative contribution to the capacitance sets in, which at higher bias even becomes inductive. This effect has been observed on a range of materials before and is well known to result from minority carrier injection<sup>22</sup>. At high forward bias both charge carriers are injected. At frequencies much lower than the reciprocal dielectric relaxation time but higher than the electron response, the hole density will redistribute to compensate the field modulation. The conductance measured at these frequencies will be entirely due to the hole current density, though possibly suffering from trapping processes. At lower frequencies the electron response sets in and a delayed (= inductive) increase in conductance follows (note the decrease  $C$  in fig. 1).

The frequency at which the capacitance becomes inductive has been explained either in terms of an injection barrier<sup>23</sup> or transit time<sup>24</sup> for the minority carrier. However, as trap relaxation was not taken into account in these references, the actually determined value for the latter parameter becomes arbitrary.

By fitting the conductance spectra to eq. 5 we obtain the transit time and determine the hole mobility as a function of bias from eq. 3, see fig. 4. Here, we neglected the electron contribution to the conductance. The hole mobility clearly exhibits the field dependence typically observed in disordered molecular materials, which follows the Poole-Frenkel law:

$$\mu_h = \mu_0 \exp(\gamma\sqrt{E}) \quad [6]$$

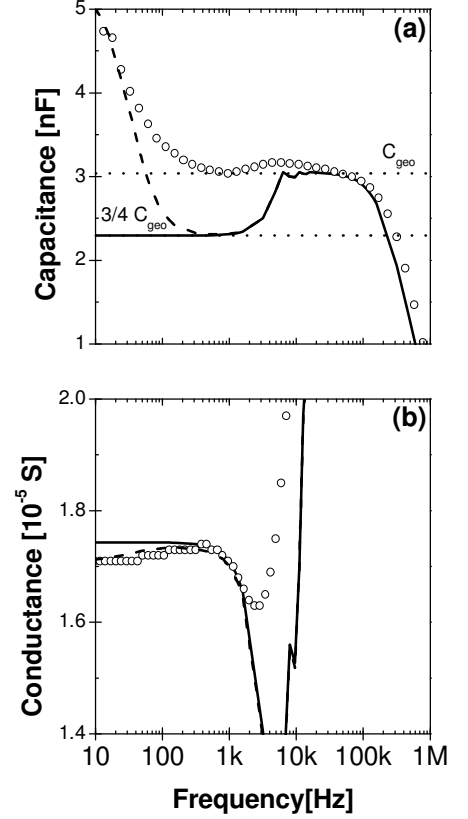


**Figure 3:** (a) Capacitance and (b) conductance at  $v_{dc} = 2$  V (open symbols). The solid line represents the frequency dependent SCLC model as calculated in eq. 2, which gives the hole transit time  $\tau_{tr} = 2.15 \times 10^{-4}$  s. The dashed line includes trap relaxation by a single trap level (eq. 5). The hole lifetime in the valence band and in the trap level are  $\tau_v = 1.7 \times 10^{-1}$  s;  $\tau_e = 5.0 \times 10^{-3}$  s respectively.



Here  $\mu_0 = 7 \times 10^{-11} \text{ m}^2/\text{V s}$  and  $\gamma = 4.1 \times 10^{-4} (\text{V/m})^{1/2}$ , which is in good agreement with literature<sup>25</sup>. The origin of this Poole-Frenkel behavior is still under debate and various models have been proposed, either assuming energetic disorder due to localized states<sup>26</sup> or structural disorder resulting in stochastic transport<sup>4,5,13</sup>. Note, however, that interpretation of the measured excess capacitance in terms of stochastic transport<sup>4,13</sup> seems ambiguous. The identification of (localized) trap states in the admittance spectra implies that energetic disorder cannot be ignored in the description of the carrier

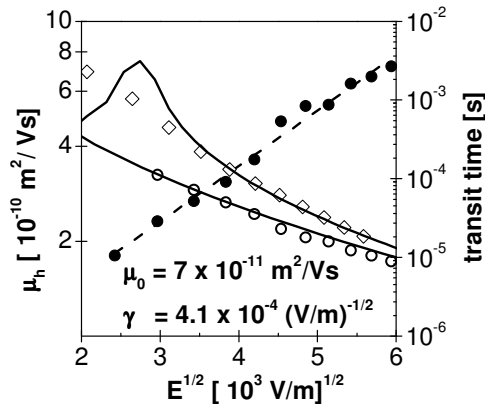


**Figure 4:** Mobility (filled circles) determined as a function of bias from the transit time effect. The Poole-Frenkel behaviour  $\mu_h = \mu_0 \cdot \exp(\gamma\sqrt{E})$  is clearly observed. The field independent mobility  $\mu_0 = 7 \times 10^{-11} \text{ m}^2/\text{Vs}$  and the Poole-Frenkel factor  $\gamma = 4.1 \times 10^{-4} (\text{V/m})^{1/2}$  are determined from a fit to the data points (dashed line). Open circles represent the transit times as obtained from admittance spectroscopy at an Al / MDMO-PPV / ITO stacking structure and the solid line is the transit time calculated with the steady state conductivity model. Also included are the transit times obtained from the structure with deposited Cs ( $4.8 \times 10^{13} \text{ atoms/cm}^2$ ; open diamonds). The Cs diffusion profile is included in the model as an electron donor level of 0.61 eV below the LUMO level, which was derived from the fit to the measured current density. The agreement is well within the error rate.

transport. Similar conclusions were obtained from experiments performed on (unsubstituted) PPV. Here, the Poole-Frenkel behavior was ascribed to field dependent release times from localized states<sup>3</sup>. From thermally stimulated current (TSC) experiments Meier *et al*, identified two levels at 0.03 and 0.18 eV above the valence band, and suggested that the ITO anode could account for this, as these levels were absent in case an Au anode was applied<sup>26</sup>.

The field dependence of the mobility is not explicitly taken into account in the derivation of eq. 2 and 5 and one can argue that the field dependent mobility in fig 4 is determined in an inconsistent manner. In order to estimate the error made, the hole transit times are compared to ones obtained from a self consistent steady state conductivity model in which the Poole-Frenkel behavior is included. This model will be outlined below. Fig 4 demonstrates that these calculated transit times and the ones determined from the admittance spectra are in good agreement and hence the inconsistency in the determination for the mobility is of negligible importance.

The steady-state model is based on the model presented in refs. 27 and 28. It treats charge injection and bulk transport on equal level, which implies that no *a priori* assumptions about the dominance of either process need to be made. The bulk transport is described by the well-known drift equation  $j = n_{dc} q \mu(E) E$  where all parameters but  $q$  may depend on the position  $z$  between the electrodes and  $\mu(E)$  is given by eq. 6. Carrier injection is described in terms of hopping injection into a Gaussian distribution of transport sites<sup>29</sup>. The field distribution  $E(z)$  is obtained by simultaneously solving the Poisson equation. Apart from the charge density due to the mobile electrons and/or holes, charge density may also result from the presence of doping or trapping states. The local degree of dopant ionization follows immediately from the position of the (local) hole or electron quasi Fermi level. The latter is obtained from the relation

$$n_{dc}(z) = \int_{-\infty}^{\infty} dE g(E) f(E - E_F) \quad [7]$$

with  $g(E) = g_0(2\pi\sigma^2)^{-1/2} \exp\left(-\frac{E^2}{2\sigma^2}\right)$  the Gaussian density of states with width  $\sigma$  and  $f(E-E_F)$  the

Fermi distribution function that is approximated by a step function. In Eq. 7, the center of the LUMO level is taken as zero energy. A similar expression holds for holes, with  $E$  replaced by  $E-E_g$  in which  $E_g$  is the (single-particle) bandgap of the organic semiconductor. The occupation  $\theta$  of a shallow trap level under a Gaussian transport level is given by

$$\theta = \frac{N}{N_T} \exp\left[\frac{1}{2}\left(\frac{\sigma}{kT}\right)^2 - \frac{|E_{tr} - E_T|}{kT}\right] \quad [8]$$

where  $\sigma$  equals 0.12 eV for MDMO-PPV<sup>30</sup>.  $N$  and  $N_T$  are the number of transport and trap sites respectively and  $E_{tr}-E_T$  is the energy of the trap level.

We use  $\mu_0$  and  $\gamma$  derived from the admittance experiments measured at the Al / MDMO-PPV / ITO structure, and the only unknown parameter, the built-in potential, is determined to be 1.2 V by optimizing the correspondence to the measured current density (fig. 5). The model reduces to space charge limited behavior when the injection barrier is set below 0.3 eV<sup>31</sup>. Notice that the steady state

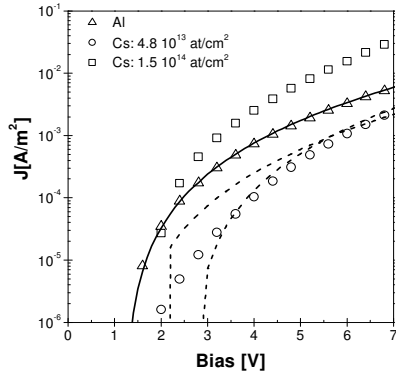


**Figure 5:** Current density-voltage characteristics at various Cs deposition coverages:  $4.8 \times 10^{13}$  (circle) and  $1.5 \times 10^{14}$  (square) atoms/cm<sup>2</sup> and without Cs (triangle). For the latter structure the conductivity (solid line) is accurately described by the steady state model. At a Cs coverage of  $4.8 \times 10^{13}$  atoms/cm<sup>2</sup> we calculated the effect of a hole trapping level (upper dashed line) or an electron donor level (lower dashed line).

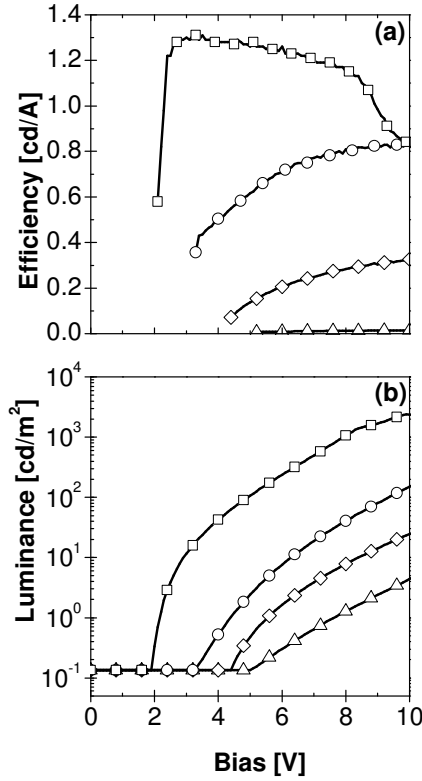


**Figure 6:** (a) Efficiency and (b) electroluminescence (EL) versus bias on Al / Cs / MDMO-PPV / ITO structures with varying Cs deposition coverage:  $4.2 \times 10^{13}$  (diamond),  $4.8 \times 10^{13}$  (circle) and  $1.5 \times 10^{14}$  (square) atoms/cm<sup>2</sup> and without Cs (triangle).

conductivity can be accurately described without including a trapping level. This indicates that the trap density is either very low or indeed shallow, as was determined by the admittance spectra. The reproducibility in hole mobility (about a factor 2 in this bias range) is mainly determined by the variation in polymer layer thickness.

### 3.3.2 Al/ Cs/ MDMO-PPV/ ITO

The effect of Cs deposition on the electroluminescence is demonstrated in fig. 6. The luminescence is continuously enhanced with Cs coverage starting from  $5 \text{ cd/m}^2$  up to  $2500 \text{ cd/m}^2$  at 10 V bias and its onset is reduced from 5 V to about 2 V. The current density as a function of bias initially decreases with Cs deposition. At higher coverage the current density increases again (fig 5). The current onset shifts from 1.0 to 1.4 V. The efficiency, (fig 6) starting at a maximum value of 0.01 cd/A converges to a value of 1.3 cd/A and cannot not be altered upon further deposition. The energy resolved electroluminescence spectra of these structures show a shift of the spectral maximum towards lower energies (red shift) as a function of deposition (fig 7). This suggest that recombination occurs close at the interface where Cs is deposited and the electronic structure is altered, which is anticipated when modifying the conduction from hole dominated to double injection.

Ion scattering spectrometry clearly demonstrates the diffusion of Cs atoms up to  $150 \text{ \AA}$  into the polymer layer as illustrated in fig. 8. For the experimental details and a description of the used

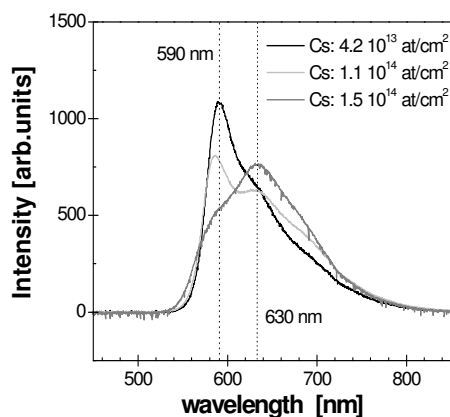


**Figure 7:** *Electroluminescence spectrum as a function of Cs deposition.*

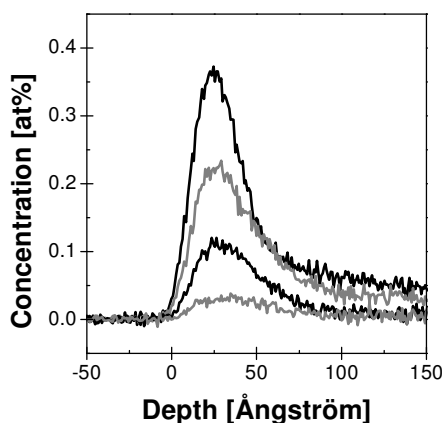


**Figure 8:** *Cs diffusion profiles obtained by NICISS. The total deposition is calculated by integration of the spectra and amounts (from top to bottom) to  $1.5 \times 10^{14}$ ,  $1.1 \times 10^{14}$ ,  $4.8 \times 10^{13}$  and  $1.7 \times 10^{13}$  atoms/cm<sup>2</sup>.*

technique we refer to ref 12 in which similar results were obtained for the deposition of K onto MDMO-PPV. Cs was not detected at the polymer surface, indicating complete diffusion into the polymer. Integration of these spectra yields the total deposited amount as given in the caption to fig. 8.

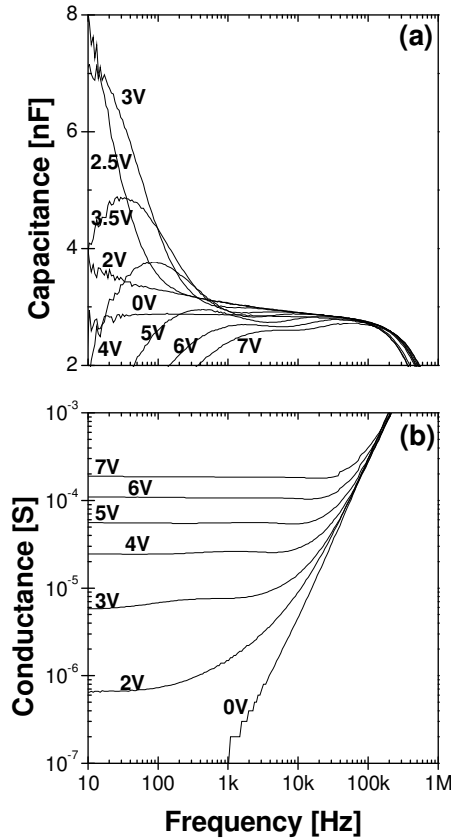


**Figure 9:** (a) Capacitance and (b) conductance versus frequency on an Al / Cs / MDMO-PPV / ITO structure for different forward bias, which are indicated in the figure. Cs deposition coverage is  $4.8 \times 10^{13}$  atoms/cm<sup>2</sup>.

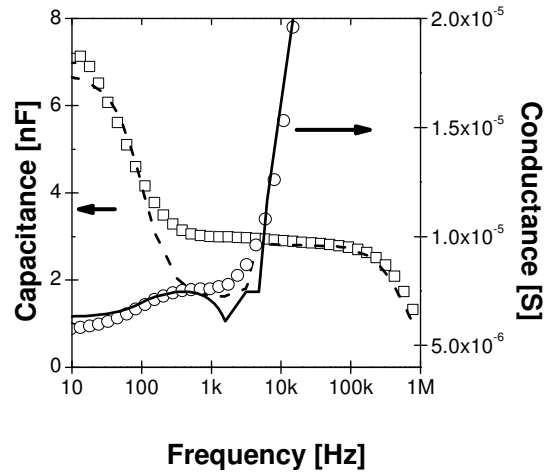


**Figure 10:** Conductance and capacitance versus frequency on an Al / Cs / MDMO-PPV / ITO structure with deposition coverage  $4.8 \times 10^{13}$  atoms/cm<sup>2</sup> at 3 V bias (open symbols). Also shown are the real and imaginary parts of eq 5 ( $\tau_r = 2.24 \times 10^{-4}$  s,  $\theta = 10^{-5}$ ,  $\tau_v = 9.0 \times 10^{-3}$  s and  $\tau_e = 1.9 \times 10^{-3}$  s)

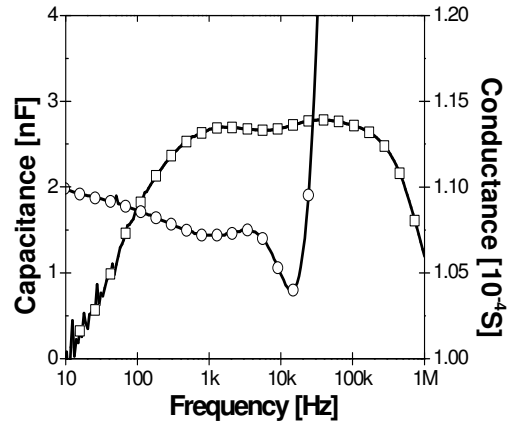


**Figure 11:** Conductance (circles) and capacitance (squares) versus frequency on an Al / Cs / MDMO-PPV / ITO structure with deposition coverage  $4.8 \times 10^{13}$  atoms/cm<sup>2</sup> at 6 V bias

The admittance measurements performed on the structure with a Cs coverage of  $4.8 \times 10^{13}$  atoms/cm<sup>2</sup> demonstrate a decreased hole conductance, in correspondence with the *I-V* characterization (compare fig 1 and 9). Both the excess capacitance and the gradient in conductance become more pronounced compared to the spectra without Cs. This is mostly reflected in the hole lifetime in the valence band which is an order of magnitude smaller than for the Al / MDMO-PPV / ITO structure. This will be addressed in the discussion. The crossover (solid line in fig 3) due to the transit time effect is obscured in the admittance spectra at low bias due to this trap relaxation (fig. 10). At higher bias the transit time effect reappears and the conduction spectra demonstrate an increase in the hole transit time compared to the Al / MDMO-PPV / ITO structures. The corresponding lifetimes in the valence and trap level for this Al / Cs / MDMO-PPV / ITO structure at 3 V bias are  $\tau_v = 9.0 \times 10^{-3}$  s and  $\tau_e = 1.9 \times 10^{-3}$  s (fig. 10) and the hole transit time as a function of bias is plotted in fig. 4.

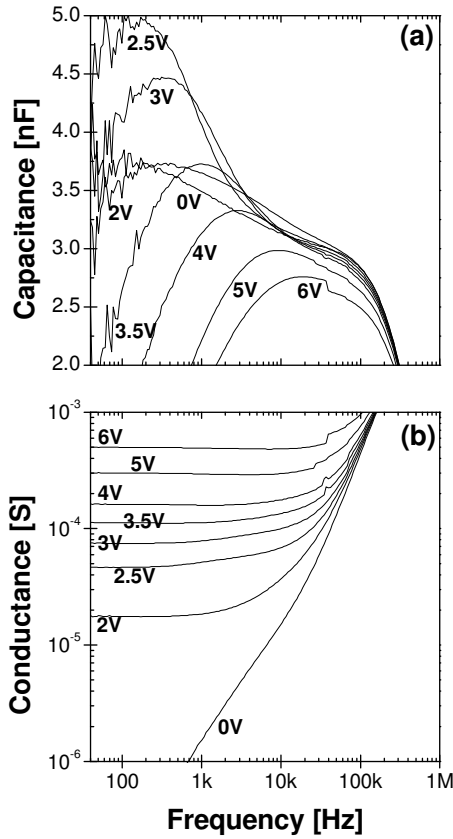


**Figure 12:** (a) Capacitance and (b) conductance versus frequency on an Al / Cs / MDMO-PPV / ITO structure for different forward bias. Cs deposition coverage is  $1.5 \times 10^{14}$  atoms/cm<sup>2</sup>.

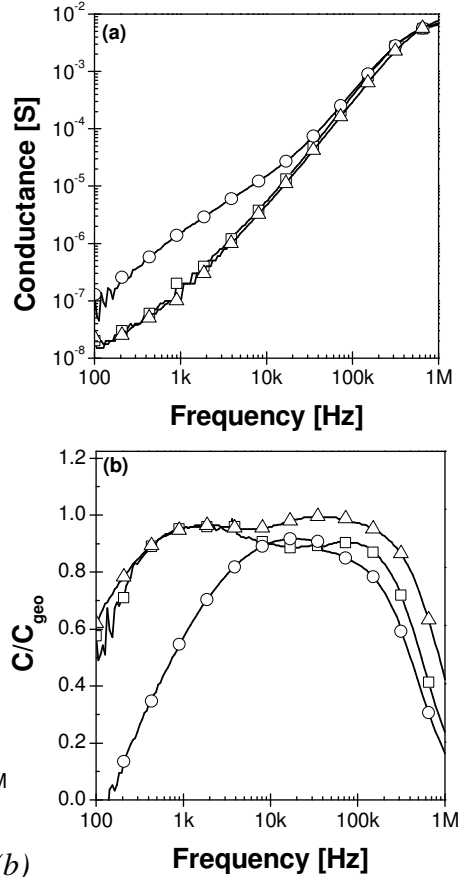


**Figure 13:** (a) conductance at zero bias for an Al / MDMO-PPV / ITO structure (squares) and for the Al / Cs / MDMO-PPV / ITO structures with  $4.8 \times 10^{13}$  (triangles) and  $1.5 \times 10^{14}$  at/cm<sup>2</sup> (circles) Cs deposition coverage. (b) normalized capacitance  $C/C_{geo}$  measured at 6 V bias for these structures, where  $C_{geo}$  represents the geometrical capacitance.

At 6 V the minority carrier features in the admittance spectra are clearly visible (up to 1 kHz the capacitance increases while the conductance decreases) and resemble the behavior without Cs, though the absolute value for the (hole dominated) conductance in this frequency domain is much lower, see figure 11.

At  $1.5 \times 10^{14}$  atoms/cm<sup>2</sup> coverage and zero bias we observe an increased conductance (fig 13a) and a capacitive contribution up to  $2 \times 10^4$  Hz (fig. 12a). In the whole bias range, i.e. up to 7 V, the transit time crossover for holes can no longer be identified in the conduction spectra. Hence, we conclude that this space charge effect is completely perturbed by the presence of either hole trapping levels or electron transport. We observe that the inductive contribution to the capacitance shifts towards higher frequencies ( $\sim 10^4$  Hz at 6 V), which indicates an enhanced electron transport.

### 3.4 Discussion

Photoelectron spectroscopy (PES) and electron energy loss spectroscopy (EELS) studies have demonstrated the charge transfer and the subsequent formation of gap states upon deposition of alkali and alkaline earth metals onto  $\pi$ -conjugated systems<sup>7-11</sup>. These states have been identified as polaron and bipolaron states (see inset of fig. 14). The lower state above the highest occupied molecular orbital (HOMO) is doubly occupied while the upper state below the lowest unoccupied molecular orbital (LUMO) is singly (doubly) occupied in case of a (bi)polaron. Below, these PES results are employed to interpret our admittance experiments. The Cs concentrations are below one monolayer coverage and consequently it seems reasonable to assume that complete charge transfer has occurred.

The decreased current density at  $4.8 \times 10^{13}$  atoms/cm<sup>2</sup> coverage, and consequently also the increased hole transit time may either originate from Coulomb scattering, trapping or doping at the polymer cathode interface. Of these possibilities Coulomb scattering may be neglected as, even in the vicinity of the Al layer, the mean free path of approximately 3 nm is much smaller than the inter-alkali-atom distance. Charging of either electron donors or hole trapping states will lead to additional band bending and hence cause a significant fraction of the potential difference to drop in the interface layer. In this case a change in transit time does therefore not necessarily imply a change in mobility, but rather a change in field distribution in the device. In order to quantify this proposition we extended the model to calculate the steady state conductivity by taking into account the measured Cs profile as a distribution of either electron donors or hole traps. By only adjusting the energy of the trapping/doping level, good agreement with the measured steady state conductivity is obtained. These doping/trapping levels are approximated to be independent of concentration, as we assume no interaction among the Cs sites at such low coverage. The results are depicted as dashed lines in figure 5. We observe a reduced (hole dominated) current density in both cases. The inclusion of a trapping level, however, exhibits a reduced current density only at high bias, which can be understood from the fact that charging of the traps may only occur *after* hole injection sets in. In contrast, doping states are immediately charged upon deposition: donated electrons will minimize their energy by diffusing to the Al electrode, creating a positively charged background. Consequently, the current density will be reduced over the whole bias range. Apart from the region directly at the current onset, a donor level at 0.61 eV below the LUMO level gives the best agreement with the measured current density. Hence we tentatively attribute the field modification at the MDMO-PPV / Al interface (fig 14) to a Cs induced electron donor level, which then accounts for the observed increase in hole transit time. The increased hole transit times observed in the admittance spectra, shown in fig 4, compare favorably with the ones calculated using this steady state model.

The increased conductance and capacitance at zero bias observed at  $1.5 \times 10^{14}$  atoms/cm<sup>2</sup> coverage (fig. 13) confirm the identification of Cs induced donor states. Upon deposition the Fermi level in the originally intrinsic layer moves from the gap into these states. Electrons then redistribute by tunneling or diffusion in the (possibly Cs induced) gap states to compensate for the oscillating field. This redistribution explains the higher capacitance as the total dipole moment increases due to the mobile electrons. When the frequency is increased, the average distance electrons can travel is reduced and hence the contribution from this enhanced dipole moment disappears. When  $\omega \sim 1/\tau_e$  the trapped charge carriers cannot follow the harmonic oscillations and the out-of-phase component partly changes into an in-phase contribution<sup>19</sup>. This is observed in the conductance spectrum for the whole frequency range up to  $2 \times 10^4$  Hz. Cs inducing only a neutral hole trapping level (at zero Volt) cannot account for these features in the admittance spectra, as the hole capture and emission rate cannot be probed below the onset of hole injection. The inductive contribution to the capacitance at 6 V is maintained up to higher frequencies as compared to

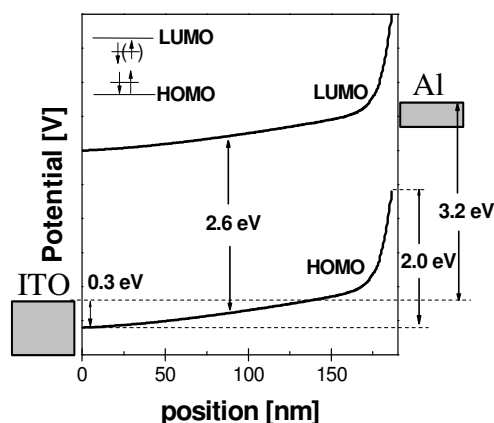


**Figure 14:** Calculated potential distribution through the polymer layer (186 nm) at 3.2 V bias with a donor concentration corresponding to the diffusion profile obtained for the  $4.8 \times 10^{13}$  atoms/cm<sup>2</sup> Cs deposition and an energy level of 0.61 eV below the LUMO. The left side corresponds with the ITO contact. The inset schematically pictures the (bi)polaron level in the band gap.

increasing number of trap states or from the increased field at the Cs doped interface, which remains a subject for further investigations.

Admittance spectroscopy thus successfully demonstrates an increased hole transit time and an enhanced electron transport with Cs deposition, which is confirmed by steady state conductivity measurements and modeling. The improved charge balance is reflected in the enhanced electroluminescence for Al/Cs/MDMO-PPV/ITO structures. Moreover, exciton dissociation by the metal induced gap states as observed by Park *et al.*,<sup>32</sup> apparently is of secondary importance and it is concluded that Cs *diffusion* is in fact favorable for current balancing and hence electroluminescence.

The excess capacitance and the conductance are analytically described *simultaneously* by taking into account the (majority carrier) transit time effect combined with a single trap level. This interpretation differs from recently published literature<sup>4, 13</sup>. The explanation of the excess capacitance by introducing an extra set of parameters that take into account the spread in hole transit times as well as an frequency dependent mobility, seems unnecessary and can in fact be ruled out by the arguments given in former sections. It is also demonstrated that deriving directly the electron mobility from the spectra<sup>24</sup> seems ambiguous.

The phenomenological dependence of excess capacitance on minority carrier injection was first demonstrated by Werner *et al.*<sup>33</sup> It is confirmed that the capacitance is highly dependent on fabrication of the minority carrier injection contact. However, we describe the excess capacitance by the lifetimes of the hole transport and trap level. Minority carrier injection in principle leads to recombination, which was not observed below 4 V bias for devices without Cs deposition. In fact, excess capacitances were also demonstrated in single carrier devices for either hole transport<sup>4</sup> as well as electron transport<sup>13</sup>. It remains to be determined how these lifetimes are affected by minority carrier injection.

samples with lower Cs coverage, which is indicative for an enhanced electron transport. This confirms the enhanced field at the interface, which indeed should result in an increased electron injection and/or higher electron mobility (fig. 14). This interpretation is in good correspondence with the observed increase in the steady state conductivity for these LED structures.

The excess capacitance at low bias that is described by the charge relaxation in a trap level, is clearly affected by Cs doping. We observe an increased excess capacitance, which is reflected in a reduced value for the hole lifetime in the valence band. The observed ratio  $\omega_h/\omega_e < 1$  for moderate Cs doping indicates that shallow traps dominate the conduction spectra. This is not contradicting the steady state calculations, from which we claimed to observe the effect of a Cs induced donor level. The conductivity at  $4.8 \times 10^{13}$  atoms/cm<sup>2</sup> remains hole dominated and hence *dispersion* in the admittance spectra at 2-3 V bias can only be expected from hole relaxation in trap levels. However, the *decline* in the steady state current density due to field modification in the polymer layer is attributed to an electron donating level. The enhanced trapping features in the admittance spectra as a result of Cs deposition can be understood from either an

### **3.5 Conclusion**

Quantitative agreement is found between admittance experiments and the analytical description of the frequency dependent space charge limited transport taking into account trap relaxation in Al/ MDMO-PPV/ ITO devices. It is also shown that the field independent mobility approximation in this model is applicable within the experimental limitations and this technique can thus be applied to directly determine carrier mobilities in the SCLC regime, even in the presence of trap levels.

From the electronic transport characterization we can directly distinguish between two processes that result in an enhanced electroluminescence with Cs deposition in the sub-monolayer regime. We identify an increase in the hole transit time at a doping concentration of  $4.8 \times 10^{13}$  atoms/cm<sup>2</sup> and additionally an improved electron injection. The latter was concluded from a shift of the inductive contribution towards higher frequency at concentrations  $\approx 1.5 \cdot 10^{14}$  atoms/cm<sup>2</sup>. We attribute both phenomena to a potential drop near the cathode interface as a result of chemical doping by the alkali species. A steady state model including doping was developed to calculate the current density as an explicit function of the two charge densities and mobilities at each position in the polymer layer. Good agreement with both the hole transit times derived from admittance spectroscopy and the I-V characterization was obtained.

This proves that the condition for the alignment of energy levels between the LUMO and metal work function for electron injection may be relaxed by doping of the polymer surface layer, for which sub-monolayer concentrations already suffice. In principle, even noble metals, which are less sensitive to oxygen and water in the atmosphere, can act as electron injection contact.



### 3.6 References and notes

- [1] J.H. Burroughes, D.D.C. Bradley, A.R. Brown, R.N. Marks, K. Mackay, R.H. Friend, P.L. Burn, A.B. Holmes, *Nature* **347**, 539 (1990).
- [2] S.H. Kim, T. Zyung, H.Y. Chu, L.-M. Do, D.-H. Hwang, *Phys. Rev. B* **61**, 15854 (2000).
- [3] G. Juška, K. Arlauskas, M. Viliūnas, K. Genevičius, R. Österbacka, H. Stubb, *Phys. Rev. B* **62**, R16235 (2000).
- [4] H.C.F. Martens, H.B. Brom, P.W.M. Blom, *Phys. Rev. B* **60**, R8489 (1999).
- [5] P.W.M. Blom, M.C.J.M. Vissenberg, *Phys. Rev. Lett.* **80**, 3819 (1998).
- [6] H. Meyer, D. Haarer, H. Naarmann, H.H. Hörhold, *Phys. Rev. B* **52**, 2587 (1995).
- [7] E. Ettegui, H. Razafitrimo, Y. Gao, B.R. Hsieh, W.A. Field, M.W. Ruckman, *Phys. Rev. Lett.* **76**, 299 (1996).
- [8] D. Steinmüller, M.G. Ramsey, F.P. Netzer, *Phys. Rev. B* **47**, 13323 (1993).
- [9] M. Fahlman, D. Beljonne, M. Lögdlund, R.H. Friend, A.B. Holmes, J.L. Brédas, W.R. Salaneck, *Chem Phys. Lett.* **214**, 327 (1993).
- [10] G. Iucci, K. Xing, M. Lögdlund, M. Fahlman, W.R. Salaneck, *Chem. Phys. Lett.* **244**, 139 (1995).
- [11] J. Birgerson, M. Fahlman, P. Bröms, W.R. Salaneck, *Synth. Met.* **80**, 125 (1996).
- [12] H.H.P. Gommans, A.W. Denier van der Gon, G.G. Andersson, L.J. van IJzendoorn, R.M.T. Pijper, H.H. Brongersma, *J. Appl. Phys.* **94**, 5756 (2003).
- [13] S. Berleb, W. Brütting, *Phys. Rev. Lett.* **89**, 286601-1 (2002).
- [14] D. Braun, E.G.J. Staring, R.C.J.E. Demandt, G.L.J. Rikken, Y.A.R.R. Kessener, A.H.J. Venhuizen, *Synth. Met.* **66**, 75 (1994).
- [15] P.W.M. Blom, M.J.M. de Jong, J.J.M. Vleggaar, *Appl. Phys. Lett.* **68**, 3308 (1996).
- [16] J. Shao, G.T. Wright, *Sol. Stat. Elec.* **3**, 291 (1969).
- [17] R. Heidemann, D. Jäger, R. Kassing, *Phys. Stat. Sol.(a)* **44**, 191 (1977).
- [18] H. Böttger, V.V. Bryksin, *Hopping Conduction in Solids*, Akademie-Verlag, Berlin, 1985.
- [19] P. Blood, J.W. Orton, *The Electrical Characterization of Semiconductors: Majority Carriers and Electron States*, Academic Press, San Diego, 1992.
- [20] D. Dascalu, *Int. J. Electron* **21**, 183 (1966).

- [21] R Kassing, Phys. Stat. Sol. (a) **28**, 170 (1975).
- [22] M. Ershov, H.C. Liu, L. Li, M. Buchanan, Z.R. Wasilewski, A.K. Jonscher, IEEE Trans. Elec. Dev. **45**, 2196 (1998). This article gives an extensive reference overview.
- [23] F. Lemmi N.M. Johnson, Appl. Phys. Lett. **74**, 251, (1999).
- [24] H.C.F. Martens, J.N. Huiberts, P.W.M. Blom, Appl. Phys. Lett. **77**, 1852 (2000).
- [25] P.W.M. Blom, M.J.M. de Jong, IEEE J. of Sel. Top. In Quant. Elec. **4**, 105 (1998).
- [26] H. Bässler, Phys. Stat. Sol. **B 175**, 15 (1993). D.H. Dunlap, P.E. Paris, V.M. Krenke, Phys. Rev. Lett. **77**, 542 (1996). S.V. Novikov, D.H. Dunlap, V.M. Krenke, P.E. Paris, A.V. Vannikov, Phys. Rev. Lett. **81**, 4472 (1998).
- [26] M. Meier, S. Karg, K. Zuleeg, W. Brütting, M. Schwoerer, J. Appl. Phys. **84**, 87 (1998).
- [27] M. Kemerink, P. Offermans, P.M. Koenraad, J.K.J. van Duren, R.A.J. Janssen, H.W.M. Salemink, J.H. Wolter, Phys. Rev. Lett. **88**, 2404 (2002).
- [28] M. Kemerink, S.F. Alvarado, P. Müller, P.M. Koenraad, H.W.M. Salemink, J.H. Wolter, R.A.J. Janssen, Phys. Rev. **B 70**, 045202 (2004).
- [29] V.I. Arkhipov, E.V. Emelianova, Y.H. Tak, and H. Bässler, J. Appl. Phys. **84**, 848 (1998); V.I. Arkhipov, U. Wolf, H. Bässler, Phys. Rev. B **59**, 7514 (1999).
- [30] T. van Woudenberg, P.W.M. Blom, Appl. Phys. Lett. **82**, 985 (2003)
- [31] The steady state equation for SCLC, also called Mott-Gurney square law:  
$$J = \frac{9}{8} \frac{\epsilon}{L^3} \mu_n (V - V_{bi})^2$$
 in combination with eq. 6 is in good agreement with the I-V data on the Al/MDMO-PPV/ITO structure (not shown). This indicates that our model indeed converges to this classical description.
- [32] Y. Park, V.-E. Choong, B.R. Hsieh, C.W. Tang, Y. Gao, Phys. Rev. Lett. **78**, 3955 (1997)
- [33] J. Werner, A.F.J. Levi, R.T. Tung, M. Anzlowar, M. Pinto, Phys. Rev. Lett. **60**, 53 (1988).



### **Field and temperature dependence of the photocurrent in polymer:fullerene bulk heterojunction solar cells**

#### **Abstract**

*The photocurrent in polymer/fullerene blends is characterized as a function of bias at temperatures ranging from 125 to 300 K. Assuming a constant generation rate and bimolecular recombination the results are numerically modeled within the drift-diffusion approximation. Bimolecular recombination is found to be a dominant factor in the field dependence of the photocurrent in the entire measured voltage range. Inclusion of field dependent geminate pair dissociation and recombination via the Onsager expressions gives a much stronger field dependence than experimentally observed. From the temperature dependence of the extracted mobilities we can simultaneously estimate the broadening of the transporting HOMO and LUMO levels.*

## 4.1 Introduction

Blends of conjugated polymer and fullerene derivatives are considered promising candidates for thin film organic solar cells<sup>1</sup>. The photovoltaic response is based on an ultrafast electron transfer from the conjugated polymer excited state to the buckminsterfullerene, with a quantum efficiency close to unity<sup>2</sup>. Combined with the large interface area for charge separation due to the intimate blending<sup>3</sup> and the efficient carrier transport across the thin film, power conversion efficiencies up to 3% have been reported<sup>3, 4, 5</sup>.

In order to improve the efficiency of the solar cell, fundamental aspects of the device operation have to be examined. Some progress has already been made: the temperature dependence of the photocurrent under short-circuit conditions,  $J_{SC}$ , is observed to result from the temperature dependence in the charge transport in combination with recombination with shallow traps<sup>6</sup> and space charge effects<sup>7</sup>. Recently, geminate recombination of generated bound electron-hole pairs based on Onsager's theory was used to explain the field and temperature dependence<sup>8</sup>.

In this work, these effects will be related to gradients in the electron and hole quasi Fermi levels that ultimately induce the photovoltaic effect. This makes it possible to recognize the importance of their contributions to the photocurrent. Fonash *et al.*<sup>9</sup> in fact summed the contributions to  $J_{SC}$ . Besides an electric field that results in efficient charge separation, a carrier concentration gradient due to dissimilar diffusion coefficients for electrons and holes may contribute as well (Dember effect). This effect is estimated to be significant for transport in organic materials<sup>10</sup>.

In this paper we will model the photocurrent in MDMO-PPV:PCBM bulk heterojunction solar cells as a function of bias for different temperatures by the drift-diffusion equations. This allows us to examine how dissimilar mobilities as well as a metastable charge transfer state affect the field and temperature dependence of the photocurrent. A similar approach was recently used in the modeling of bilayer polyfluorene-based photovoltaic devices<sup>11</sup> and MDMO-PPV:PCBM cells<sup>12</sup>.

## 4.2 Results and discussion

The set of coupled partial differential equations is given by

$$\begin{aligned}
 \bar{\nabla} \cdot (\epsilon \bar{\nabla} \phi) &= q(n - p) \\
 \bar{\nabla} \cdot \bar{J}_n &= -q(-\partial_t n - R + G) \\
 \bar{\nabla} \cdot \bar{J}_p &= q(-\partial_t p - R + G) \\
 \bar{J}_n &= q(D_n \bar{\nabla} n - \mu_n n \bar{\nabla} \phi) \\
 \bar{J}_p &= q(-D_p \bar{\nabla} p - \mu_p p \bar{\nabla} \phi)
 \end{aligned} \tag{1}$$

where  $\phi$  denotes the electric potential,  $n$  and  $p$  are the free carrier concentrations of electrons and holes, and  $J_n$  and  $J_p$  are the electron and hole current density, respectively.  $D_n$ ,  $D_p$ ,  $\mu_n$  and  $\mu_p$  are the diffusion coefficients and the mobilities of electrons and holes, respectively.  $R$  is the recombination rate,  $G$  the generation rate and  $\epsilon = \epsilon_r \epsilon_0$  with  $\epsilon_0$  the permittivity of vacuum and  $\epsilon_r$  the relative permittivity that is assumed constant. The Einstein relation for diffusion,  $D_{n/p} = k_B T / q \mu_{n/p}$ , is assumed to hold, where  $k_B$  is the Boltzmann constant,  $T$  the temperature and  $q$  the elementary charge.

Numerical solution of the above system of equations is far from trivial. The system of equations is singularly perturbed<sup>13</sup> and highly nonlinear. Dedicated numerical methods have been

developed to solve the system, and they turn out to be essential for a robust and efficient solution. The Scharfetter-Gummel discretization scheme must be used to discretize the current densities, whereas damped Newton methods<sup>14</sup> or nonlinear variable transformations<sup>15</sup> are essential for the solution of the extremely nonlinear systems of discretized equations. A thorough description of all numerical methods used for semiconductor device simulation is given in ref. 16, the simulations described in this paper have been performed using the software package CURRY, developed within Philips Research.

It is generally understood that electrons and holes in these devices are transported through the PCBM and MDMO-PPV phase, respectively. Due to intimate blending percolative paths are formed that strongly depend on morphology. This limits the validity of the drift-diffusion equations, as the carrier mobility cannot be rigorously defined from the expectation value of the scattering time (relaxation time approximation). Therefore, the results only give a semi-empirical description of the transport via a functionalized mobility in terms of field, temperature and/or concentration. In the calculations presented here we consider the mobilities as a function of temperature only. Given the bias range, this restriction is not severely limiting (at 2 V typically a factor of 2 increase results) and merely allows us to reduce the number of free variables.

Prior to sample preparation, the ITO covered glass substrates were first cleaned by ultrasonic treatment in acetone, rubbing with soap, rinsing with de-mineralized water, refluxing with iso-propanol, and finally 20 minutes UV ozone treatment. Subsequently, a 100 nm thick layer of polyethylenedioxythiophene: polystyrenesulfonate (PEDOT:PSS) was spin coated (1500 rpm; 90s) from an aqueous dispersion under ambient conditions on the cleaned substrates and dried by annealing for 1 minute at 180° C. Then a 90 nm thick layer was spin coated (1000 rpm; 90s) on top of the PEDOT:PSS from a chlorobenzene solution consisting of poly[2-methoxy-5-(3',7'-dimethyloctyloxy)-1,4-phenylene vinylene] (MDMO-PPV) and 1-(3-methoxycarbonyl)propyl-1-phenyl-[6,6]-methanofullerene (PCBM) in the mixing ratio 1:4 (by weight), which was stirred vigorously overnight in the dark. The substrates were then transferred into a glovebox filled with

nitrogen atmosphere ( $[O_2] < 1$  ppm and  $[H_2O] < 1$  ppm). From there, they were introduced in a vacuum deposition chamber ( $p \sim 10^{-6}$  mbar). 1.0 nm of LiF and 100 nm of Al were deposited right after each other while the sample temperature was kept below 40° C. Inside the glovebox, the samples were mounted in a variable temperature continuous flow cryostat, which was subsequently evacuated. The  $I$ - $V$  characterization was performed using a Keithley 2410 source meter.

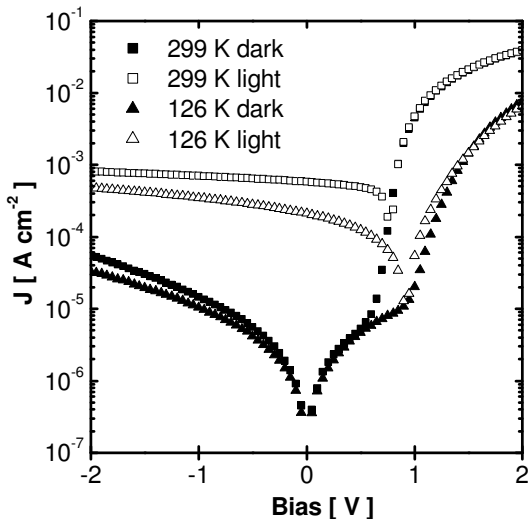


**Figure 1:**  $I$ - $V$  characterization on polymer:fullerene bulk heterojunction solar cells in the dark and under illumination at 299 K and 126 K. Absolute values are shown: the dark conductivity is negative below 0 V and under illumination below  $\sim 0.8$  V.

In figure 1 the  $I$ - $V$  characteristics are given in the dark and under illumination for two temperatures. In figure 2 the photocurrent ( $J_{ph}$ ) and open-circuit potential ( $V_{oc}$ ) at 299 K are determined by subtracting the current obtained in the dark from that under illumination. In the absence of gap states the recombination is given by the bimolecular recombination rate, which we assume to be described by the Langevin equation  $R = \gamma n p$ , with  $\gamma = e(\mu_n + \mu_p)/(\epsilon_0 \epsilon_r)$ .<sup>17, 18</sup> The generation rate,  $G = G_0$ , is assumed uniform. The dashed curve is obtained for mobilities that were taken from literature<sup>8</sup> ( $\mu_n = 2.0 \times 10^{-3}$  and  $\mu_p =$

$1.4 \times 10^{-4} \text{ cm}^2/\text{Vs}$ ). Here, the only free parameter was  $G_0$  which determines the saturation value for the photocurrent. The thin line in Fig. 2 indicates the theoretical maximum device output,  $eG_0l$ , with  $l$  the layer thickness. The solid line is obtained by including the mobilities in the optimization procedure, which yielded somewhat different values for  $\mu_n$  ( $2 \times 10^{-2}$ ) and  $\mu_p$  ( $2 \times 10^{-5}$ ).

The decrease in  $J_{\text{ph}}$  at lowering bias is due to the reduced field in the device. Close to the open circuit voltage it is strongly determined by diffusion and recombination. To disentangle these factors we repeated the calculation of the dashed curve with  $R=0$  (dash-dotted line). Actually, this calculation reproduces the analytical result of Sokel and Hughes<sup>19</sup>. From the difference between the dashed and dash-dotted line, it is evident that Langevin recombination is the dominant loss mechanism in the entire measured bias range.

From the above results we conclude that the field dependence in the photocurrent can be adequately described by a constant generation rate and bimolecular recombination with dissimilar mobilities. Finally, we notice that for the used parameter sets, the modeled photocurrent is, at all shown biases, linear in the light intensity, in agreement with experimental observations<sup>6,20</sup>. This finding indirectly refutes that bimolecular recombination always yields a non-linear light intensity dependence<sup>6,20</sup>.

An alternative route<sup>8</sup> to improve the correspondence is to assume the presence of a metastable bound charge transfer (CT) state. In optical experiments in these solar cells, the presence of a CT state has been shown.<sup>2</sup> However, its bound nature has not explicitly been demonstrated. After generation, such an  $e-h$  pair may either decay to the ground state with (constant) rate  $k_f$ , or dissociate with rate  $k_e(E)$  into free carriers. This then leads to an explicit field dependence in the generation and recombination rate. In the presence of such a charge transfer state the generation is described by a rate constant times the probability for the bound  $e-h$  pair to escape the attractive Coulomb force:

$$\hat{G}(T, E) = G_0 \frac{k_e(T, E)}{k_e(T, E) + k_f}, \text{ where} \quad [2]$$

$$k_e(T, E) = k_0 \left( 1 + b + \frac{b^2}{3} + \dots \right), \text{ with} \quad [3]$$

$$b = \frac{e^3 E}{8\pi\epsilon_r\epsilon_0 k_B^2 T^2}$$

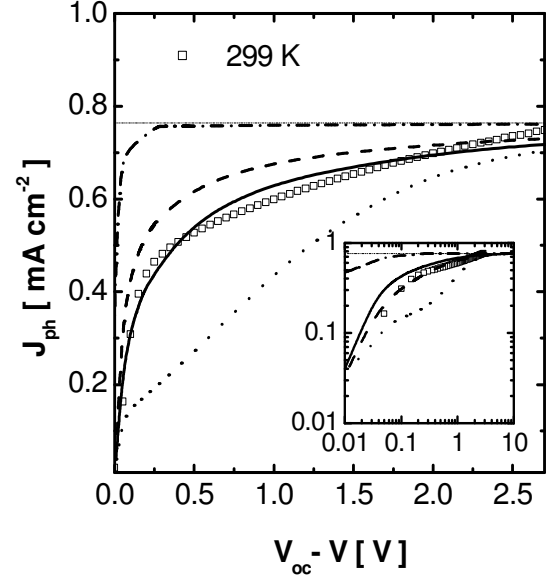


**Figure 2:** The photocurrent versus bias obtained at 299 K (squares). The curves give the numerical solution of the drift-diffusion equation after optimizing  $G_0$  (dashed),  $G_0$ ,  $\mu_e$  and  $\mu_h$  (solid), including the presence of a charge transfer state ( $k_f/k_0=15$ , dotted) and in the absence of recombination (dash-dotted). The thin line indicates the maximum output  $J_{\text{ph}}=eG_0l$ . The inset shows the same data on a double-log scale.

Here  $k_0$  is the zero-field rate constant. The expression between brackets follows from Onsager's theory<sup>21</sup> commonly applied to describe the field and temperature dependence of photocurrent generation<sup>18</sup>. In order to provide a consistent description, the bimolecular recombination must simultaneously be reduced to account for the possibility of re-ionization,

$$\hat{R}(T, E) = R_0 \frac{k_f}{k_e(T, E) + k_f}, \quad [4]$$

where  $R_0$  is the bimolecular recombination rate previously described.

This description deviates from the numerical model used in ref. [8] in the way the Onsager expression is incorporated to describe the field dependence of  $G$  and  $R$ . The only additional free parameter in this implementation is the ratio  $k_f/k_0$ .

After optimizing  $k_f/k_0$ , with  $\mu_n = 2.0 \times 10^{-3}$  and  $\mu_p = 1.4 \times 10^{-4}$  cm<sup>2</sup>/Vs, the dotted curve is found. A much stronger field dependence in the photocurrent is found than experimentally observed. Mihailetschi *et al.*<sup>8</sup> showed that when a distribution of  $k_0$ , resulting from a spread in electron-hole separations in the CT state, is used, much better agreement with experiment is obtained. Actually, the increased slope in  $J_{ph}$  prior to high-field saturation is reproduced by this means (see inset). In the field range studied here, in which only the onset of this feature is visible, the distribution in  $k_0$  effectively switches off the field dependence of eq. 3<sup>22</sup> and hence we can ignore the field dependence in the generation rate.

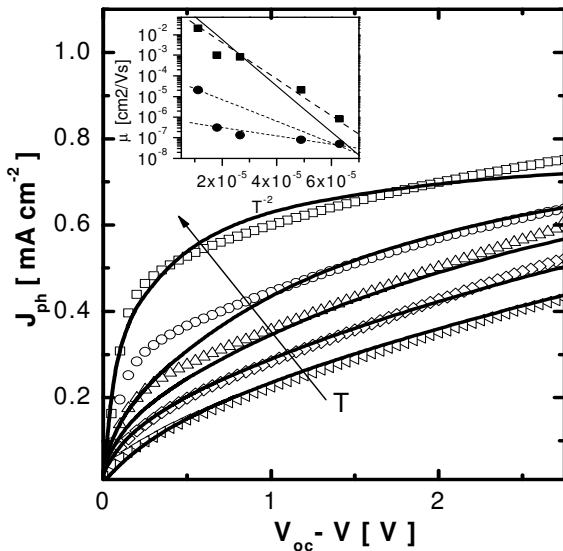


**Figure 3:** *The temperature dependence of the photocurrent versus bias. The solid curves are obtained by fitting the electron and hole mobility.  $G_0$  was determined at 299 K and kept constant.  $T = 299, 235, 194, 143, 126$  K (top to bottom). Inset: electron (squares) and hole (circles) mobilities used in the calculation vs.  $T^{-2}$ . Lines are fits to  $\mu \sim \exp[-(3\sigma/5k_B T)^2]$ . The solid line corresponds to  $\sigma = 0.073$  eV.*

In fig 3 several photocurrents are shown at different temperatures. By only altering the mobilities while retaining the same generation rate, good agreement is obtained at all temperatures. At intermediate temperatures (194-235 K) and low bias (<1 V) deviation from experimental data is observed by at most 30%. This deviation can be overcome by decreasing the prefactor,  $\gamma$  in the Langevin description for recombination. Note that recombination coefficients as large as predicted by Langevin recombination are not generally observed in low mobility disordered materials<sup>23, 24</sup>. Although it is clear that by addition of another fit parameter the agreement with experiment can be increased, it is beyond the scope of this paper to recognize this prefactor from photoelectrical characterization. Moreover, when including this prefactor together with the electron and hole mobility as free parameter, the transport description does not yield a unique set of parameters.

The electron and hole mobilities that were used in these calculations are plotted vs.  $T^{-2}$  in the inset of fig. 3. Fitting these values with  $\mu(T) \sim \exp[-(3\sigma/5k_B T)^2]$  enables us to make an estimate of the broadening of the PCBM LUMO and PPV HOMO levels<sup>25</sup>. For



PCBM we find  $\sigma_{\text{LUMO}} \approx 0.065$  eV, in good agreement with the value of 0.073 reported in Ref. 23. For MDMO-PPV we find  $\sigma_{\text{HOMO}} = 0.03\text{-}0.05$  eV. Despite the relatively large uncertainty, these values are clearly below the value of 0.11 eV found for pure MDMO-PPV. This is consistent with the finding of Melzer *et al.* that the hole mobility in MDMO-PPV is enhanced upon blending with PCBM<sup>26</sup>, since it is reasonable to expect that a reduced disorder results in an enhanced mobility. As an independent confirmation, we found that the mobilities reported here are entirely consistent with the (temperature dependent) impedance spectra taken on the same samples<sup>27</sup>. Finally, we note that in our modeling, the temperature dependence of  $J_{ph}$  in the entire bias range is explained by the temperature dependence of the carrier mobilities rather than the  $T$ -dependence of the generation rate.<sup>8</sup>

### 4.3 Conclusions

In summary, we demonstrate that the field and temperature dependence of photocurrents in bulk heterojunction organic solar cells can be explained in terms of the drift-diffusion equations by inclusion of bimolecular recombination. The modeling enables us to simultaneously estimate the broadening of the PCBM LUMO level and PPV HOMO level. In addition, we modified the generation and recombination rate to account for the presence of the charge transfer state and included Onsager's theory for geminate recombination. The resulting field dependence appears too strong to explain the observed photocurrent.

### 4.3 References and notes

- [1] C.J. Brabec, N.S. Sariciftci, J.C. Hummelen, *Adv. Functional Mater.* **11**, 15 (2001); H. Hoppe and N.S. Sariciftci, *J. Mater. Res.*, **19** (2004) 1924; K.M. Coakley and M.D. McGehee, *Chem. Mater.*, **16** (2004) 4533.
- [2] N.S. Sariciftci, L. Smilowitz, A.J. Heeger, F. Wudl, *Science* **258**, 1474 (1992).
- [3] S.E. Shaheen, C.J. Brabec, N.S. Sariciftci, F. Padinger, T. Fromherz, J.C. Hummelen, *Appl. Phys. Lett.* **78**, 841 (2001).
- [4] C.J. Brabec, S.E. Shaheen, C. Winder, N.S. Sariciftci, P. Denk, *Appl. Phys. Lett.* **80**, 1288 (2002).
- [5] P. Schilinsky, C. Waldauf, C.J. Brabec, *Appl. Phys. Lett.* **81** 3885 (2002).
- [6] I Riedel, J. Parisi, V. Dyakonov, L. Lutsen, D. Vanderzande, J.C. Hummelen, *Adv. Functional Mater.* **14**, 38 (2004).
- [7] J. Nelson, *Phys. Rev. B* **67**, 155209 (2003).
- [8] V.D. Mihailetschi, L.J.A. Koster, J.C. Hummelen, P.W.M. Blom. *Phys. Rev. Lett.* **93**, 216601 (2004).
- [9] S.J. Fonash, S. Ashok, *Appl. Phys. Lett.* **35**, 535 (1979).
- [10] J. Nelson, *The Physics of Solar Cells*, 1<sup>st</sup> ed. (Imperial College Press, London, 2003).
- [11] J.A. Barker, C.M. Ramsdale, N.C. Greenham, *Phys. Rev. B* **67**, 075205 (2003).
- [12] L. J.A. Koster, V.D. Mihailetschi, P.W.M. Blom, *Proc. SPIE* **5520**, 200 (Eds. Z.H. Kafafi and P.A. Lane, Denver, USA, 2004).
- [13] P.A. Markowich, *SIAM J. Appl. Math.*, vol. 5, pp. 896-928 (1984).
- [14] R.E. Bank, D.J. Rose, *Numer. Math.*, vol. 37, pp. 279-295 (1981).
- [15] S.J. Polak, C. den Heijer, W.H.A. Schilders, P.A. Markowich, *Int. J. Numer. Methods Eng.*, vol. 24, pp. 763-838 (1987).
- [16] W.H.A. Schilders, *Numerical Methods for Semiconductor Device Simulation*, volumes I and II, Springer, Vienna (to appear).
- [17] Langevin, *Ann. Chim. Phys.* **28**, 433 (1903).
- [18] M. Pope, C.E. Swenberg, *Electronic Processes in Organic Crystals and Polymers*, 2<sup>nd</sup> ed. (Oxford University Press, Oxford, 1999).
- [19] R. Sokel, R.C. Hughes, *J. Appl. Phys.* **53**, 7414 (1982).

[20] J.K.J. van Duren, X. Yang, J. Loos, C.W.T. Bulle-Lieuwma, A.B. Sieval, J.C. Hummelen, R.A.J. Janssen, *Adv. Funct. Mat.* **14**, 425 (2004).

[21] L. Onsager, *J. Chem. Phys.* **2**, 599 (1934).

[22] P.W.M. Blom, private communication.

[23] A. Privikas, G Juška, A.J. Mozer, M. Scharber, K. Arlauskas, N.S. Sariciftci, H. Stubb, R. Österbacka, *Phys. Rev. Lett.* **94**, 176806 (2005).

[24] E.A. Schiff, *J. Non-Cryst Solids* **190**, 1 (1995) and references therein.

[25] V.D. Mihailechi, J.K.J. van Duren, P.W.M. Blom, J.C. Hummelen, R.A.J. Janssen, J.M. Kroon, M.T. Rispens, W.J. Verhees, and M.M. Wienk, *Adv. Funct. Mat.* **13**, 43 (2003).

[26] C. Melzer, E.J. Knoop, V.D. Mihailechi, P.W.M. Blom, *Adv. Funct. Mat.* **14**, 865 (2004).

[27] H.H.P. Gommans, M. Kemerink, J.M. Kramer, R.A.J. Janssen, unpublished.

### Negative capacitances in low-mobility solids

#### Abstract

*The negative capacitance as often observed in semiconducting devices is explained by bipolar injection in diode configuration. Numerical calculations within the drift-diffusion approximation are performed and relations with bias, sample dimensions and carrier mobilities are presented in case of bimolecular recombination. Finally, measurements conducted on a light emitting diode and photovoltaic cell based on low-mobility organic semiconductors are modeled as a function of bias and temperature, respectively.*

## 5.1 Introduction

Admittance spectroscopy has proven to be a powerful and nondestructive method to study transport properties in dielectric materials. Recently, negative capacitances have been reported on a variety of devices that were based on organic materials<sup>1-4</sup> or on crystalline or amorphous inorganic semiconductors.<sup>5-14</sup> Equally numerous explanations for this negative capacitance (NC) have been presented that involved minority carrier flow<sup>1, 3, 4, 5</sup>, interface states<sup>9, 13</sup>, slow transient time of injected carriers<sup>14</sup>, charge trapping<sup>2, 3, 10, 11, 12</sup> or space charge.<sup>6</sup> The bulk of these descriptions are either based on phenomenological arguments or based on device representation in an equivalent circuit. However, such representations are not necessarily related to the physical properties of the system, despite the fact that they mimic the measured spectra.

Here, we will derive the NC from numerical solutions for Boltzmann transport in the drift-diffusion approximation for bipolar transport. Such description will provide a general understanding that includes the phenomena of minority carriers, space charge and the slow transient time of the injected carriers. In order to conduct such general investigation, interface and trap states are not considered, although their effect on the capacitance is beyond dispute. We will demonstrate the NC behavior in diode configuration for various recombination rates and successively present numerical scaling relations in the limiting cases in terms of sample dimensions, bias and carrier mobilities.

In the second part of this chapter the capacitance is experimentally determined for two devices based on low-mobility organic semiconductors: a light emitting diode (LED) and a photovoltaic cell (PVC). For the active layer in the LED the PPV-derivative MDMO-PPV is used, which has attracted worldwide attention in academia and industry for its favorable combination of solubility and optoelectronic properties. The PVC consists of a blend of MDMO-PPV and a methanofullerene (PCBM) that has demonstrated a power conversion efficiency of 2.5 %<sup>15-16</sup>.

Admittance spectra on MDMO-PPV based LEDs have previously been reported as a function of bias<sup>1, 3</sup>. It was observed that the light onset coincided with the onset for the NC<sup>1</sup>, which is a strong indication for the existence of a relation between minority carrier (electron) flow and the occurrence of a negative capacitance. This is indeed found to be the case, and we demonstrate that on basis of characteristic features in the capacitance it is possible to determine the two carrier mobilities and recombination rate simultaneously as a function of bias and temperature.

The advantage over alternative electrical characterization techniques such as *I-V* characterization or time-of-flight (TOF) in the determination of the minority carrier mobility is that there is no need for modifications of the original device: In *I-V* characterization the majority carrier contribution is generally repressed by altering the contacts. In TOF measurements film thicknesses are restricted to values much larger than the optical absorption depth, which is usually far above the thickness used in typical, optimized devices. Submitting to these requirements unintentionally leads to altering the transport properties of the system.

Moreover, it will be demonstrated that in case the frequency range is sufficiently large, recombination rate constants can be determined.

## 5.2 Theory

The set of coupled partial differential equations is given by

$$\begin{aligned}
 \bar{\nabla} \cdot (\varepsilon \bar{\nabla} \phi) &= q(n - p) \\
 \bar{\nabla} \cdot \bar{J}_n &= -q(-\partial_t n - R) \\
 \bar{\nabla} \cdot \bar{J}_p &= q(-\partial_t p - R) \\
 \bar{J}_n &= q(D_n \bar{\nabla} n - \mu_n n \bar{\nabla} \phi) \\
 \bar{J}_p &= q(-D_p \bar{\nabla} p - \mu_p p \bar{\nabla} \phi)
 \end{aligned} \tag{1}$$

where  $\phi$  denotes the electric potential,  $n$  and  $p$  are the free carrier concentrations of electrons and holes, and  $J_n$  and  $J_p$  are the electron and hole current density, respectively.  $D_n$ ,  $D_p$ ,  $\mu_n$  and  $\mu_p$  are the diffusion coefficients and the mobilities of electrons and holes, respectively.  $R$  is the recombination rate and  $\varepsilon = \varepsilon_r \varepsilon_0$  with  $\varepsilon_0$  the permittivity of vacuum and  $\varepsilon_r$  the relative permittivity that is assumed constant. The Einstein relation for diffusion,  $D_{n/p} = k_B T / q \mu_{n/p}$ , is assumed to hold, where  $k_B$  is the Boltzmann constant,  $T$  the temperature and  $q$  the elementary charge.

The numerical solution of Eqs. 1 has been described previously in ref 17. A description of all numerical methods used for semiconductor device simulation is given in ref 18. The simulations described in this paper have been performed using the software package CURRY, developed within Philips Research.

In case diffusion currents are neglected, a zero electric field is the logical boundary condition at an ohmic contact. When including diffusion, it is more realistic to apply the free carrier density at the interface,  $\rho_i$ , for the boundary condition, according to:

$$\rho_i = n_{metal} \exp\left(-\frac{\Delta\phi}{kT}\right),$$

with  $\Delta\phi$  the effective barrier height for carrier injection from the metal Fermi level into the transport level of the dielectric and  $n_{metal}$  the carrier density in the metal. As an ohmic contact is required to probe the bulk properties,  $\Delta\phi$  must be small, ( $\leq 0.2$  eV), and  $\rho_i$  may become unrealistically large, i.e. larger than the density of states (DOS) of the dielectric. Hence, in order to model an ohmic contact we set  $\rho_i$  equal to the DOS of the dielectric ( $= 10^{21}$  cm<sup>-3</sup>). In the description of the polymer LED a non-ohmic contact will be considered for electron injection and hence a smaller charge concentration will be used at the metal-polymer interface.

In the absence of gap states the recombination is given by the bimolecular recombination rate,  $R = \gamma n p$ , where  $\gamma$  is the recombination rate constant<sup>19</sup>. This constant is generally set equal to  $\chi = e(\mu_n + \mu_p) / (\varepsilon_0 \varepsilon_r)$  as derived by Langevin<sup>20</sup> although smaller values have been generally found in disordered molecular<sup>21</sup> and inorganic materials<sup>22</sup>. For this reason the capacitance is calculated for a variety of recombination rate constants in diode configuration assuming bipolar injection from ohmic contacts, see Fig. 1. The material parameters as used in the calculations are given in the figure caption.

First note that the negative capacitance for bipolar injection is indeed found in the drift-diffusion approximation. At sufficiently low frequencies all capacitances converge to a constant negative value, while at sufficiently high frequencies the geometrical capacitance is obtained. The physical argument for the NC is equivalent to the well-known reduction of the capacitance to  $\frac{3}{4}$  of the geometrical capacitance  $C_{geo}$  for unipolar space-charge limited currents at frequencies below the

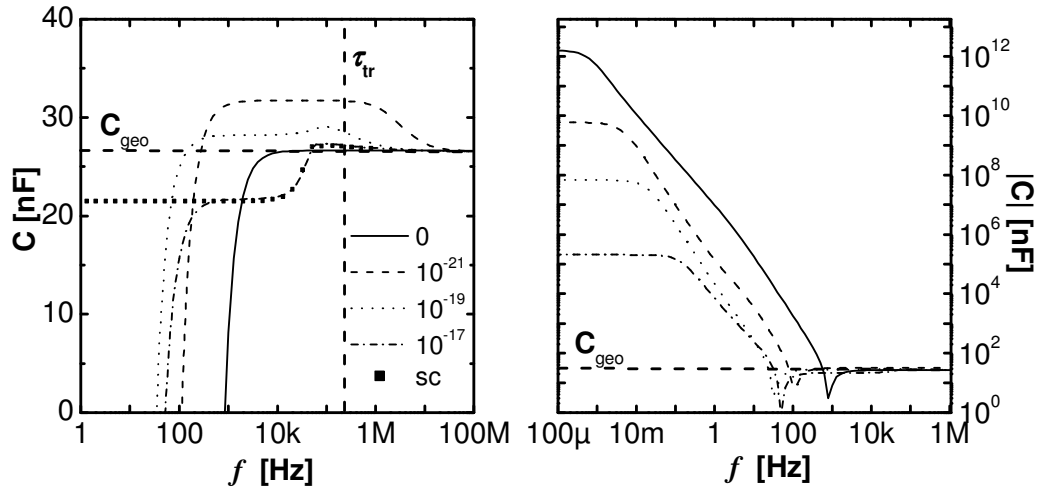


**Figure 1:** Left: Capacitance,  $C(f)$ , in a dielectric medium for various recombination constants,  $\gamma$  (as given in the inset in  $\text{cm}^3/\text{s}$ ) and for a single carrier (sc) (hole only) device. Here, the layer thickness,  $L$ , is  $100 \text{ nm}$ , the surface area,  $A$ , is  $1 \text{ cm}^2$ , the relative permittivity,  $\epsilon_r$ , is  $3$ , the bias is  $5 \text{ V}$ , and the mobility for holes,  $\mu_p$ , is  $10^{-6} \text{ cm}^2/\text{Vs}$  and electrons,  $\mu_n$ , is  $10^{-12} \text{ cm}^2/\text{Vs}$ . The geometrical capacitance is indicated with  $C_{\text{geo}}$ . Right: Absolute value of the capacitance,  $|C(f)|$ .

reciprocal transit time<sup>23</sup>. Since the (differential) capacitance reflects the (change in) stored charge per (change in) bias, the presence of (additional) space charge in the dielectric gives rise to a deviation  $\Delta C$  from the geometrical capacitance. Since the build-up of space-charge necessarily lags behind the stimulus,  $\Delta C$  is negative. For bipolar currents, the amount of stored space charge can, depending on the recombination strength, be much larger than in the unipolar situation due to the compensation of positive and negative charge carriers<sup>24</sup>. Hence, the magnitude of  $\Delta C$  is enhanced as well, and the total capacitance  $C_{\text{geo}} + \Delta C$  may, for sufficiently weak recombination, eventually become negative. The relevant time scales can be best understood in the carrier transient response to a step potential<sup>14</sup>: For a short time period after the voltage step, such that even the fastest carriers cannot respond, only the displacement current contributes to the (geometrical) capacitance, which is determined by the dielectric permittivity. Subsequently, as both injection contacts are set ohmic, the fastest carriers (holes) will determine the transient field in the following time interval. This field is maintained until the second (electron) carrier response sets in, resulting in modification of this (hole dominated) transient field. However, this modification is closely followed by the hole response. For each time unit the hole and electron current will increase until the field, and thus the currents, have converged towards their final equilibrium configuration that is determined by both mobilities and the recombination rate<sup>25</sup>. At high recombination rates space charge will dominate the electric field in the whole dielectric layer. For smaller recombination rates the area that is dominated by space charge will decline up to near the injecting contacts. Finally, for zero recombination this area is confined to the immediate vicinity of the contacts while in the remaining of the layer the field is simply  $V/L$ , where  $V$  is the applied bias and  $L$  is the distance between the electrodes.

From figure 1 it can be immediately observed that indeed the recombination rate highly affects the capacitance. At a high recombination rate the frequency resolved capacitance clearly exhibits a transition from  $21.5$  to  $26.6 \text{ nF}$  at  $\sim 10 \text{ kHz}$  that is absent for lower recombination rates. This transition is a consequence of the (positive) space charge and corresponds to the transit time effect as obtained for a single carrier space charge limited configuration that was discussed above. Shao *et al*<sup>25</sup>, demonstrated this effect for drift-only transport and calculated that the capacitance at frequencies smaller than the transit time,  $\tau_{\text{tr}} = (2L)^2 (3\mu_p V)^{-1}$ , is exactly  $\frac{3}{4}$  of the geometrical

capacitance. The ‘low’ frequency capacitance slightly differs in case diffusion is accounted for. The characteristic transition reproduces exactly the transition for a single carrier device as indicated in fig 1.

With decreasing recombination the low-frequency saturation value of the (negative) capacitance increases in magnitude, as expected from the discussion above. In the limit of zero recombination space charge effects become negligible and the contacts determine the ac response. Here, it is observed that the transition from the constant negative capacitance towards the (constant) geometrical capacitance covers six decades in the frequency domain, corresponding to the six order-of-magnitude difference in carrier mobility. In fact, this transition is observed to decrease in the frequency range with increasing recombination rate. This can be understood in relation to the foregoing discussion in the transient response picture: The equilibrium electron concentration throughout the dielectric layer is much smaller for the space charge dominated field than for  $V/L$ , and hence less electrons have to penetrate the layer less far in order to reach equilibrium.

In the admittance experiments on polymer based devices the NC will be examined to determine the minority carrier mobility and where possible the recombination constant. In this analysis we will use the frequency  $f_0$  for which  $C(f_0) = 0$  as characteristic for the (reciprocal) time scale on which the bimolecular current reaches equilibrium. In figure 2,  $f_0$  is shown for variations in the electron and hole mobility, the applied bias and the layer thickness that appear meaningful in experimental configurations. It is shown that for all combinations within

this range  $f_0$  can be scaled onto a straight curve by  $f_0 \propto \frac{V}{L^2} (\mu_n \mu_p)^{0.62}$ . Variations in  $\mu_p$  are explicitly indicated in figure 2. The power in the mobilities is a numerical approximation that, considering the experimental limitations, yields sufficient accuracy. The recombination constant as chosen here ( $0.01 \times \gamma_L$ ) leads to a space charge dominated field and can thus be considered strong recombination; taking a larger recombination constant consequently leads to the same scaling. The variations in height for the different hole mobilities in figure 2 are due to their effect on the recombination rate constant,  $\gamma_L$ .

Although it is dangerous to use hand waving arguments to interpret such complex phenomena as bipolar impedance spectra, we argue one can qualitatively understand the scaling behavior of  $f_0$ . We start from the well-known Parmenter-Ruppel expression for the bipolar space-charge limited current in steady-state

$$J \propto \epsilon_0 \epsilon_r \sqrt{\frac{\mu_e \mu_h (\mu_e + \mu_h)}{\mu_r}} \frac{V^2}{L^3},$$

where  $\mu_r$  is the recombination mobility that for Langevin-type recombination is given by  $\mu_r \propto \mu_n + \mu_p$ . Therefore, we have  $J \propto \epsilon_0 \epsilon_r \sqrt{\mu_e \mu_h} V^2 / L^3$ . Now, by analogy with the unipolar situation, where the characteristic frequency of a space-charge limited current of magnitude

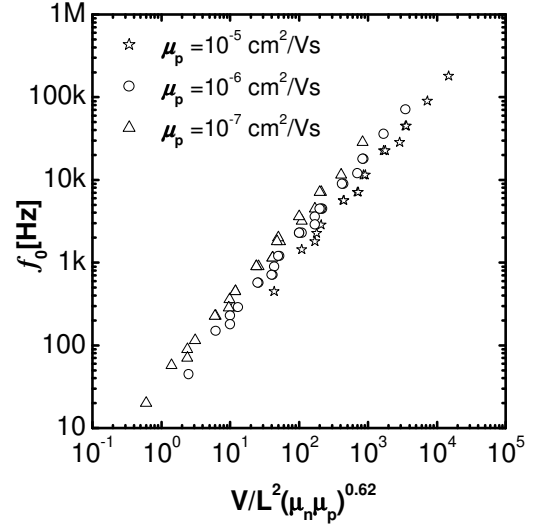


**Figure 2:** Zero capacitance frequency,  $f_0$ , for different bias (2-10V), layer thickness (50-200 nm), electron mobility ( $10^{-9}$ - $10^{-7}$   $\text{cm}^2/\text{Vs}$ ) and hole mobility ( $10^{-7}$ - $10^{-5}$   $\text{cm}^2/\text{Vs}$ ). The recombination constant was chosen to be  $0.01 \times \gamma_L$ . The remaining parameters were set as in figure 1.



$J \propto \epsilon_0 \epsilon_r \mu V^2 / L^3$  is given by  $f \propto \mu V / L^2$ , one expects for  $f_0$   $f_0 \propto \sqrt{\mu_e \mu_h} V / L^2$ . Surprisingly, the scaling that follows from the exact model only differs from this prediction only in the exponent of the mobility, despite the fact that both diffusion and the large carrier densities near the contacts are ignored.

In case the recombination rate is set zero we obtain similar results as in figure 2 by scaling  $f_0 \propto \frac{\sqrt{\mu_n \mu_p}}{L}$ . As the bias is always a straightforward tunable variable, this gives a handle to discriminate between the two limits. Obviously, this becomes less straightforward in case the mobility is a function of the electric field<sup>25</sup> or the density<sup>26</sup>.

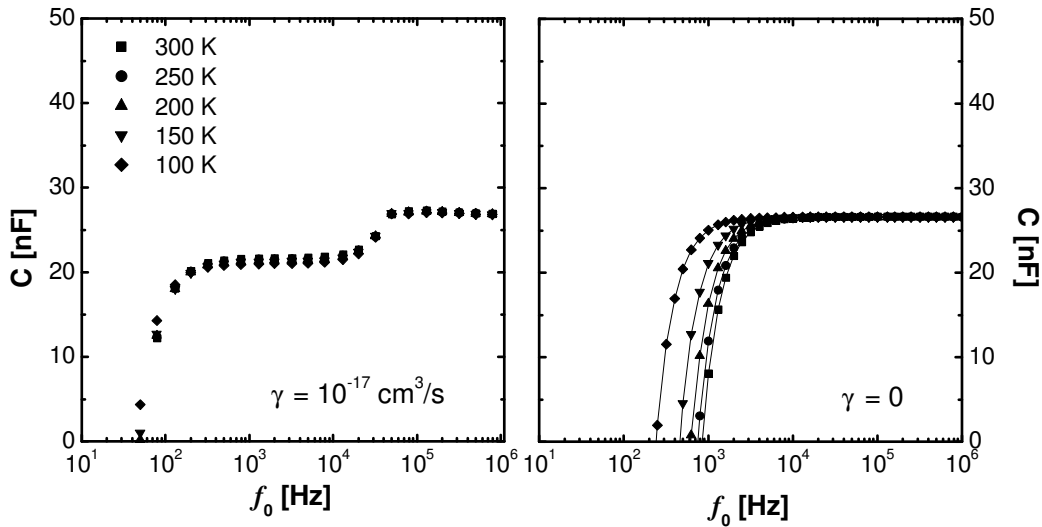


**Figure 3:** Capacitance,  $C(f)$ , in a dielectric medium for  $\gamma = 10^{-17} \text{ cm}^3/\text{s}$  (left) and 0 (right) at different temperatures (see inset). The remaining parameters were set as in figure 1.

The temperature dependence in the range of 100-300 K has been determined in both recombination limits as well and the results are shown in figure 3. It can be observed that for devices with a space charge dominated field the temperature and hence the diffusion coefficient,  $D$ , does not affect the capacitance. This turns out to be very useful as the experimentally derived capacitance (more specific  $f_0$ ) can now be directly related to the mobilities as a function of temperature as will be demonstrated below. This is in contrast to the situation for zero recombination as can be seen in figure 3. In our diode configuration the temperature only determines the flow and hence the field near the injecting contacts. In the frequency range where the fastest carriers contribute to the capacitance these temperature induced field modifications near the contacts are marginal compared to the space charge in the remaining layer in case of high recombination rate. However, as for a small recombination rate the space charge becomes confined at the injecting contacts the capacitance is very sensitive for these temperature changes.

### 5.3 Experimental

In order to determine the minority carrier mobility in organic devices without modifying the charge injecting contacts admittance spectroscopy has been conducted on a polymer LED and solar cell. The polymer LED consists of a photoactive layer, poly[2-methoxy-5-(3',7'-dimethyloctyloxy)-1,4-phenylene vinylene] (MDMO-PPV), sandwiched between an indium-tin-oxide (ITO) substrate

and Al top layer. The manufacturing procedure as described in ref 1 has been followed. The thickness of the MDMO-PPV layer was 170 nm. The spectra in fig 4 were taken at room temperature for different forward bias. From electroluminescence the onset of light emission was observed at a bias of 4 V. Simultaneously, the negative contribution to the capacitance sets in and is found to extend up to higher frequencies with increasing bias.

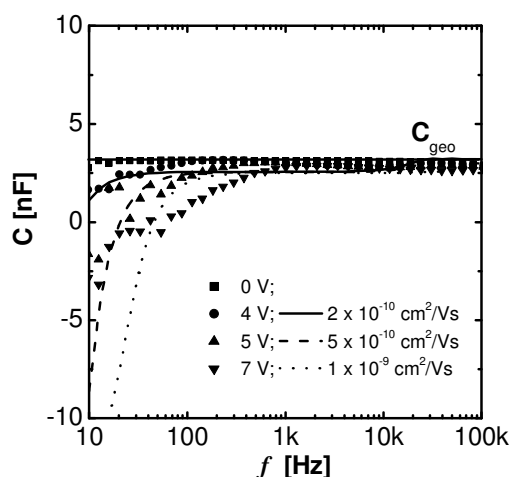


**Figure 4:** Capacitance,  $C(f)$ , in a polymer LED structure at room temperature for different bias (see inset). The geometrical capacitance is indicated with  $C_{geo}$ . The electron mobility is given in the graph for each bias.

At 0 V the capacitance equals the geometrical capacitance with a small deviation ( $>10$  kHz) due to the contact resistance (fig. 4). The hole mobility is  $2 \times 10^{-6} \text{ cm}^2/\text{V s}$  at 4-5 V and  $5 \times 10^{-6} \text{ cm}^2/\text{V s}$  at 7 V as determined in our earlier work by the transit time effect<sup>1</sup>. Identical values were determined from the steady state conductivity (not shown). The relative permittivity of MDMO-PPV is  $\sim 3$ . Electron injection from the Al into the LUMO is considered non-ohmic.<sup>1</sup> Consequently, the charge concentration at the Al interface is included as a constant and determined from the capacitance spectra ( $9 \times 10^{15} \text{ cm}^{-3}$ ), just as the recombination rate ( $\chi/1000$ ). Only the electron mobility,  $\mu_n$ , was optimized for each spectrum at  $f_0$  and the values are given in fig 4.

Although the characteristic features of the experimental data are reproduced by the calculations, there is generally an overestimation of the calculated slope in negative capacitance. The calculated curves

also seem to underestimate the capacitance prior to the onset of the negative capacitance, in for instance the range of 0.1-10 kHz at 4 V. The agreement with the experimental data in this range could be improved by reducing the recombination rate constant. In fig. 1 it can be observed that for small recombination rates the calculated capacitance equals the geometrical capacitance down to  $\sim f_0$ . However, the experimental capacitance decreases with increasing frequency in this range. This behavior is likely related to the presence of traps as with increasing frequency the number of charges that escape the trap level decreases<sup>27</sup>. Although traps are known to be present in these samples, their density and distribution in space and energy are unknown<sup>1</sup>. Hence, in the calculations trap levels have not been considered.

Both the electron and hole mobilities exhibit the (apparent) field dependence typically observed in disordered molecular materials,  $\mu_{n/p} = \mu_0 \exp(\beta\sqrt{E})$ . The values of  $\beta$  and  $\mu_0$  that are derived from the extracted values of  $\mu_p$  were found to be in good agreement with values reported in literature<sup>1</sup>. Since trapping effects, that are of importance in the same frequency range as  $f_0$  are not accounted for in the model we refrain from extracting  $\beta$  and  $\mu_0$  from the used values of  $\mu_n$ . Finally, it should be pointed out that the NC cannot directly be related to the electron mobility as was assumed in Ref. 4.

The bulk heterojunction solar cell consists of a blend of donor material MDMO-PPV and the electron accepting material 1-(3-methoxycarbonyl)propyl-1-phenyl-[6,6]- fullerene (PCBM) in the mixing ratio 1:4 (by weight). For the I-V characterization the front electrode was a 100 nm thick layer of polyethylenedioxythiophene:polystyrenesulfonate (PEDOT:PSS) spin coated on top of an ITO substrate. For the back electrode LiF (1 nm) and subsequently Al (100 nm) were thermally deposited onto the bulk heterojunction layer ( $\sim 90$  nm). The details of the manufacturing procedure are described in ref 17. The admittance spectra were taken at various temperatures between 80-300

K. At high temperatures ( $>194$  K) the value of the electron mobility of the PCBM phase is too high to observe significant dielectric behavior. Instead of a capacitance close to the geometrical value we measure a purely ohmic resistor and thus zero capacitance. This is due to the specifications of the HP 4192A (the device under test should have a series resistance of  $> 100 \Omega$ ) and thus not due to fundamental reasons. Only at sufficient low temperatures ( $< 143$  K) the geometrical capacitance is retained.

The relative permittivity,  $\epsilon_r = 3.4$ , was determined from the geometrical capacitance and both contacts were assumed ohmic.<sup>17</sup> The minimum (negative) value for the capacitance was clearly resolved at 113-143 K (figure 5), from which we could determine the recombination constant (see fig. 1) as well. Here, the model gives an accurate description of the data in the entire frequency range. From these simulations, the recombination constant was determined to be  $\gamma = \chi/23$  and  $\gamma = \chi/13$  at 143 and 113 K, respectively. These results thus indicate a temperature dependent recombination rate constant. This was found before by Nelson who used a temperature dependent ratio between free and trapped positive polarons to explain this.<sup>28</sup>

## 5.4 Summary

We demonstrate that in metal-insulator-metal configuration the time-dependent drift-diffusion equations result in a negative capacitance for bipolar transport. At high recombination rates, the frequency for zero capacitance,  $f_0$ , is found to scale as  $f_0 \sim (\mu_n \mu_p)^{0.62} V/L^2$ . At zero recombination rate, we find  $f_0 \sim \sqrt{\mu_n \mu_p}/L$ .

Two examples of capacitance spectra on low mobility charge transporting layers exhibiting negative capacitances are shown. For the LED electron and hole mobilities were determined as a function of bias. In case of the bulk heterojunction photovoltaic cell the mobilities together with the recombination rate constant were obtained at different temperatures. Finally, we conclude that the capacitance spectra provide an elegant way to directly determine the minority carrier mobility and recombination rate constant without making modifications to the device.

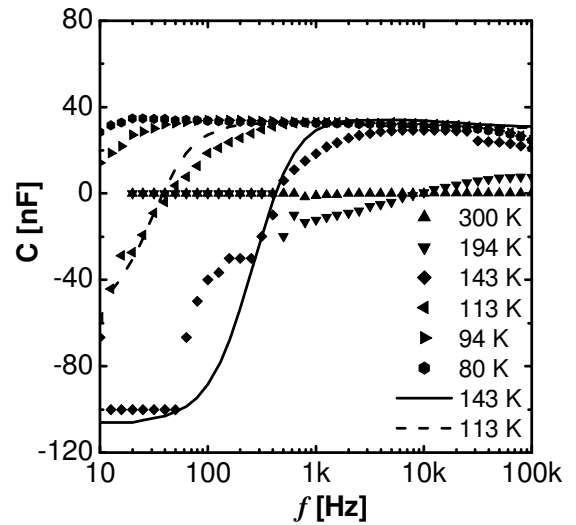


**Figure 5:** Capacitance,  $C(f)$ , in an organic solar cell structure at 1.25 V for different temperatures (see inset). At 143 K  $\mu_n = 1.3 \times 10^{-6} \text{ cm}^2/\text{Vs}$ ,  $\mu_p = 1 \times 10^{-7} \text{ cm}^2/\text{Vs}$  and  $\gamma = 3 \times 10^{-14} \text{ cm}^3/\text{s} = 0.04 \times \chi_L$ . At 113 K  $\mu_n = 1 \times 10^{-7} \text{ cm}^2/\text{Vs}$ ,  $\mu_p = 1 \times 10^{-8} \text{ cm}^2/\text{Vs}$  and  $\gamma = 4 \times 10^{-15} \text{ cm}^3/\text{s} = 0.07 \times \chi_L$ .

## 5.5 References and notes

- [1] H.H.P. Gommans, M. Kemerink, G.G. Andersson, R.M.T. Pijper, *Phys. Rev. B* **69** 155216 (2004).
- [2] L.S.C. Pingree, B.J. Scott, M.T. Russell, M.C. Hersam, *Appl. Phys. Lett.* **86**, 073509 (2005).
- [3] I.N. Hulea, R.F.J. van der Scheer, H.B. Brom, B.M.W. Langeveld-Voss, A. van Dijken, K. Brunner, *Appl. Phys. Lett.* **83**, 1246 (2003).
- [4] H.C.F. Martens, J.N. Huiberts, P.W.M. Blom, *Appl. Phys. Lett.* **77**, 1852 (2000).
- [5] J. Werner, A.F.J. Levi, R.T. Tung, M. Anzlowar, M. Pinto, *Phys. Rev. Lett.* **60**, 53 (1987).
- [6] G.B. Parravicini, A. Stella, M.C. Ungureanu, R. Kofman, *Appl. Phys. Lett.* **85**, 302 (2004).
- [7] V. Kytin, Th. Dittrich, F. Koch, E. Lebedev, *Appl. Phys. Lett.* **79**, 108 (2001).
- [8] J.-C. M'Peko, *Appl. Phys. Lett.* **77**, 735 (2000).
- [9] A.G.U. Perera, W.Z. Shen, M. Ershov, H.C. Liu, M. Buchanan, W.J. Schaff, *Appl. Phys. Lett.* **74**, 3167 (1999).
- [10] F. Lemmi, N.M. Johnson, *Appl. Phys. Lett.* **74**, 251 (1999).
- [11] N.C. Chen, P.Y. Wang, J.F. Chen, *Appl. Phys. Lett.* **72**, 1081 (1998).
- [12] K. Ždánský, *J. Appl. Phys.* **88**, 2024 (2000).
- [13] X. Wu, E.S. Yang, H.L. Evans, *J. Appl. Phys.* **68**, 2845 (1990).
- [14] M. Ershov, H.C. Liu, L. Li, M. Buchanan, Z.R. Wasilewski, A.K. Jonscher, *IEEE Trans. Electron. Devices* **45**, 2196 (1998) and reference therein.
- [15] S.E. Shaheen, C.J. Brabec, N.S. Sariciftci, F. Padinger, T. Fromherz, J.C. Hummelen, *Appl. Phys. Lett.* **78**, 841 (2001).
- [16] C.J. Brabec, S.E. Shaheen, C. Winder, N.S. Sariciftci, P. Denk, *Appl. Phys. Lett.* **80**, 1288 (2002).
- [17] H.H.P. Gommans, M. Kemerink, J.M. Kramer, R.A.J. Janssen, to be published
- [18] W.H.A. Schilders, *Numerical Methods for Semiconductor Device Simulation*, volumes I and II, Springer, Vienna (to appear).
- [19] M. Pope, C.E. Swenberg, *Electronic Processes in Organic Crystals and Polymers*, 2<sup>nd</sup> ed. (Oxford University Press, Oxford, 1999).
- [20] Langevin, *Ann. Chim. Phys.* **28**, 433 (1903).

- [21] A. Privikas, G Juška, A.J. Mozer, M. Scharber, K. Arlauskas, N.S. Sariciftci, H. Stubb, R Österbacka, Phys. Rev. Lett. **94**, 176806 (2005).
- [22] E.A. Schiff, J. Non-Cryst Solids **190**, 1 (1995) and references therein.
- [23] J. Shao, G.T. Wright, Sol. Stat. Elec. **3**, 291 (1969).
- [24] M.A. Lampert, P. Mark, *Current Injection in Solids*, 1<sup>st</sup> ed. (London, Academic Press, 1970).
- [25] H. Bässler, Phys. Stat. Sol. **B 175**, 15 (1993).
- [26] C. Tanase, E.J. Meijer, P.W.M. Blom, D.M. de Leeuw, Phys. Rev. Lett **91**, 216601 (2003).
- [27] P. Blood, J.W. Orton, *The Electrical Characterization of Semiconductors: Majority Carriers and Electron States*, Academic Press, San Diego, 1992.
- [28] J. Nelson, Phys Rev. **B 67**, 155209 (2003).

# Universality of ac conduction for generalized space charge limited transport in ordered solids

### Abstract

*In numerous nonmetallic systems the ac conductivity is observed to follow an approximate power law behavior  $\sigma(\omega) = \omega^s$  with  $0 \leq s \leq 1$ . We show that the presence of non-limiting, i.e. ohmic, contacts on the sample necessarily leads to these characteristics. Ac conductivity curves are obtained by numerical solution of the complete set of time-dependent drift-diffusion equations. The ac conductivity curves can be converted into quasi-universal master curves by application of the Taylor-Isard scaling law for an arbitrary temperature dependence of the mobility. In contrast to the currently prevailing interpretation of ac conductance, our results demonstrate that disorder is not required to account for the experimental observations. However, the implications of disorder on our results are discussed and they are expected to increase the range over which the power law behavior extends.*

## 6.1 Introduction

The literature on ac conductivity in disordered solids and its scaling properties with temperature and composition is extensive and experiments have been performed on a wide range of semiconducting and insulating materials<sup>1-14</sup>. The frequency dependent conductivity is characterized by an approximate power law behavior  $\sigma(\omega) \propto \omega^s$  in which  $s$  is observed to be  $0 \lesssim s \lesssim 1$ . By rescaling the frequency dependent conductivity at various temperatures following Taylor-Isard scaling, master curves can be created that appear to be independent of the actual disordered material. In order to explain this ac conductivity and its universal character, many theories have been proposed in which disorder plays a leading role<sup>14-16</sup>. As disorder on a microscopic level necessarily varies with material and preparation conditions, it is striking that these master curves seem to be independent of the details of the disorder. This is indeed subject of controversy, though in the limit of extreme disorder<sup>14</sup> and near the threshold of percolation<sup>15</sup> the validity of this proposition has been proven by theoretical modeling. Nevertheless, this merely shifts the argument of striking generality as either of these critical limits thus always seems to be achieved experimentally, despite the wide range of sample parameters for which the universality is observed<sup>1-14</sup>.

Although implications of space charge are commonly included in the interpretation of  $I$ - $V$  characteristics on insulating materials, this seems not to be the case in the field of ac conduction and only a few papers have pointed in this direction<sup>3,17</sup>.

Here, we will demonstrate that the use of the drift-diffusion equations in combination with a realistic model for the ohmic contact is in fact sufficient to obtain an ac conductivity that follows  $\sigma(\omega) \sim \omega^s$  with  $0 \lesssim s \lesssim 1$  and that obeys Taylor-Isard scaling. We will refer to this as the generalized space charge limited conductivity (gSCLC) to contrast with conventional SCLC, in which diffusion is commonly neglected. As we only consider the case of constant mobility here, we tacitly assume the absence of disorder.

## 6.2 Drift-diffusion

The drift-diffusion equations are widely used to describe semiconductor devices. The set of coupled partial differential equations is given by the Poisson equation, the continuity equations and the transport equations:

$$\begin{aligned}
 \bar{\nabla} \cdot (\epsilon \bar{\nabla} \phi) &= q(n - p - C) \\
 \bar{\nabla} \cdot \bar{J}_n &= q(\partial_t n + R) \\
 \bar{\nabla} \cdot \bar{J}_p &= q(-\partial_t p - R) \\
 \bar{J}_n &= q(D_n \bar{\nabla} n - \mu_n n \bar{\nabla} \phi) \\
 \bar{J}_p &= q(-D_p \bar{\nabla} p - \mu_p p \bar{\nabla} \phi)
 \end{aligned} \tag{1}$$

where  $\phi$  denotes the electric potential,  $n$  and  $p$  are the free carrier concentrations of electrons and holes, and  $J_n$  and  $J_p$  are the electron and hole current density, respectively.  $D_n$ ,  $D_p$ ,  $\mu_n$  and  $\mu_p$  are the diffusion coefficients and the mobilities of electrons and holes, respectively.  $C$  is the net doping concentration,  $R$  the recombination rate,  $\epsilon = \epsilon_r \epsilon_0$  with  $\epsilon_0$  the permittivity of vacuum and  $\epsilon_r$  the relative permittivity that is assumed constant. Often, the Einstein relation for diffusion,  $D_{n/p} = k_B T / q \mu_{n/p}$ , is assumed to hold, where  $k_B$  is the Boltzmann constant,  $T$  the temperature and  $q$  the elementary

charge. The bars depicted above the variables express their vector character. In this text vectors are depicted bold faced as well.

Numerical solution of the above system of equations is far from trivial. In the 1980's, many conferences (NASECODE and SISDEP/SISPAD series) were held on the topic. The system of equations is singularly perturbed<sup>18</sup> and highly nonlinear. Dedicated numerical methods have been developed to solve the system, and they turn out to be essential for a robust and efficient solution. The Scharfetter-Gummel discretization scheme must be used to discretize the current densities, whereas damped Newton methods<sup>19</sup> or nonlinear variable transformations<sup>20</sup> are essential for the solution of the extremely nonlinear systems of discretized equations. A thorough description of all numerical methods used for semiconductor device simulation is given in ref 21, the simulations described in this paper have been performed using the software package CURRY, developed within the Philips electronics company.

In the calculations presented here we consider only single carrier transport, a constant mobility and  $C$  equal to zero. Therefore we are not obliged to assume any model for the recombination process, the field or density dependence of the mobility, the shape of the doping profile and the temperature dependence of its ionization, which could limit the generality of our conclusions.

As only a small harmonic modulation is generally applied in admittance spectroscopy we may linearize the time dependent problem in the following manner:

$$\frac{\partial}{\partial t} \bar{\nabla}^2 \phi_1 = D \bar{\nabla}^4 \phi_1 + \mu \bar{\nabla} (\bar{\nabla}^2 \phi_0 \bar{\nabla} \phi_1 + \bar{\nabla}^2 \phi_1 \bar{\nabla} \phi_0) \quad [2]$$

With  $\phi(x, t) = \phi_0(x) + \phi_1(x, t)$ ,  $\phi_1(x, t) = \phi_1^0(x) \exp(i\omega t)$  in case we consider hole transport and  $\phi_0$  is derived from

$$D \bar{\nabla}^4 \phi_0 + \mu \bar{\nabla} (\bar{\nabla}^2 \phi_0 \bar{\nabla} \phi_0) = 0. \quad [3]$$

In the discussion below we will refer to the terms in eq. 2 as the displacement term at the left hand side and the diffusion modulation, velocity modulation and density modulation at the right hand side. These expressions can be derived by writing the continuity equation for holes in terms of the electric potential. After replacing the potential by its explicit time (in)dependent terms, one collects the terms in which only  $\phi_0$  appears. Noting that its time derivative equals zero this gives eq. 3, while the terms linear in  $\phi_1$  give eq. 2.

Similar equations, though with the diffusion terms omitted, have been solved analytically by Kassing<sup>22</sup> and Shao and Wright<sup>23</sup>. In the resulting analytical expression, the conductance drops to 2/3 of its steady state value at frequencies much higher than  $1/\tau_t$ , the reciprocal transit time. This has been called the transit time effect, and we will refer to this as the SCLC solution.

The boundary values we choose to remain constant in following discussion are:  $\phi_{hi} = 0$  V and  $\rho_{ni} = 1 \text{ cm}^{-3}$  at the non-injecting contact and  $\phi_i = 1$  V at the injecting contact. Commonly, admittance spectra are determined at zero bias. However, comparison with the analytical description of the transit time effect becomes meaningless as the actual transit time is then defined infinite. Below, we will show that the conductivity for  $\phi_i = 0$  V and  $\phi_i = 1$  V yields similar results in case diffusion is included.

In case diffusion currents are neglected, the logical second boundary condition at the injecting contact for SCLC is  $-\nabla \phi \equiv E(0) = 0$ <sup>22-24</sup> (‘ $\equiv$ ’ means ‘defined as’). When including diffusion, it is more realistic to apply the free carrier density at the interface,  $(-\epsilon/q) \nabla^2 \phi \equiv \rho_i$ , as the boundary condition:



$$\rho_i = n_{metal} \exp\left(-\frac{\Delta\phi}{kT}\right),$$

with  $\Delta\phi$  the effective barrier height for carrier injection from the metal Fermi level into the transport level of the dielectric and  $n_{metal}$  the carrier density in the metal<sup>25</sup>. As an ohmic contact is required to probe the bulk properties,  $\Delta\phi$  must be small, ( $\approx 0.2$  eV), and  $\rho_i$  may become unrealistically large, i.e. larger than the density of states (DOS) of the dielectric. Therefore, we set  $\rho_i$  equal to the DOS. The temperature is set 300 K.

## 6.3 Results and discussion

### 6.3.1 Approximate power law behavior

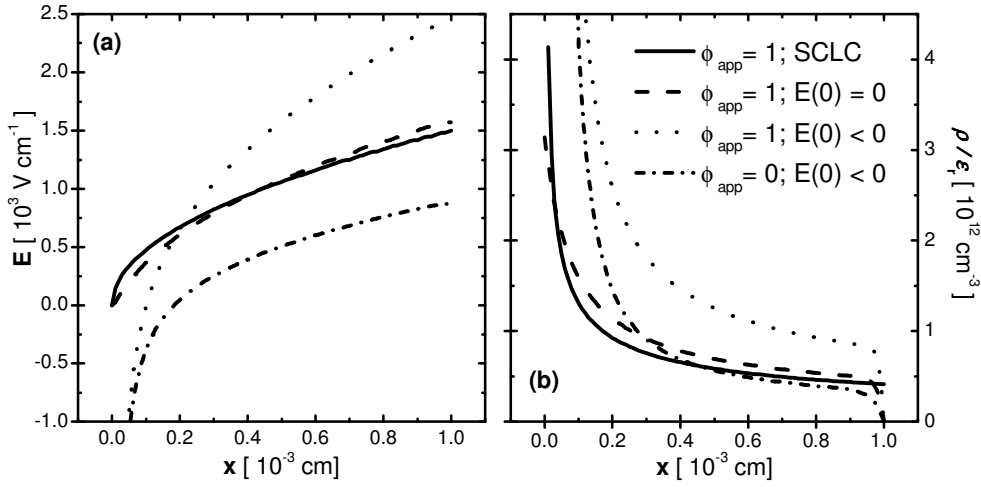


**Figure 1:** (a) Electric field,  $E$ , and (b) charge concentration divided by the relative dielectric constant,  $\rho/\epsilon_r$ , for a dielectric layer of  $10 \mu\text{m}$  in space charge configuration. The legend in (a) is identical to that in (b). The boundary conditions are shown in the inset;  $\phi_{app} = \phi_i - \phi_{ni} = \phi_i$  and for  $E(0) = 0$  and  $E(0) < 0$  we choose  $\rho_i = 3 \times 10^{13} \text{ cm}^{-3}$  and  $\rho_i = 1 \times 10^{21} \text{ cm}^{-3}$ , respectively.  $E$  and  $\rho/\epsilon_r$  derived from the Mott-Gurney square law,  $J_0 = 9/8 \epsilon_r \epsilon_0 \mu \phi_{app}^2 L^{-3}$ , are denoted as SCLC.

The solutions for the electric field and charge concentration in the steady state are compared in Fig. 1 where we used  $(-\epsilon/q)\nabla^2\phi_i \equiv \rho_i = 3 \times 10^{13} \text{ cm}^{-3}$ , which gives  $-\nabla\phi_i \equiv \mathbf{E}(0) = 0$ , and  $\rho_i = 10^{21} \text{ cm}^{-3}$ . Also given is the steady state solution obtained from the Mott-Gurney square law (MG). We observe that both the field and the charge density as a function of position resemble the MG law quite well for the condition  $\mathbf{E}(0) = 0$ . However, at  $\rho_i = 10^{21} \text{ cm}^{-3}$ , we observe  $\mathbf{E}(0) < 0$ . This is readily understood<sup>25</sup> as in the steady state  $\bar{\nabla} \cdot \bar{\mathbf{J}}_p = q\bar{\nabla} \cdot (-D_p \bar{\nabla} p + \mu_p p \bar{\mathbf{E}}) = 0$  holds and hence the superposition of the drift and diffusion currents is independent of position. As the gradient in charge density increases towards the injecting contact beyond the value given by the MG law, the diffusion current must be opposed by a drift current towards the injecting contact, which requires a negative electric field.

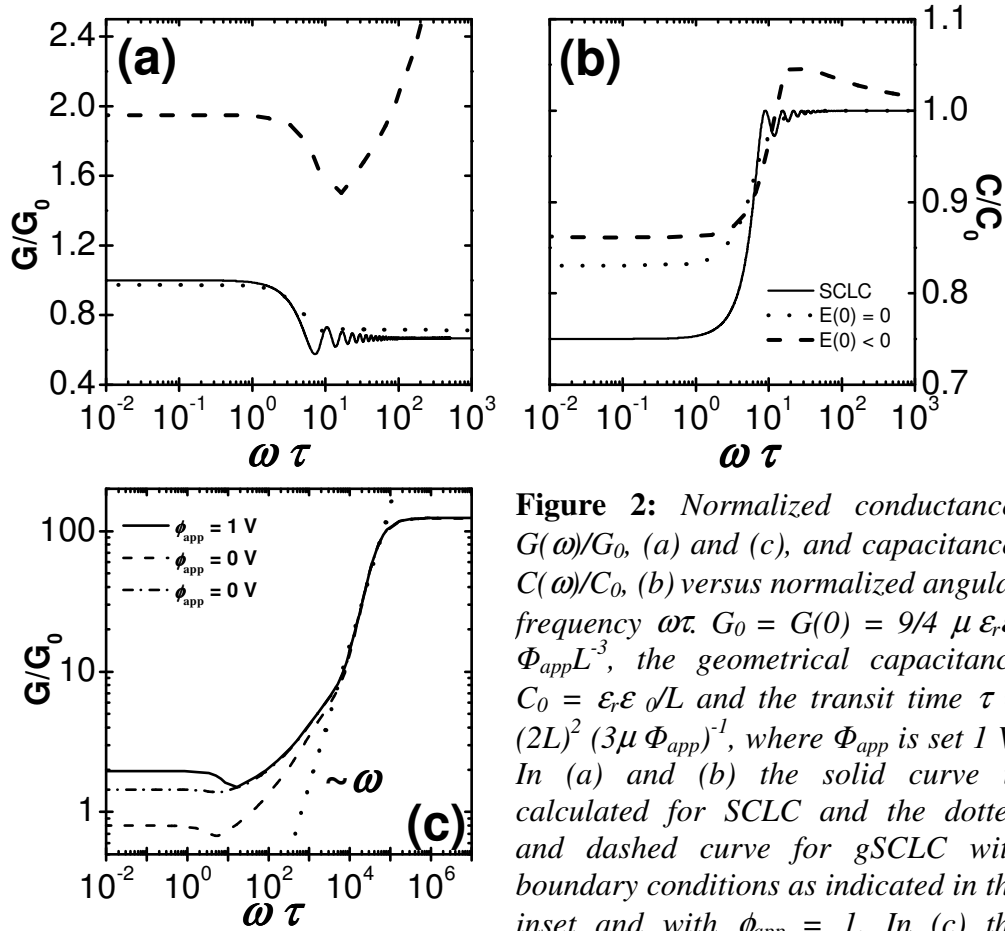


**Figure 2:** Normalized conductance,  $G(\omega)/G_0$ , (a) and (c), and capacitance,  $C(\omega)/C_0$ , (b) versus normalized angular frequency  $\omega\tau$ .  $G_0 = G(0) = 9/4 \mu \epsilon_r \epsilon_0 \Phi_{app} L^{-3}$ , the geometrical capacitance  $C_0 = \epsilon_r \epsilon_0 / L$  and the transit time  $\tau = (2L)^2 (3\mu \Phi_{app})^{-1}$ , where  $\Phi_{app}$  is set 1 V. In (a) and (b) the solid curve is calculated for SCLC and the dotted and dashed curve for gSCLC with boundary conditions as indicated in the inset and with  $\phi_{app} = 1$ . In (c) the conductance for gSCLC and  $E(0) < 0$  as in (a), is shown again on double logarithmic scale.

In Fig. 2 the normalized conductance and capacitance is shown as a function of normalized angular frequency. For both  $\rho_1 = 3 \times 10^{13} \text{ cm}^{-3}$  ( $E(0) = 0$ ) and  $\rho_1 = 10^{21} \text{ cm}^{-3}$  ( $E(0) < 0$ ) the transit time effect is clearly observed around 3 - 10  $\omega\tau$ . For the more realistic boundary condition  $\rho_1 = 10^{21} \text{ cm}^{-3}$ , however, at frequencies beyond 10  $\omega\tau$  the conductance increases almost two orders of magnitude following a power law  $\omega^s$  with  $0 \lesssim s \lesssim 1$ . Note that for both boundary conditions the high frequency capacitance converges to the geometrical value (fig 2b). The low frequency conductance for the latter boundary condition ( $E(0) < 0$ ) is about two times higher than for the former case ( $E(0) = 0$ ) because the carrier concentration near the non-injecting contact is about two times higher (fig 1b). These calculations show that for  $E(0) = 0$  the diffusion component in both the steady state and in the time dependent solution may indeed be neglected. The oscillations that are found in the SCLC solution vanish in the solution of the full drift-diffusion problem. It should be emphasized that despite the fact that the conductivity in the drift-diffusion equations does not scale with applied bias, a bias is applied to compare the outcomes with the analytical SCLC solution.

In order to gain more insight in the frequency dependence of the conductance, the solution for the time dependent eq. 2 is given for three frequencies in terms of  $-\nabla\phi_1 \equiv \mathbf{E}_1 = \mathbf{E}_{ac}$  and  $(-\epsilon/q) \nabla^2\phi_1 \equiv \rho_1 = \rho_{ac}$  in Fig. 3. With increasing frequency the real and imaginary contributions to  $\mathbf{E}_1$  and  $\rho_1$  start to diminish at the non-injecting side. Physically, this behavior results from the finite velocity of the charge carriers which causes a decreasing penetration depth and hence a decreasing ability to screen external fields with increasing frequency. This ultimately leads to a charge response that is restricted to the injecting contact and hence a constant electric field ( $\phi_1/L$ ) in the

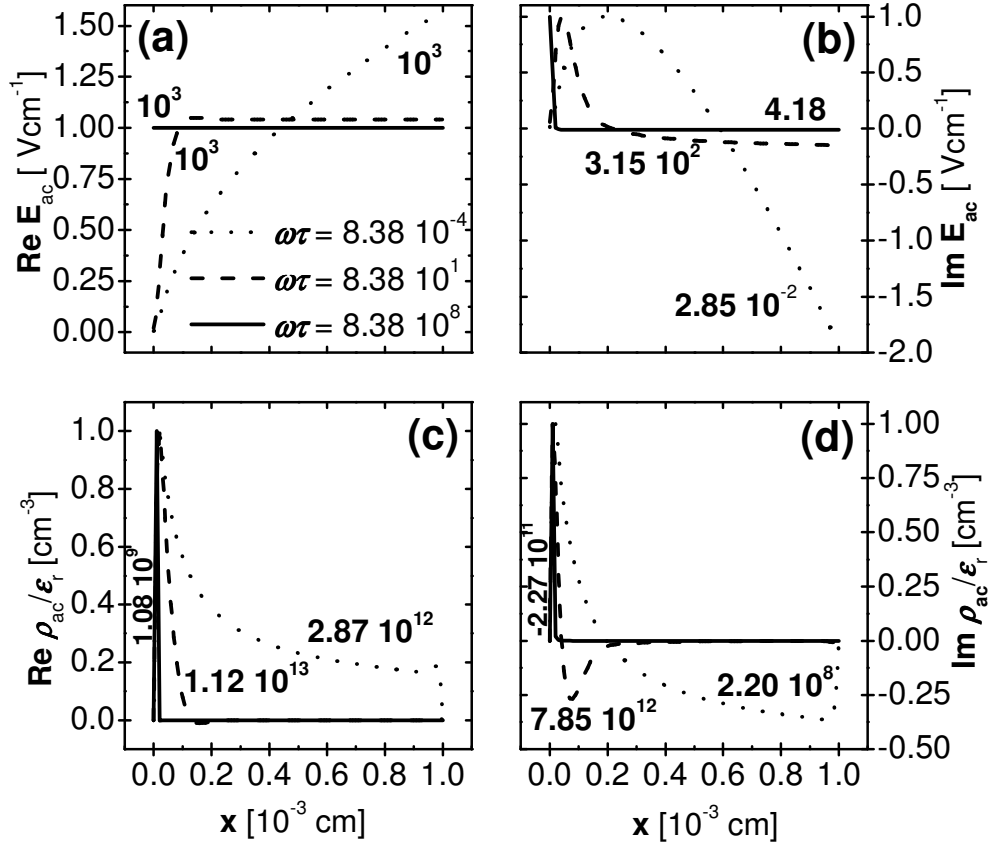


**Figure 3:** Real (a) and imaginary (b) part of the time dependent electric field and real (c) and imaginary (d) part of the time dependent charge concentrations for three frequencies given in (a) for  $\phi_i = 1$  and  $\rho_i = 1 \times 10^{21} \text{ cm}^{-3}$  at  $\phi_{app} = 1 \text{ V}$ . In (a) the field is normalized by  $\phi_i/L$  and in (b), (c) and (d) all curves are normalized on their peak value (normalization constants are depicted in the graphs).

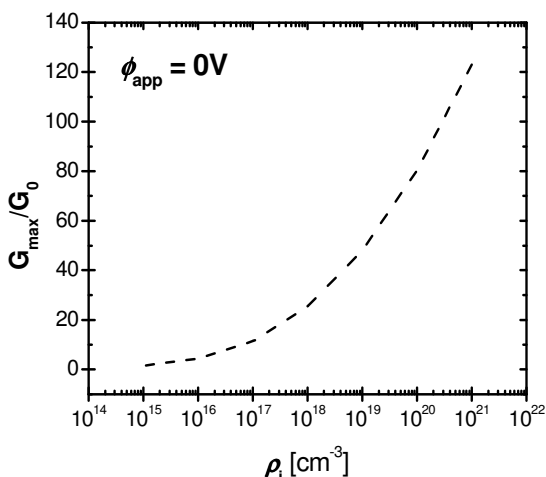


**Figure 4:** saturation conductivity,  $G_{max}$ , versus charge concentration at the injecting interface.  $G_0 = G(0) = 9/4 \mu \epsilon \epsilon_0 \Phi_{app} L^{-3}$

remaining dielectric layer. Therefore, at high frequencies the in-phase velocity modulation near the injecting contact ( $\sim \nabla^2 \phi_0 \nabla \phi_1$ ) is much higher in case of  $\rho_i = 10^{21} \text{ cm}^{-3}$  than for  $\rho_i = 3 \times 10^{13} \text{ cm}^{-3}$ . Since the density modulation and the diffusion modulation decrease and finally vanish with increasing frequency, the velocity modulation becomes the dominating term in the conductance near the injecting contact at sufficiently high frequencies. This velocity modulation simultaneously induces a displacement current that becomes the dominating term away from the injecting contact.

In fig 4 we demonstrate the variation of the high frequency conductivity (the saturation value) with charge density at the injecting contact. This shows that the occurrence of the calculated power law behavior does not critically depend on the charge concentration at the electrodes. However,

the dependence of the saturation value of the ac conductivity on the charge concentration at the electrodes implies that admittance spectroscopy can in principle be used as a probe for the density of states.

### 6.3.2 Taylor Isard scaling and the BNN relation

Taylor-Isard scaling has been applied in a number of experiments and reflects the time-temperature superposition that appears to hold generally<sup>1-14</sup>:

$$\frac{\sigma(\omega)}{\sigma(0)} = F\left(C \frac{\omega}{\sigma(0)}\right). \quad [4]$$

Here,  $C$  is the Taylor-Isard constant and  $\sigma(0)$  is the conductivity at low frequencies. It is found that  $C$  is determined by the Barton-Nakajima-Namikawa (BNN) relation<sup>14</sup>:

$$\sigma(0) = p\Delta\epsilon\epsilon_0\omega_m \quad [5]$$

which gives  $C = \Delta\epsilon\epsilon_0$ . This relation was observed for electric conduction on both ionically and electronically conducting oxide glasses<sup>26</sup>. Here  $\omega_m$  is the angular frequency at the relaxation peak,  $\epsilon_0$  is the permittivity of vacuum,  $\Delta\epsilon$  is the magnitude of the dielectric relaxation and  $p$  is a numerical constant experimentally determined to be of order one. Recently, Sidebottom<sup>3</sup> proposed a scaling that combined both laws<sup>14</sup>.

The complex conductivity  $\sigma(\omega) = \sigma'(\omega) + i\sigma''(\omega)$  (both  $\sigma'(\omega)$  and  $\sigma''(\omega)$  are real valued functions of  $\omega$ ) is calculated for increasing mobility and the real part,  $\sigma'(\omega)$ , is shown at normal and scaled axes for zero bias in figure 5. This figure should emphasize the similarity with experimental curves typically obtained with increasing temperature. The proportionality of both  $\sigma(0)$  and  $\omega_m$  with  $\mu$  is clearly visualized and will be derived in a moment. The typically observed Arrhenius temperature dependence in both  $\sigma(0)$  and  $\omega_m$  with similar activation energies is thus readily explained as in (g)SCLC both quantities are proportional to  $\mu$ , which normally follows an Arrhenius law. This implies that the time-temperature superposition property is obtained for any temperature dependence of  $\mu$  in case of SCLC transport. Here, we did not choose the scaling constant  $C$  to be proportional to  $1/T$  as is sometimes applied. In case the temperature range is limited ( $T_{\min}/T_{\max} \leq 0.5$ ) this will not affect the scaling property severely and in this manner we are not obliged to assume a Curie law for  $\Delta\epsilon$ .<sup>14</sup> In order to estimate the dielectric relaxation the complex relative permittivity defined as  $\epsilon(\omega) = [\sigma(\omega) - \sigma(0)] / (i\omega\epsilon_0) + 1$  is calculated and the imaginary part,  $\epsilon''(\omega)$ , ( $\epsilon(\omega) = \epsilon'(\omega) - i\epsilon''(\omega)$ ) where  $\epsilon'(\omega)$  and  $\epsilon''(\omega)$  are real valued functions of  $\omega$ ) is shown both on normal and scaled axis in correspondence to ref 26 (fig 5). From this we conclude that  $\Delta\epsilon$  is independent of the mobility as can be readily understood for both  $\omega_m$  and  $\sigma(0)$  are observed to be linear in  $\mu$ . From figure 5 we obtain  $\omega_m \approx 66/\tau_r = 50\mu\phi_{\text{app}}L^{-2}$ , where we used  $\phi_{\text{app}} = 1$ .

Now,  $\sigma(0) \equiv LdJ_0/d\phi_{\text{app}} = LG(0)$  and in case we apply the MG law we obtain  $\sigma(0) = 9/4 \epsilon_r\epsilon_0 \mu \phi_{\text{app}} L^{-2}$ . It should be clear that  $\Delta\epsilon \propto \epsilon_r$ , as the maximum of the dielectric relaxation scales with the high frequency conductivity by definition, which in turn scales with  $\epsilon_r$  in case of (g)SCLC and eq. 5 is derived for  $p$  equal to some numerical value.

One difficulty remains for SCLC though, as at zero bias the dielectric layer is entirely depleted and  $\sigma(0)$  becomes zero. However, for gSCLC, the diffusion causes the steady state charge density  $\sim -\nabla^2\phi_0$  to converge to a positive and finite valued function of  $x$ , even when the applied bias

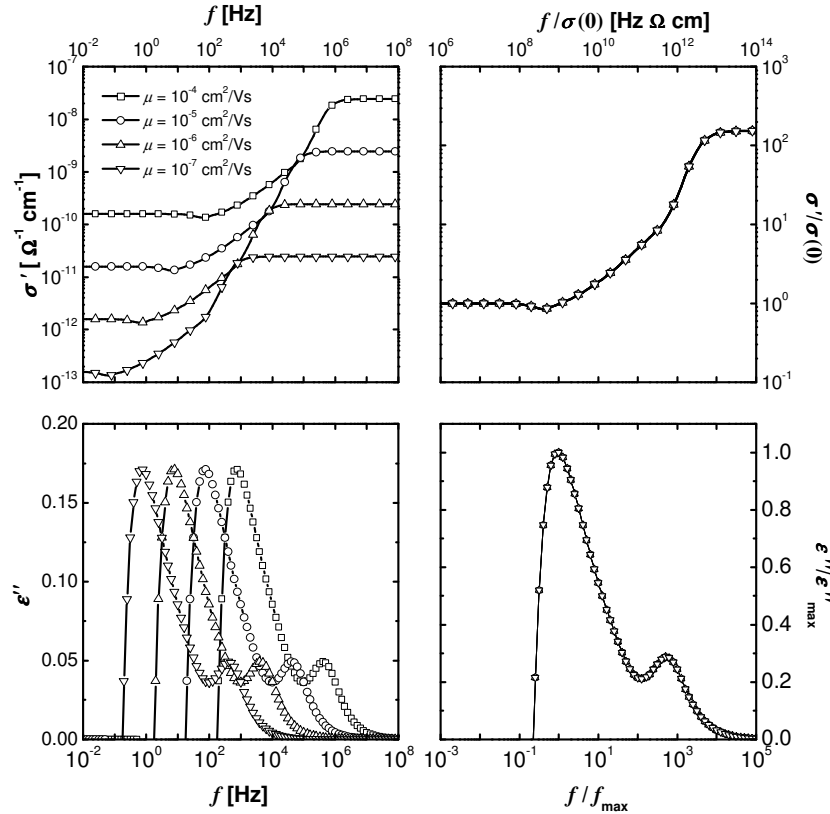


**Figure 5:** The real part of the complex conductivity  $\sigma'(f)$  and the imaginary part of the complex relative permittivity  $\epsilon''(f)$  as a function of frequency for increasing mobility. The right graphs show the same curves on scaled axis as indicated. Here,  $\rho_i = 1 \times 10^{21} \text{ cm}^{-3}$ ,  $L = 10^{-3} \text{ cm}$ ,  $\epsilon_r = 10$  and the applied bias,  $\phi_{app}$ , is 0 V.

is zero (see Fig. 1). Consequently, the conductance as calculated from the solution for  $\phi_1$  in eq. 2 for  $\phi_{app} = 0\text{V}$  resembles that for  $\phi_{app} = 1\text{V}$  (Compare G fig 2c with  $\sigma'(f)$  in fig 5).

From fig. 5  $p$  is determined to be 2.1 and thus closely corresponds to the values in ref 26. This value is far from general as a variety of mechanisms may change the conductivity at both low and high frequencies as will be explained in the subsequent paragraphs. Only in case of one blocking and one ohmic contact with well-defined sharp interfaces on *microscopic* level, injecting charge carriers in an otherwise completely depleted dielectric layer, this can be taken as a limiting value for  $p$ .

So far, (g)SCLC transport has been considered, which gives rise to quadratic  $I$ - $V$  characteristics, in contrast to the ohmic behavior that is typically observed for most disordered materials. By increasing the background/impurity doping concentration to the order  $\epsilon_r \times 10^{12} \text{ cm}^{-3}$ , the ohmic contribution to  $\sigma(0)$  becomes dominant, while the high-frequency behavior remains unchanged. Simultaneously,  $p$  is thus found to increase.

In these calculations we employ a constant mobility to demonstrate the ac conductance and scaling behavior in an ordered medium. The effects of disorder on the mobility have been described in a number of publications demonstrating a mobility that increases with electric field<sup>25, 27, 28</sup> and charge concentration<sup>29, 30</sup>. Taking into account disorder therefore leads to a mobility that increases towards the injecting contact. Consequently, the ac conductivity, which we have shown to be dominated by the velocity modulation in this region, may extend over a larger frequency domain and covers a larger conductivity range than calculated here.

According to these calculations the universality of ac conductance is predicted to include ordered solids as well. The only requirement is that the reciprocal transit time is in the probed frequency range ( $10^0$ - $10^6$  Hz). For organic crystals ( $\mu \sim 10^0$  cm<sup>2</sup>/Vs)<sup>31</sup> this means the sample thickness should be  $\geq 10^{-3}$  cm, which seems feasible. Finally, we should emphasize that the present results do not limit the validity of previous, disorder-based models for the ac conductivity. However, we feel that the space charge effects discussed in this paper should be incorporated in a full description of the fascinating phenomena associated with ac conductivity.

## **6.4 Conclusion**

In conclusion, we have demonstrated that space charge dynamics can explain the approximate power law behavior that is commonly observed in ac conductance experiments on dielectric materials. Moreover, the numerically calculated ac conductance curves are shown to obey the experimentally observed scaling laws. For this, no specific mobility model nor any parameters reflecting unknown disorder need to be assumed. Therefore the applied generalized SCLC model has general validity for admittance spectroscopy on dielectric materials, irrespective of the presence of disorder. However, we expect that a full understanding of ac transport in dielectrics requires a simultaneous description of both space charge and disorder.

## 6.5 References and notes

- [1] C. Chiteme, D.S. McLachlan, Phys. Rev. B **67**, 024206 (2003).
- [2] B. Roling, C. Martiny, S. Murugavel, Phys. Rev. Lett. **87**, 085901-1 (2001).
- [3] D.L. Sidebottom, Phys. Rev. Lett. **82**, 3653 (1999).
- [4] M.P.J. van Staveren, H.B. Brom, L.J. de Jongh, Phys. Rep. **208**, 1 (1991) and references therein.
- [5] S. Berleb, W. Brütting, Phys. Rev. Lett. **89**, 286601-1 (2002).
- [6] A. Ghosh, M. Sural, Europhys. Lett. **47**, 688 (1999.)
- [7] D.S. McLachlan, M.B. Heaney, Phys. Rev. B **60**, 12746 (1999).
- [8] A.R. Kulkarni, P. Lunkenheimer, A. Loidl, Sol. Stat. Ion **112**, 69 (1998).
- [9] H.B. Brom, J.A. Reedijk, H.C.F. Martens, L.J. Adriaanse, L.J. de Jongh, M.A.J. Michels, Phys. Stat. Sol. (b) **205**, 103 (1998).
- [10] J.A. Reedijk, L.J. Adriaanse, H.B. Brom, L.J. de Jongh, G. Schmid, Phys. Rev. B **57**, R15116 (1998)
- [11] M.T. Connor, S. Roy, T.A. Ezquerra, F.J. Baltá Calleja, Phys. Rev. B **57**, 2286 (1998)
- [12] B. Roling, A. Happe, K. Funke, M.D. Ingram, Phys. Rev. Lett. **78**, 2160 (1997).
- [13] N. Balkan, P.N. Butcher, W.R. Hogg, A.R. Long, S. Summerfield, Philos. Mag. B **51**, L7 (1985)
- [14] J.C. Dyre, T.B. Schrøder, Mod. Rev. Phys. **72**, 873 (2000) and references therein.
- [15] A.V. Milovanov, J.J. Rasmussen Phys. Rev. B **64** 212203 (2003).
- [16] J.P. Clerck, G. Giraud, J.M. Langier, J.M. Luck, Adv. Phys **39**, 1 (1990) and references therein.
- [17] G.F. Leal Ferreira, L.E. Carrano de Almeida, Phys. Rev. B **56**, 11579 (1997).
- [18] P.A. Markowich, SIAM J. Appl. Math. **5**, 896 (1984).
- [19] R.E. Bank, D.J. Rose, Numer. Math. **37**, 279 (1981).
- [20] S.J. Polak, C. den Heijer, W.H.A. Schilders, P.A. Markowich, Int. J. Numer. Methods Eng. **24**, 763 (1987).
- [21] W.H.A. Schilders, *Numerical Methods for Semiconductor Device Simulation*, volumes I and II, Springer, Vienna (to appear).

- [22] R. Kassing, Phys. Stat. Sol. (a) **28**, 170 (1975).
- [23] J. Shao, G.T. Wright, Sol. Stat. Elec. **3**, 291 (1969).
- [24] M.A. Lampert, P. Mark, *Current Injection in Solids* (Academic Press, New York and London, 1970).
- [25] M. Pope, C.E. Swenberg, *Electronic Processes in Organic Crystals and Polymers*, 2<sup>nd</sup> ed. (Oxford University Press, Oxford, 1999).
- [26] H. Namikawa, J. Non-Cryst. Sol. **18**, 173 (1975).
- [27] P.M. Borsenberger, D.S. Weiss, *Organic Photoreceptors for imaging systems* (Dekker, New York, 1993); *Organic Photoreceptors for Xerography* (Dekker, New York, 1998), and references therein.
- [28] H. Bässler, Phys. Status Solidi B **175**, 15 (1993), and references therein.
- [29] O. Rubel, S.D. Baranovskii, P. Thomas, S. Yamasaki, Phys. Rev. B **69**, 014206 (2004).
- [30] C. Tanase, E.J. Meijer, P.W. M. Blom, D.M. de Leeuw, Phys. Rev. Lett **91**, 216601 (2003).





## Summary

In the early nineties a new polymer has been discovered with conducting as well as luminescent abilities in diode configuration. This has drawn a lot of attention as it may be a new and low cost alternative to conventional materials in display technology. An additional advantageous property shared by many other polymers is its flexibility that allows for the desired folding. Subsequently, large investments in the development of such polymers are made in order to improve on the performance for consumer electronics.

An important aspect in this performance are the electrodes which have to be manufactured. One requirement is that at least one electrode is transparent, which allows for the out coupling of the generated light. Another demand is directly related to whether positive or negative charge carriers have to be injected into the polymer. For light generation both are needed and consequently two different electrodes are generally applied. Here, the importance of the right electrodes is thus stressed, as the polymer contains hardly any intrinsic carriers.

In the choice for the electrode material the intrinsic properties are often considered. However, these may alter in case the material is brought into contact with the polymer. In turn the properties of the polymer can change as well due to the presence of the electrode or its deposition process. In a more extreme situation such interface may exhibit even new conducting or optical properties. In this thesis a successful attempt is undertaken to characterize these interfaces by a variety of techniques and an explanation is presented that unifies the outcomes.

Ion scattering analysis have demonstrated the diffusion of Cs and K into the polymer (MDMO-PPV) during the process of physical vapor deposition. The total amount of alkali deposition remained below one monolayer at all times and the presence of alkali was observed up to 30 nm below the MDMO-PPV surface. Surprisingly, the maximum alkali concentration was found at 1.6 nm, while at the outermost surface its concentration was below the detection limit of ppm. Despite these low deposition concentrations the light output improved tremendously (factor  $10^3$ ) due to the increase of electron injection. This increase was confirmed by admittance spectroscopy. Moreover an alternative interpretation for the capacitance is presented that is typically observed for these systems.

In order to explain the improved performance of deposited LiF onto fullerene-polymer blends (PCBM:MDMO-PPV) blends in solar cell configuration it is required to characterize the charge transport. Hence, we have determined  $I$ - $V$  curves under illumination for a temperature range of 80-300 K. Bimolecular recombination is used to describe these curves, while geminate recombination, which incorporates an explicit field dependence, appears unsuitable.

The minority carrier mobility is difficult to determine in  $I$ - $V$  characterization, as its dissipation is marginal compared to that of the majority carrier. Admittance spectroscopy can resolve this issue. In case both charge carriers are injected the drift-diffusion equations demonstrate a transition from positive towards negative values in the capacitance. Here, we discuss the relation between this transition and the carrier mobilities making some assumptions for the injection barriers and recombination rate. Subsequently, we have measured the capacitance in order to determine the minority carrier mobility in both a polymer LED and solar cell. For the LED these experiments were conducted as a function of bias, while for the solar cell the temperature was varied.

Finally, it is calculated that an electrode with ohmic injection into a material with low intrinsic carrier concentration leads to ac conductivity. Ac conductivity is found numerous times in all kinds of dissipating systems and commonly attributed to disorder. Here, it is thus argued that disorder is not a required ingredient. Simultaneously, the two experimentally observed scaling laws are demonstrated to hold within this description.



## Samenvatting

Begin jaren negentig heeft men een nieuw type polymeer uitgevonden dat in diode structuur zowel over geleidende als lichtgevende eigenschappen beschikt. Vooral dit laatste trekt enorm de aandacht aangezien een nieuw en mogelijk goedkoper alternatief is gevonden voor de reeds ontwikkelde materialen in de beeldschermtechnologie. Een extra voordeel van dit polymeer is de buigzaamheid, een eigenschap die ze overigens delen met veel 'gewone' polymeren, waardoor ze desgewenst geschikt zijn om op te rollen. Veel energie wordt derhalve gestoken in de ontwikkeling van dergelijke polymeren om tot een optimale prestatie te komen in de consumenten electronica.

Een belangrijk aspect voor de prestatie van een uiteindelijk product zijn de electrodes die moeten worden aangebracht. Een eerste vereiste is dat één van de twee electrodes transparant is, zodat het licht ook daadwerkelijk kan worden waargenomen. In de tweede plaats wordt de keuze bepaald door de vraag of er voornamelijk positieve dan wel negatieve ladingsdragers geïnjecteerd moeten worden in het plastic. Voor de generatie van licht zijn beiden noodzakelijk en in het algemeen worden dus twee verschillende electrodes toegepast. Aangezien het polymeer zelf nauwelijks over ladingsdragers beschikt krijgt men een idee van het belang voor een juiste keuze van het electrode materiaal.

Bij deze keuze worden vaak de intrinsieke eigenschappen van het electrode materiaal in overweging genomen. Deze kunnen echter veranderen op het moment dat het in contact wordt gebracht met het polymeer. Ook het polymeer zelf kan veranderen onder invloed van het electrode materiaal of als gevolg van het proces van aanbrengen van de electrode. In een bijzonder geval is het zelfs mogelijk dat een grenslaag wordt gevormd tussen electrode en polymeer, die geheel nieuwe geleidende of optische eigenschappen in zich herbergt. In dit proefschrift is een succesvolle poging gedaan om dergelijke grenslagen te karakteriseren met behulp van een verscheidenheid aan technieken en de resultaten daarvan te combineren tot een inzichtelijk verband.

Ionenverstrooiings-experimenten hebben aangetoond dat zowel kalium als cesium bij het aanbrengen door middel van opdammen nadrukkelijk het polymeer (MDMO-PPV) in diffunderen. Deze diffusie is aangetoond voor totale hoeveelheden van minder dan één monolaag en tot op 30 nm voorbij het MDMO-PPV oppervlak. Opvallend hierbij is dat de concentratie alkali aan het MDMO-PPV oppervlak beneden de detectielimiet van ppm's zat en dat het concentratie maximum zich 1.6 nm onder dit oppervlak bevond. Dergelijke lage concentraties hebben desalniettemin een enorme invloed op de licht opbrengst in een LED configuratie (factor  $10^3$ ) als gevolg van een verbetering van electron-injectie aan deze grenslaag. Dit laatste is bevestigd door admittantie metingen. In de uitleg van de admittantie spectra op dergelijke LEDs hebben we ook een alternatieve interpretatie voor de typisch gemeten capaciteit gegeven.

Om de prestatie verbetering als gevolg van opgedampt LiF op mengsels van fullereen en polymeer (PCBM en MDMO-PPV) in een zonnecel configuratie te begrijpen was het noodzakelijk om het ladingstransport te karakteriseren. Hiertoe hebben we *I-V* curves bepaald onder lichtinval bij temperaturen variërend tussen 80 tot 300 K. Om deze curves te kunnen verklaren blijkt bimoleculaire recombinatie een noodzakelijke ingrediënt. Onsager recombinatie met een expliciete veld afhankelijkheid daarentegen blijkt hiermee niet verenigd te kunnen worden.

De bijdrage van de ladingsdrager met lage mobiliteit blijkt moeilijk te bepalen in *I-V* karakterisatie, aangezien deze wordt overschaduwed door de bijdrage van de ladingsdrager met hogere mobiliteit. Admittantie metingen kunnen hiervoor een uitkomst bieden. Het blijkt in het geval van de aanwezigheid van twee ladingsdragers dat de drift-diffusie vergelijking een overgang van positieve naar negatieve waarden in de capaciteit voorspellen. Hier hebben we uitgelegd hoe deze overgang direct kan worden gerelateerd aan de mobiliteit van beide ladingsdragers, mits een aantal aannames worden gedaan ten opzichte van de injectiebarrières en de recombinatie. Vervolgens hebben we de capaciteit gemeten om de mobiliteit van de ladingdragers met lage

mobiliteit te karakteriseren in zowel plastic LEDs als zonnecellen. Voor de eerste hebben we dit gedaan als functie van de bias en bij de laatste als functie van de temperatuur.

Uiteindelijk is ook berekend dat een electrode, die zorgt voor maximale injectie in een materiaal met een lage concentratie intrinsieke ladingsdragers, leidt tot een frequentie afhankelijke geleiding. Dergelijke geleiding is al een aantal keren gevonden op zeer verschillende materialen, maar tot nu toe uitsluitend toegeschreven aan wanorde. Naar aanleiding van deze bevindingen lijkt wanorde dus geen noodzakelijk ingrediënt. Tegelijkertijd wordt met deze beschrijving wel voldaan aan een tweetal schalingswetten die experimenteel zijn waargenomen.

## Dankwoord

Bij de tot standkoming van dit proefschrift heb ik ook anderen in de gelegenheid gesteld hun tijd een zinvolle invulling te geven.

Martijn Kemerink, mijn dagelijks begeleider, meest opvallend is jouw altijd positieve invalshoek, waarmee je anderen weet te motiveren. Mijn dank voor deze noodzakelijke inspiratie en de werkelijk onbeperkte hoeveelheid tijd die je vrijmaakte. Hierbij wil ik Arnoud Denier van der Gon vermelden voor de eerste twee-en-een-half jaar dat hij zich van deze taak kwijtte. Het abrupte einde van zijn 39-jarige leven kwam voor iedereen als een schok. Ralf Pijper and Jan-Maarten Kramer zijn als afstudeerders altijd met veel inzet aan de slag gegaan. Ik heb mijn uiterste best gedaan om de enorme hoeveelheid experimentele data van jullie hand te vereeuwigen in de literatuur. Misschien heb ik iets kunnen overbengelen, ongetwijfeld heb ik meer geleerd van jullie. René Janssen, mijn eerste promotor, die veel energie heeft gestoken om mijn hoofdstukken begrijpelijk te maken voor de lezer(s?). Je hebt me overtuigd dat vriendschap en wetenschap altijd te verenigen zijn. Als gevolg van de trend om technische apparatuur niet meer zelf te ontwikkelen maar commerciële varianten aan te schaffen lijkt de technische ondersteuning van de groep van toenemend belang. In het bijzonder die van Gerard Wijers, bij wie iedereen tussen de vakanties door mag aankloppen. En natuurlijk alle leden van de huidige groep M2N en voorheen FOG gedurende de periode 2001-2005: Ondanks de enorme werkdruk was de sfeer in de groep altijd erg goed. Bedankt voor de vele uitjes waarvoor ik was uitgenodigd en veel succes met het verdere verloop van jullie onderzoek/carrière.

Tijdens de afgelopen jaren heb ik ook samenwerkingen mogen aangaan met de volgende mensen buiten de vakgroep: Gunther Andersson van de universiteit Leipzig, de metingen op de NICISS leverden door de hoge resolutie uiteindelijk veel inzicht in de polymeer-metaal grenslagen. Bedankt voor de gelegenheid die je me geboden hebt op het apparaat en natuurlijk voor je gastvrijheid. Hans Brom van de universiteit Leiden, die ik wil bedanken voor de impedantie analyzer die hij de vakgroep geschonken heeft en de hulp bij de interpretatie van de metingen. Wil Schilders van de faculteit wiskunde en informatica, jouw software voor de berekening van ladingstransport in halfgeleiders heeft enorm bijgedragen aan de interpretatie van de experimentele data en is derhalve van een niet te overschatten waarde voor dit proefschrift. Nu de waarde van het programma in de groep 'ontdekt' is zullen het hopelijk nog velen na mij gebruiken. Het succes van deze samenwerkingen blijkt wel uit de dominante bijdragen van deze technieken in dit hele proefschrift, waarvoor mijn oprechte dank.

In deze opsomming mogen de bijdragen van Martien de Voigt, Leo van IJzendoorn, en Hidde Brongersma van de vakgroep TIB en Calipso bv, natuurlijk niet ontbreken.

De belangstelling van vrienden, kennissen en familie is in de afgelopen jaren van minstens zo'n grote betekenis geweest, want naast de zojuist genoemde inhoudelijke bijdragen zijn ontspanning en relativering altijd een welkome afwisseling.

## List of publications

*Interface formation in K doped poly(dialkoxy-p-phenylene vinylene) light-emitting diodes*

H.H.P. Gommans, A.W. Denier van der Gon, G.G.Andersson, L.J. IJzendoorn, R.M.T. Pijper, and H.H. Brongersma  
J. Appl. Phys. **94**, 5756 (2003)

*Charge transport and trapping in Cs-doped poly(dialkoxy-p-phenylene vinylene) light-emitting diodes*

H.H.P. Gommans, M. Kemerink, G.G. Andersson, and R.M.T. Pijper  
Phys. Rev. B **69**, 155216 (2004)

*Field and temperature dependence of the photocurrent in polymer:fullerene bulk heterojunction solar cells*

H.H.P. Gommans, M. Kemerink, J.M. Kramer, R.A.J. Janssen  
Submitted

*Negative capacitances in low-mobility solids*

H.H.P. Gommans, M. Kemerink, J.M. Kramer, R.A.J. Janssen  
Submitted

*Universality of ac conduction for generalized space charge transport in ordered solids*

H.H.P. Gommans, M. Kemerink, W.H.A. Schilders  
Submitted

*Liquid metals as electrodes in polymer light emitting diodes*

G.G.Andersson, H.H.P. Gommans, A.W. Denier van der Gon, and H.H. Brongersma  
J. Appl. Phys. **93**, 3299 (2003)

## Curriculum Vitae

- 2 jan. 1978 Geboren te Eindhoven
- 1990-1996 Gymnasium, Kruisheren Kollege, Uden
- 1996-2000 Experimentele natuurkunde, Universiteit Utrecht
- 2001-2005 Onderzoeker in Opleiding (OIO), Technische Universiteit Eindhoven; vakgroep: Molecular Materials and Nanosystems, geleid door prof.dr. R.A.J. Janssen